



**UNIVERSITÀ DEGLI STUDI DI PAVIA**

**DOTTORATO IN SCIENZE CHIMICHE E  
FARMACEUTICHE E INNOVAZIONE  
INDUSTRIALE  
(XXXIII Ciclo)**

**Coordinatore: Chiar.mo Prof. Giorgio Colombo**

**Perovskites for optoelectronic applications, new  
synthetic approaches and properties modulation  
routes**

Tesi di Dottorato di  
**Sara Bonomi**

A.A. 2020/2021

**Tutor**  
Chiar.mo Prof. Lorenzo Malavasi

# SUMMARY

Summary .....	0
Abstract .....	3
1. Introduction .....	7
1.1 Perovskites .....	9
1.1.1 Crystal structure and stability factors .....	10
1.1.2 Optoelectronic properties .....	13
1.1.3 Lead-free trend .....	18
1.2 Thin films making techniques .....	24
1.2.1 The flaws of solution methods .....	25
1.2.2 Vapor-based techniques .....	29
1.3 Perovskites modulation .....	32
2. Rf magnetron sputtering .....	34
2.1 MAPbI <sub>3</sub> .....	38
2.2 CsSnBr <sub>3</sub> , CsSn <sub>2</sub> Br <sub>5</sub> and Cs <sub>2</sub> SnBr <sub>6</sub> .....	57
2.3 Cs <sub>3</sub> Bi <sub>2</sub> (I <sub>1-x</sub> Br <sub>x</sub> ) <sub>9</sub> .....	69
3. High pressure studies .....	100
3.1 MASnBr <sub>3</sub> and CsSnBr <sub>3</sub> .....	104

4.	Physical modulation techniques .....	127
4.1	High-pressure quenching .....	128
4.1.1	MAPI .....	128
4.2	Extended ball milling .....	143
4.2.1	MAPI and $\text{PEA}_2\text{PbBr}_4$ .....	144
5.	Future perspectives .....	166
6.	Bibliography .....	168

# ABSTRACT

The development and the increasing application of renewable sources are two pivotal points of the solutions set for the huge climatic challenge that all the world is facing nowadays.

Apart from the classical, well-known, and widespread silicon-based photovoltaic panels, one of the most flourishing fields in terms of renewable sources is that of metal halide perovskites (MHPs).

The enormous attractiveness of these materials relies on their outstanding optoelectronic properties and their applicability in many different fields. In fact, they can be largely employed as low-cost tunable light adsorbers in several optoelectronic devices such as LEDs, lasers, photodetectors, transistors, and so on.

The extreme tunability of MHPs is due to their structure, and consequently their properties' ease of modification. However, while there are several studies about chemical modulations through alloying, physical tuning methods are not often taken into consideration.

All MHPs are constituted by a network of  $BX_6$  octahedra (where B is a metal cation and X a halide anion): when they share 6, 4, 2, and 0 corners the structure is respectively called 3D, 2D, 1D, and 0D perovskite.

However, even though only limited amounts of Pb are implemented in solar cells, there is a potential risk of harm to humans and the environment. To overcome the problem, researchers are currently trying to substitute Pb with other suitable elements to develop novel, low-cost, non-toxic, and environment-friendly perovskite materials, that could be

possibly capable of various applications with superior performances and long-term stability.

In almost all the devices, the perovskite is present in form of thin film, therefore in literature many different growing methods can be found, either solution or vapor-based. Solution based ones are the most applied, but even the optimized techniques are affected by many shortcomings, such as: i) a lack of control over the low-temperature crystallization process, which is affected by many factors (i.e. solvents and precursors, surface properties of the substrate, solvent evaporation during the deposition and annealing conditions), and often leads to poor reproducibility in properties (i.e. morphology, thickness, crystallinity, and crystal size) that crucially influence the device performances; ii) the solvent employed in depositing a perovskite layer washes away the underlying ones, so the sequential film deposition and the deriving perovskite-perovskite heterostructures are very difficult to realize; iii) the complex fluid dynamics during the scale-up of solution methods does not permit the growth of uniform thin films in panel-size substrates due to the many intermediate phases that coexist during the crystallization process; iv) the common wet-chemistry protocols used for hybrid organic-inorganic phases do not assure good results in totally inorganic perovskite deposition, mainly because of the poor solubility in apolar solvents (e.g. dimethylformamide or dimethyl sulfoxide) of many halide precursors necessary to insert the A-site cation into the structure.

The main aims of this thesis are: i) the realization of new approaches to tune, in a stable way, the optical and structural properties of perovskites in order to extend their range of applications; and ii) the development of different environmental-friendly scale-up methods suitable to prepare perovskite phases for optoelectronic devices and to stabilize

metastable phases. For these purposes, we focused on industrial types of equipment and techniques that could fit our scopes.

The first part of this work is about the employment and optimization of a vapor-based technique to deposit metal halide perovskites thin films.

At the beginning of this work, it was possible to find in literature only a few papers about perovskite thin films growth by vapor-based techniques: most of them dealt with co-deposition methods and in only one Pulsed Laser Deposition (PLD) was applied. Today vapor-based methods for the fabrication of perovskite films are not yet widespread due to the relatively more complex infrastructures required with respect to spin-coating approaches.

The most employed physical vapor deposition method still consists of different variations of thermal evaporation, therefore we decided to explore radio-frequency magnetron sputtering because of the advantages of simple equipment, easy control, large coating area, and strong adhesion.

By means of this technique, a large number of thin films can be prepared at relatively high purity, high speed, low temperature, and low cost. The radio-frequency source does not require an electrically conductive target, therefore any material can be deposited, while the magnetron enhances the switching on of the plasma and permits a more efficient deposition thanks to the interaction between the magnetic and the electric fields.

The second section of the thesis focuses on preliminary in-situ high-pressure studies of metal halide perovskites at large facilities.

This investigation of MHPs is relatively recent and mainly focused on methylammonium lead iodide perovskite ( $\text{MAPbI}_3$ ) and, while studies of temperature dependence modification and chemical tuning strategies exist, the knowledge of pressure-induced effects remains scarce.

Understanding the correlations between pressure-induced structural and electronic changes could allow us to more precisely tune the properties of a material through compression. In addition, these studies could permit the discovery of new phases that subsequently could be stabilized at ambient conditions (and eventually produced on a large scale).

The last part of this work is focused on the tuning of metal halide perovskites by the means of two industrial physical modulation techniques: spark plasma sintering and ball-milling. We could obtain interesting results with both these approaches, reporting, for example, the first evidence of high-pressure quenching thanks to a homemade apparatus, and by providing insights into the role of extended ball-milling in the phase stability and optical properties of 3D and 2D MHPs.

# INTRODUCTION

The multilateral climate change process, the air pollution, and the gradual but inexorable exhaustion of fossil fuels are now an established reality.

Various initiatives sprung up to contrast the enormity of these problems, one above all, the COP21 Paris Agreement adopted in 2015 by 196 Parties.

Since then a global “Energy Transition to Net Zero Carbon” started with the main aim of downshifting the fossil fuel production and employment to stay within the carbon emissions budget to limit global warming to less than  $1.5\text{ }^{\circ}\text{C}^1$ .

In order to gain these preset goals, the development and the increasing application of renewable sources and devices represent a key irreplaceable point.

One of the most flourishing fields in terms of renewable sources is that of photovoltaic panels.

Currently, the most common ones contain crystalline silicon (c-Si) wafers, granting high power conversion efficiencies, proven manufacturability, and abundant material sources. However, unfortunately, the fabrication process necessary to obtain good quality c-Si panels is complex, expensive, and leads to a significant amount of  $\text{CO}_2$  emissions.

Industries and scientists recently tried to find better photovoltaic alternatives to overcome c-Si panels problems: among the others (such as organic solar cells and dye-sensitized solar cells), Metal Halide Perovskites (MHPs) based panels burstingly stand out.

The enormous attractiveness of these materials relies on their outstanding optoelectronic properties and their extreme tunability and applicability in many different fields in addition



to the photovoltaic one. In fact, they can be largely applied in several devices such as LEDs, lasers, photodetectors, transistors, and so on.

Most of their qualities are due to the atomic arrangement of these materials that is the one of perovskite crystal structure.

## 1.1 Perovskites

The first perovskite was the mineral  $\text{CaTiO}_3$  found in the Ural Mountains of Russia in 1893 by the mineralogist Gustav Rose and named after Count Lev Alekseyevich von Perovski, that was a mineralogist too (Figure 1.1).

Nowadays the term identifies one of the most structurally abundant families of materials that have a structure that is somehow similar to the original one.

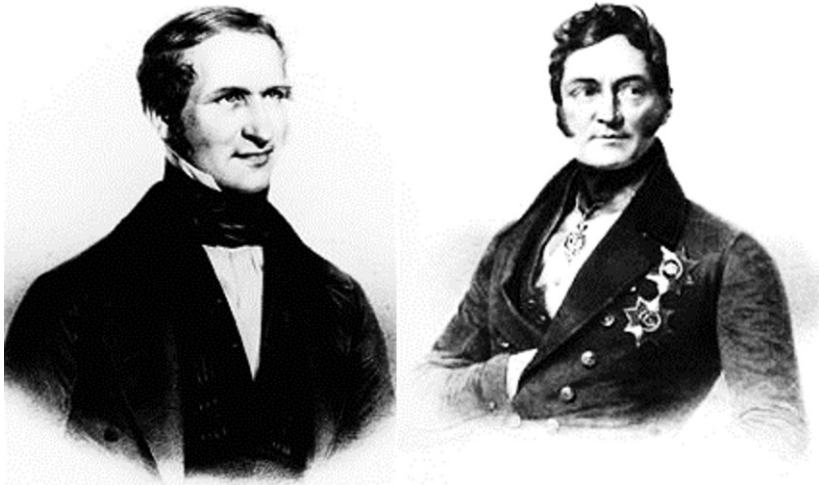


*Figure 1.1* Gustav Rose on the left and Lev Perovski on the right.

Perovskites can be natural or synthetic and can exhibit many different properties, such as colossal magnetoresistance, superconductivity, ferroelectricity, charge ordering, dielectric properties, and so on.

The most promising subgroup for optoelectronic devices is that of MHPs<sup>2,3</sup>, containing both fully inorganic and hybrid organic-inorganic materials.

### 1.1.1 Crystal structure and stability factors

The perovskite crystal lattice is perhaps the most adaptable one and it is defined as a network of corner-sharing  $\text{BX}_6$  octahedra with A cations in between, that crystallize with a general  $\text{ABX}_3$ , or equivalent, stoichiometry<sup>4</sup>.

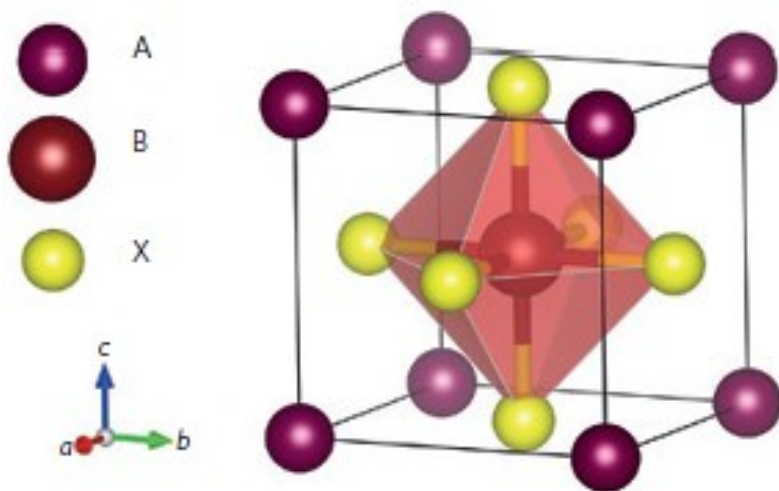


*Figure 1.2* Schematic representation of 3D- $\text{ABX}_3$  metal halide perovskite structure.

When the octahedra share all their corners the structure is called 3D perovskite (in Figure 1.2 the unit cell of the classical 3D perovskite is shown). If they share 4, 2, and 0 corners instead they are respectively named 2D, 1D, and 0D perovskites<sup>5</sup>.

Deviations from the standard stoichiometry can be obtained when the A and B cation sites become partially or fully vacant (vacancy-ordered perovskites), or when they are replaced by a combination of other cations with different valences but with an overall neutral charge balance, forming double or quadruple perovskites<sup>4</sup>.

The aristotype (*the highest symmetric structure of the group*) belongs to the  $Pm\bar{3}m$  cubic space group, but the vast majority of perovskites have a reduced symmetry, due to many reasons: lattice distortions, distorted octahedra, ordered cations, vacancies, the presence of organic cations, or inorganic clusters<sup>4</sup>.

In the general formula  $ABX_3$  A is a monovalent cation ( $A^+$ ), B a divalent one ( $B^{2+}$ ) and X represent a halogen anion ( $X^-$ ) (see Figure 1.2)

As already mentioned, there are many variations (see Figure 1.3): from the “classical” stoichiometry<sup>4</sup>:

- *Antiperovskites*, with A being a monovalent metal, X a halide, and B a chalcogenide
- *Inverse perovskites*, in which A cation is very large and has a higher oxidation state than the small B cation
- *Vacant perovskites*, with A-site vacant  $BX_3$  octahedra
- *Ordered* (in sense of replacing) *perovskites*, here the B cations are heterovalently replaced by a combination of two or more cations that are located at specific crystallographic sites
- *Vacancy-ordered perovskites*, with the B-site cation partially replaced with a vacancy

However, opinions are conflicting about some materials that many scientists consider perovskites despite not falling in the previous categories, while others talk about them as “pseudo-perovskite structures” or “perovskite-like structures”.

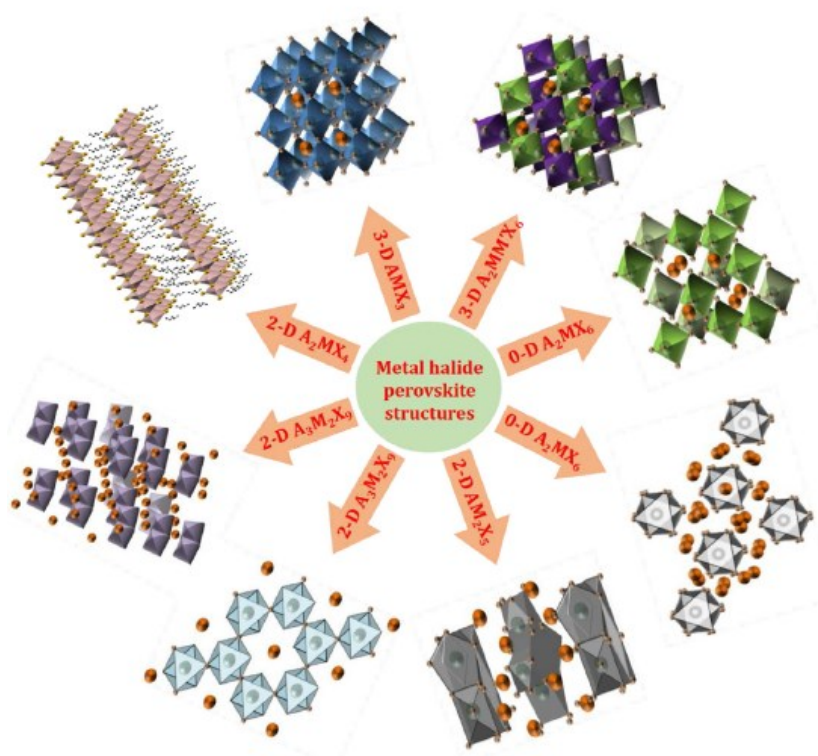


*Figure 1.3* Schematic representation of different metal halide perovskite crystal structures of 3-D cubic-phase  $AMX_3$ , 2-D  $A_2MX_4$ , 2-D  $A_3M_2X_9$ , 2-D  $AM_2X_5$ , 0-D  $A_4MX_6$ , and 3-D double perovskites  $A_2MM'X_6$ . Reprinted with permission by ref. 4, Copyright © 2020 American Chemical Society.

## Tolerance and octahedral factors

The unusual adaptability of the perovskite crystal lattice often generated doubts about the structure stability, in simple terms: what can we put in a perovskite without destroying the structure? To predict the stability of a perovskite, two factors must be

considered as necessary but not sufficient conditions: the Goldsmith tolerance factor and the octahedral factor.

The first is a figure of merit that indicates whether ternary metal halides can or not form geometrically stable  $ABX_3$  perovskites:

$$t = \frac{(r_A + r_X)}{\sqrt{2}(r_B + r_X)}$$

where  $r_A$ ,  $r_B$  and  $r_X$  are the radii of the respective ions<sup>6</sup>. The accepted values of  $t$  are between 0.7 and 1.1. The more  $t$  moves away from the range, the more the structure deforms.

The octahedral factor relies instead on the stability of the  $BX_6$  octahedrons:

$$\mu = \frac{r_B}{r_X}$$

where  $r_B$  and  $r_X$  are the radii of the respective ions. The correct range of  $\mu$  varies from 0.377 and 0.895 and the principle is the same as the tolerance factor, but applied to octahedrons<sup>6</sup>.

## 1.1.2 Optoelectronic properties

The optoelectronic properties are all those properties due to the quantum mechanical effects of light on electronic materials, especially semiconductors, sometimes in presence of electric fields.

Historically, the interest in the electronic properties of perovskites rose after the demonstration of ferroelectricity in

BaTiO<sub>3</sub> in the mid-1940s<sup>7</sup>. Shortly thereafter, the vibrant colors of CsPbX<sub>3</sub> compounds motivated the first study of metal halide perovskite electronic properties, which revealed a frequency-dependent photoconductive response<sup>8</sup>.

The transition to MHP optoelectronics began with pioneering works on hybrid organic-inorganic 2D systems. Of particular interest was the natural self-assembly of quantum well (QW) structures in (RNH<sub>3</sub>)<sub>2</sub>MX<sub>4</sub> compounds<sup>9</sup>.

A transition from semiconducting to metallic behavior as a function of the number of adjacent inorganic layers in layered tin-based hybrid perovskites highlighted the electronic tunability of these materials, pointing out their applicability in devices such as organic-inorganic light-emitting diodes (OILEDs) and as semiconducting channels in thin-film field-effect transistors (TFTs)<sup>10–12</sup>.

Propelling current interest in MHPs optoelectronic properties is their recent success as low-cost, tunable light absorbers in next-generation photovoltaics (PVs) due also to the remarkable performance of perovskite solar cells (PSCs), with record laboratory-scale power conversion efficiency now certified at 25.5% (<https://www.nrel.gov/pv/cell-efficiency.html>).

To check if a material is good or not for optoelectronic devices it is required to define the bandgap (or energy gap,  $E_g$ ), photoluminescence (PL) response, and carrier lifetime/diffusion length.

The **energy gap** is an energy range in which no electronic state can exist and corresponds to a value in electronvolts referring to the energy difference between the top of the valence band and the bottom of the conduction band.

A material can have a direct and/or indirect  $E_g$ : if the lowest energy state in the conduction band and the highest one of the

valence band have the same momentum, the bandgap is direct, otherwise, it is indirect.

For the first, valence electrons can be directly excited into the conduction band by a photon whose energy is larger than the bandgap. In the presence of an indirect bandgap the photon must both be involved in a transition from the valence band top to the conduction band bottom.

Speaking about device applications, the energy gap matches the *emission* energy of a LED or a laser, and it is equal to the energy of the photons that a solar cell *adsorbs* (so, if we consider the solar spectrum, the ideal bandgap for solar cells is around 1.4 eV).

In materials with a large exciton binding energy, it is possible to observe two different bandgaps: "optical bandgap" and "electrical bandgap" (or "transport gap"). The optical one is the threshold for photons to be absorbed, while the electrical one is the threshold for creating an electron-hole pair that is not bound together. The first is found at lower energy<sup>13</sup>.

The measure of the **photoluminescence**, that is the light emission after the absorption of electromagnetic radiation, gives much information about a material: the pure PL, the TR-PL (time-resolved photoluminescence), and the PLQY (photoluminescence quantum yield) permit to gain information about the  $E_g$ , the recombination mechanisms, and the carrier density.

Carriers interesting for optoelectronic devices are the electronic ones: separate couples of electrons and holes that form when a material is struck by light at proper energy.

The recombination mechanisms are all the processes that re-put the couple together and are usually an obstacle for a good optoelectronic device because they affect the carrier lifetime and



the diffusion length: the more these last two are high, the more the electrons and the holes can be separated and collected by the electrodes to be used as electric energy. In fact, the electron-hole diffusion lengths must be much longer than the film thickness required to obtain complete solar light absorption.

On the other side, the carrier density helps to indicate which is the best application for a material: if it is low the material, e.g. in solar cells or lasers<sup>14</sup>.

It is challenging to properly predict and comprehend the electronic structure and the deriving properties of these materials.

Halide perovskites most relevant for optoelectronics, namely those with main group metal centers, are direct gap semiconductors with strong band-edge optical absorption and luminescence. The direct gap nature of MHPs is a valid generalization, but recent calculations suggest there may be subtle yet important exceptions that arise in non-centrosymmetric hybrid compounds<sup>15</sup> (as evidenced in Table 1).

*Table 1.1* Band Gaps ( $E_g$ ) for Select MHPs with variable chemistries and dimensionality

<b>Compound</b>	<b><math>E_g</math> (eV)</b>	<b>Type</b>	<b>Dimensionality</b>
$\text{CH}_3\text{NH}_3\text{PbI}_3$	1.61	Direct	3D
$\text{CH}_3\text{NH}_3\text{GeI}_3$	1.90	Direct	3D
$(\text{CH}_3\text{NH}_3)_3(\text{C}_9)_2\text{Pb}_4\text{I}_{13}$	2.03	Direct	2D
$(\text{CH}_3\text{NH}_3)_2(\text{C}_9)_2\text{Pb}_3\text{I}_{10}$	2.17	Direct	2D
$\text{C}(\text{NH}_2)_3\text{GeI}_3$	2.70	Indirect	1D
$(\text{NH}_2\text{Cl}=\text{NH}_2)_3\text{PbI}_3$	3.10	Direct	1D
$(\text{CH}_3\text{NH}_3)_4\text{PbI}_6 \cdot 2\text{H}_2\text{O}$	3.87	Direct	0D

The electronic structure near the band edge is primarily dictated by the basic  $\text{BX}_6$  building blocks, while the A-site component's

influence on octahedral orientation and dimensionality leads to profound effects on electronic structure<sup>15</sup>.

Structures containing smaller A-site cations with reduced cell volumes should exhibit smaller band gaps, but for many MHPs, the situation is more complex since the size and nature of A-site cations drive reorientation of the octahedral units. Therefore the A cation acts as a templating agent for the inorganic motif<sup>15</sup>.

However, it is not sufficient to take into account both octahedra and the A-site cation, because perovskites are affected by dynamic disorder too, that correspond to structural reorientations and distortions occurring when external physical conditions (such as temperature and pressure) or morphology (single crystal-bulk-film or different thickness and roughness) change<sup>15</sup>. In fact, the carrier lifetime is also strongly dependent on the polycrystalline nature of the film and the defect density or electronic trap density within the films<sup>16</sup> (as evidenced in Table 1.2).

*Table 1.2* Examples of measured mobilities and diffusion lengths for various metal halide perovskites

<b>Compound</b>	<b>Sample type</b>	<b>Mobility (cm<sup>2</sup>V<sup>-1</sup>s<sup>-1</sup>)</b>	<b>Diffusion length (μm)</b>
CH <sub>3</sub> NH <sub>3</sub> PbI <sub>3</sub>	Thin film (solution)	1.4	0.13
CH <sub>3</sub> NH <sub>3</sub> PbI <sub>3</sub>	Single crystal	2.5	2-8
CH <sub>3</sub> NH <sub>3</sub> PbBr <sub>3</sub>	Thin film (vapor assisted)	8.9	1.06
CH <sub>3</sub> NH <sub>3</sub> PbBr <sub>3</sub>	Single crystal	24	4.2

Significant changes in optical properties occur also upon reduction in dimensionality (from 3D to 2D, 1D, and 0D) leading to intensified oscillator strength and optical nonlinearities<sup>15</sup>.

Anyway, the carrier recombination is predominantly radiative, with room-temperature photoluminescence quantum efficiencies of up to 70%<sup>16</sup>, amplified spontaneous emission (ASE) and lasing which have been reported for both bulk and nanostructured hybrid MHPs<sup>17–19</sup>, with favorable properties of MHPs for lasing, including high PLQY at relatively large carrier densities and long excited-state lifetime<sup>15</sup>.

The high carrier mobilities compared to other solution-processed materials also opens the possibility for electrically-pumped lasing<sup>20</sup>, the considerable diffusion length is interesting in photovoltaic devices implementation, while the extreme energy gap variation makes perovskites perfect for LED, photocatalysis, and photosensoristic applications.

### **1.1.3 Lead-free trend**

The most extensively studied and also most efficient perovskite absorber materials are based on semiconducting (hybrid) lead halide perovskites adopting an  $ABX_3$  structure (see Figure 1.4), where A is a monovalent cation, B is a divalent  $Pb^{2+}$  metal cation and the X-site of the perovskite structure is occupied by halide counterions ( $X = Cl^-, Br^-, I^-$ )<sup>21</sup>.

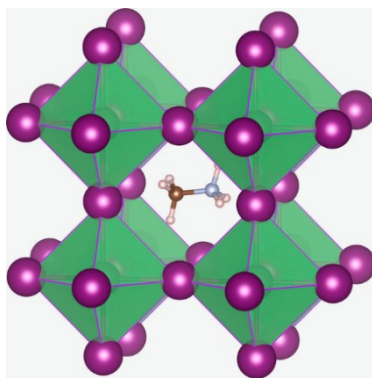


*Figure 1.4* Schematic representation of MAPbI<sub>3</sub> (MA = methylammonium)

However, the use of lead in electronics is restricted to <1000 ppm (0.1 wt%) by the EU's Restriction of Hazardous Substances (RoHS) directive due to the toxicity of lead<sup>22</sup>.

In fact, the current limitations impeding the commercialization of lead-based halide perovskite solar cells are:

- the toxicity, bioavailability, and probable carcinogenicity of lead and lead halides
- the water solubility of lead that might contaminate water supplies
- the chemical instability under ambient conditions, especially in the presence of heat, air, moisture, and event light illumination<sup>23–25</sup>.

Therefore, even though only low amounts of Pb are implemented in solar cells, there is a potential risk of harm to humans and the environment<sup>26–28</sup>.

To overcome the problem, researchers are currently searching for a potential substitute of Pb with other suitable elements to develop novel, low-cost, non-toxic, and environment-friendly perovskite materials such that they are capable of various

applications with superior performance and long-term stability<sup>29–31</sup>.

Recently, lead-free metal halide perovskite (LFHP) materials have shown their capability as potential materials for various optoelectronic device applications (see Table 1.3), and their current progress is quite impressive. LFHP materials are a common group of compounds with the chemical formula  $A_xM_yX_z$  ( $x, y, z$  depends on the structural dimensionality), where A is an organic or inorganic cation, M is a metal cation, and X is a halide anion<sup>32</sup>.

LFHPs could be distinguished into the following four categories depending on their crystal structure and the valence of the metallic cation:

- **divalent metal cation perovskites** = contain M in +2 oxidation state (Sn, Ge, Mg, Ca, Sr, Cu, Fe, Pd, Eu) and present  $AMX_3$  stoichiometry or the layered perovskites stoichiometry  $A_2A'_{n-1}M_nX_{3n+1}$ , in which A' is a long-chained organic cation that does not fit in the  $[MX_6]^4$  cavity
- **trivalent metal cation perovskites** = with M in 3+ oxidation state (Sb, Bi) and  $A_3M_2X_9$  stoichiometry
- **tetravalent metal cation perovskites** = present M in 4+ oxidation state (Sn, Ge, Pd, Te, Ti) and show  $A_2MX_6$  stoichiometry
- **double perovskites** = contain M in both +1 and +3 oxidation state (+1: Cu, Ag, Au; 3+: In, Bi, Sb) and present  $A_2MM'X_6$  stoichiometry<sup>21,32</sup>

*Table 1.3* Dimensionality, optical data and the highest obtained power conversion efficiencies of the currently most promising lead-free halide perovskites

Compound	Dimensionality	Band gap (eV)	PCE%
CH <sub>3</sub> NH <sub>3</sub> SnI <sub>3</sub>	3D	1.27-1.35	5.23
CH <sub>3</sub> NH <sub>3</sub> GeI <sub>3</sub>	3D	2	0.2
(CH <sub>3</sub> (CH <sub>2</sub> ) <sub>3</sub> NH <sub>3</sub> ) <sub>2</sub> CuBr <sub>4</sub>	2D	1.76	0.63
Rb <sub>3</sub> Sb <sub>2</sub> I <sub>9</sub>	2D	2.1	0.66
Cs <sub>3</sub> Bi <sub>2</sub> I <sub>9</sub>	0D dimer	2.2	1.09

Sn<sup>2+</sup> metal cation (ionic radius of 110 pm) is the most suitable candidate for substitution with Pb<sup>2+</sup> cation (ionic radius of 119pm) in the perovskite structure because of very similar valence electronic configuration and nearly similar ionic radius<sup>32</sup>.

Compared to lead, tin has lower uptake ability by plants which suggests that its use could avoid serious contamination issues in case of leaking in electronics<sup>22</sup>.

The corresponding perovskites analogs MASnI<sub>3</sub>, FASnI<sub>3</sub>, and CsSnI<sub>3</sub> have a direct bandgap of around 1.20, 1.41, and 1.3 eV, respectively, which is lower than their Pb-based perovskite counterparts (see Table 1.4 and Table 1.5)<sup>33,34</sup>.

The main draw-back of these tin halide perovskites is the chemical instability of the divalent metal cation, which oxidizes from 2+ to 4+ under ambient conditions<sup>35,36</sup>. As a consequence, the oxidation of Sn<sup>2+</sup> to the chemically more stable Sn<sup>4+</sup> leads to the possible formation of a 2D A<sub>2</sub>SnX<sub>6</sub> perovskite structure with an increase of the bandgap.

Table 1.4 Structural and optical data of tin halide perovskites and the highest obtained power conversion efficiencies

Compound	Crystal system	Dimensionality	Band gap (eV)	PCE%
CH <sub>3</sub> NH <sub>3</sub> SnI <sub>3</sub>	Pseudocubic	3D	1.27-1.35	5.23
CH <sub>3</sub> NH <sub>3</sub> SnI <sub>3</sub>	Tetragonal	3D	1.21-1.35	6.4
CH <sub>3</sub> NH <sub>3</sub> SnBr <sub>3</sub>	Pseudocubic	3D	2.15-2.2	4.27
CsSnI <sub>3</sub>	Ortorombic	3D	1.27-1.31	3.31
CsSnBr <sub>3</sub>	Cubic	3D	1.75-1.8	2.1

Table 1.5 Dimensionality and optical data of lead halide perovskites and the highest obtained power conversion efficiencies

Compound	Dimensionality	Band gap (eV)	PCE%
CH <sub>3</sub> NH <sub>3</sub> PbI <sub>3</sub>	3D	1.56-1.59	19.89
CH <sub>3</sub> NH <sub>3</sub> PbBr <sub>3</sub>	3D	2.2	0.82
CsPbI <sub>3</sub>	3D	1.73	2.9
CsPbBr <sub>3</sub>	3D	2.30-2.36	6.7

Though there are so many efforts were devoted to developing LFHP, a systematic understanding of the properties of the materials with the fabrication method was lacking. The materials' properties largely depend on the fabrication methods, especially for optoelectronic device applications<sup>37,38</sup>.

To produce any perovskite-based device is fundamental that the active material is in form of thin film, therefore any fabrication process has to include at least one deposition method.



## 1.2 Thin films making techniques

Perovskite-based solar cells are primarily prepared in two device architectures. The first one has been derived from dye-sensitized solar cells using mainly mesoporous  $\text{TiO}_2$  as electron transport material and Spiro-OMeTAD (2,2',7,7'-tetrakis[N,N-di(4-methoxyphenyl)amino]-9,9'-spirobifluorene) as hole transport material. The other one is derived from organic solar cells where PEDOT : PSS (poly-3,4-ethylenedioxythiophene : polystyrenesulfonate) and PCBM ([6,6]-phenyl-C61-butyric acid methyl ester) are used as hole and electron transport layer, respectively<sup>32</sup>.

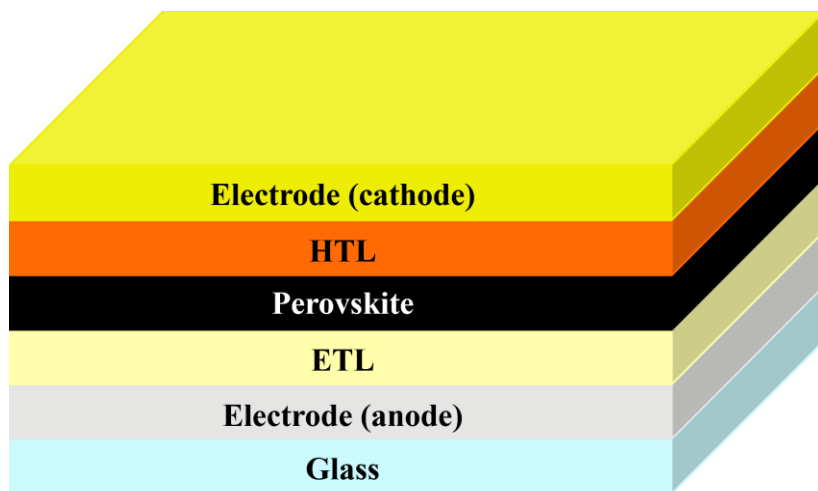


*Figure 1.5* General scheme of perovskite solar cell; HTL= Hole Transport Layer; ETL= Electron Transport Layer

Therefore, it is clear that in solar cells, but also in many other devices (such as photosensors and photocatalysts), the perovskite should be present in the form of a thin film.

In literature many different growing methods can be found, either solution or vapor-based<sup>39</sup>.

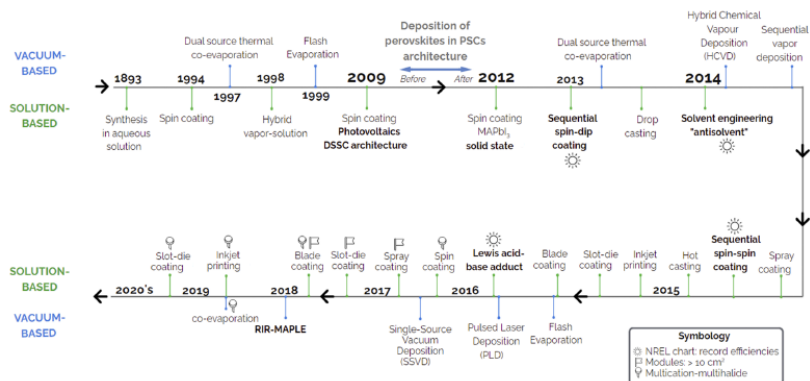


Figure 1.6 Timeline of thin-film fabrication methods for inorganic and hybrid halide perovskites. Reprinted with permission by ref. 39, Copyright © 2020 APL Materials.

## 1.2.1 The flaws of solution methods

Solution-based deposition methods have been the most explored routes to deposit halide perovskites, especially as proof of concept studies of a full breadth of optoelectronic devices, namely, solar cells, LEDs, lasers, photodetectors, X-ray detectors, waveguides, and resistive memory devices.

From 1994 to date, works about different liquid-based techniques have been published (see Figure 1.6): spray coating<sup>40,41</sup>, hot casting<sup>42</sup>, inkjet printing<sup>43</sup>, slot-die coating<sup>44,45</sup>, blade coating<sup>46</sup>, and drop casting<sup>47</sup> (schemes in Figure 1.7).

In 1994, the spin coating method was first conceived to deposit hybrid  $(\text{C}_6\text{H}_5\text{C}_2\text{H}_4\text{NH}_3)_2\text{PbI}_4$  layered perovskites in electroluminescence (EL) devices and now it is still the most straightforward and successful procedure to grow thin films from precursor inks<sup>39</sup>.

However, solutions containing inorganic and organic salts have shown several bottlenecks during crystallization of perovskite thin films due to the different miscibility of the components, leading to different crystallization rates in a single film<sup>39</sup>.

Moreover, pinholes and cracks were often observed because of inadequate control over crystal growth. The perovskite crystallization process is affected by many other parameters such as the composition and concentration of the precursors' solution, the spin speed, the medium temperature, and the solvent vapor pressure inside the glovebox<sup>48</sup>.

To tackle this, strategies such as gas-assisted and solvent extraction approaches were implemented to quickly remove the solvent from the precursor solution, improving the crystallization process, but many issues remain unsolved<sup>49,50</sup>.

Two-step spin coating, interdiffusion, and vapor-assisted solution process (VASP) have demonstrated improved morphology and usually higher solar cell efficiency as compared with the single-step spin coating method<sup>51,52</sup>.

However, two-step methods still need to solve the challenges associated with the proper diffusion of the organic component while reacting with the compact inorganic film, since they consist in firstly depositing the inorganic precursor and then the organic one over the first (instead of depositing them together).

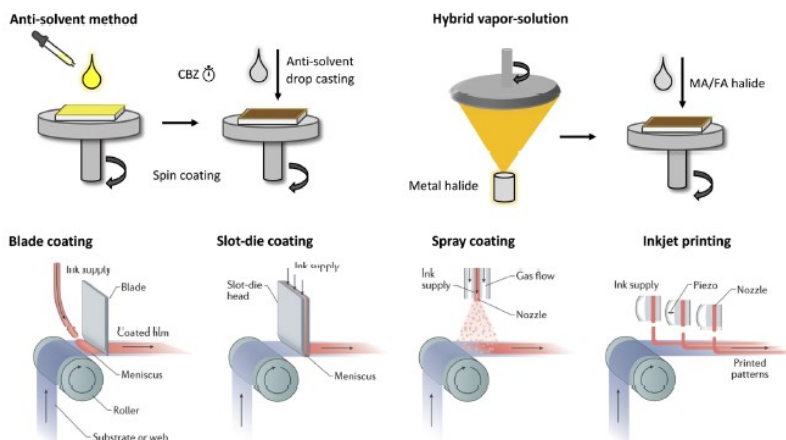


*Figure 1.7* Schemes of a selection of many solution-based thin films deposition methods. Reprinted with permission by ref. 39, Copyright © 2020 APL Materials, and ref. 62 of ref. 39, Copyright © 2020 Springer Nature.

All in, even optimized solution-process methods are affected by shortcomings. One is a lack of control over the low-temperature crystallization process, which is affected by many factors such as solvents and precursors, surface properties of the substrate, solvent evaporation during the deposition and annealing conditions, often leading to poor reproducibility of films morphology, thickness, crystallinity, and crystal size, properties that in turn have crucial influences on the photovoltaic performance. The second major shortcoming, more fundamental than the first one, is that sequential film deposition from solution cannot produce perovskite-perovskite heterostructures, since the solvent employed in depositing subsequent layers washes away the underlying ones. As a consequence, multijunction tandem solar cells and p-n junctions fully based on MHPs are advancing very slowly<sup>53</sup>.

In addition, the complex fluid dynamics during upscalable solution methods is a hurdle for uniform thin films in

module/panel-size substrates due to the many intermediate phases that coexist during the crystallization process<sup>54,55</sup>.

In addition, the common wet-chemistry protocols used for hybrid organic-inorganic (HOIP) phases do not reliably assure good results in totally inorganic perovskite deposition: for example because of the poor solubility in apolar solvents (such as dimethylformamide or dimethyl sulfoxide) of many halide precursors of inorganic metals<sup>56</sup>.

All the overmentioned considerations are more or less valid for hybrid methods too, because they consist of mixed procedures exploiting both vapor and liquid-based methods (see an example in Figure 1.8): the result is an upgrade of liquid-based ones but without the whole set of advantages given by the vapor based<sup>39</sup>.

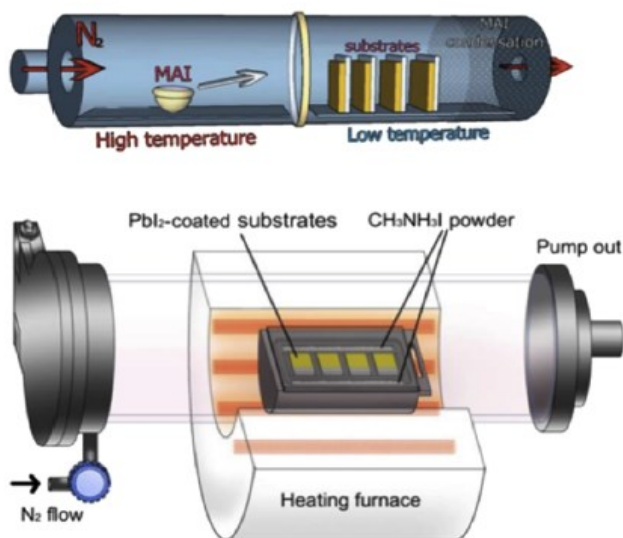


*Figure 1.8* Two examples of equipment for HCVD (Hybrid Chemical Vapor Deposition): firstly a solution method is applied to deposit the inorganic part of the MAPbI<sub>3</sub> hybrid halide perovskite, then the organic part is grown by CVD Reprinted with permission by ref. 66, Copyright © 2020 APL Materials.

## 1.2.2 Vapor-based techniques

Many different vapor-based deposition methods are potentially available in depositing perovskite thin films and they can be divided into two main categories: CVD (Chemical Vapor Deposition) and PVD (Physical Vapor Deposition).

The chemical techniques rely on one (or more) volatile precursor(s) that reacts at high temperature and form a product that finally deposits on a substrate. It is possible to classify them into 4 groups:

- Thermal CVD: <sup>57</sup>
- Aerosol Assisted CVD (AACVD), that occurs under ambient pressure and requires moderately volatile precursors<sup>58</sup>
- Photo Assisted CVD (PACVD), in which the deposition is helped by a light source such as a Hg-vapor lamp<sup>59</sup>
- Plasma Enhanced CVD (PECVD), in which the chemical reactions occur after the switching on of a plasma of the reagent(s)<sup>60</sup>

The physical methods occur in vacuum: the starting material passes from a condensed to a vapor phase and it is subsequently deposited on the substrate. The main ones are:

- Vacuum Evaporation, that needs high vacuum ( $10^{-8}$  atm) and heating or an electron stream to sublimate the target material and lay it down on a substrate (see Figure 1.9)
- Pulsed Laser Deposition, that is assisted by a High-Density Laser Beam ( $10^9$  W/cm<sup>2</sup>) which removes material from a target forming a 12000 K plasma that is subsequently focused by magnetic lenses to be deposited<sup>61</sup> (see Figure 1.10)
- Radio Frequency Sputtering, successfully employed in this work

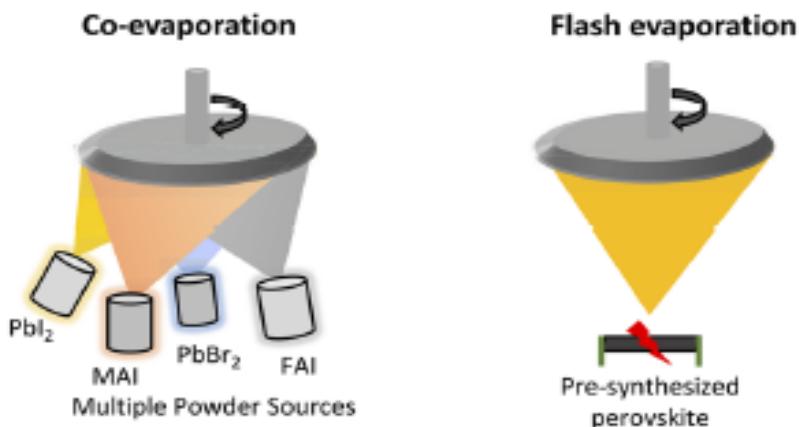


Figure 1.9 Two schemes of vacuum methods: co-evaporation on the left, and flash evaporation on the right. Reprinted with permission by ref. 39, Copyright © 2020 APL Materials.

At the beginning of this work, it was possible to find in literature only a few papers about thin films growth by vapor-based techniques: most of them were about co-deposition methods<sup>59,62–65</sup> and in only one PLD was applied<sup>61</sup>.

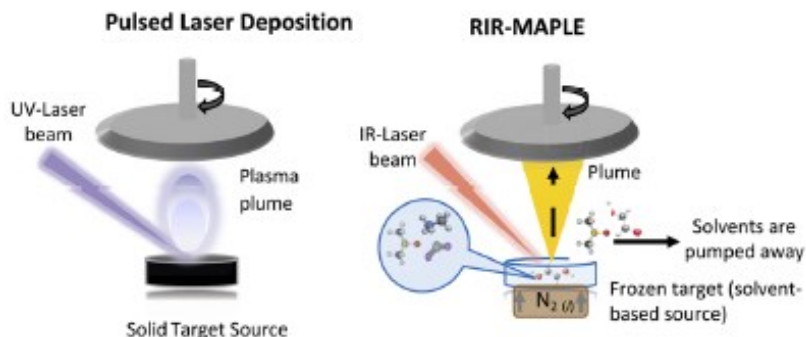


Figure 1.10 Pulsed Laser Deposition and Resonance Infrared Matrix-Assisted Pulsed Laser Evaporation. Reprinted with permission by ref. 39, Copyright © 2020 APL Materials.

Today vapor-based methods for the fabrication of perovskite optoelectronics are not yet widespread due to the rather complex

infrastructures required. This explains the prevalent adoption of lab-scale, solution-processing methods by the research community working in the field. Anyway, the large discrepancy in the number of groups working on solution processing and vapor deposition is not so evident in the best performances obtained<sup>66</sup>.

The most widespread PVD method still consists of different variations of thermal evaporation<sup>58,67</sup> (see an example in Figure 1.11), such as LPCVD<sup>68,69</sup> and AACVD<sup>70,71</sup>, and only one group worked on CsPbBr<sub>3</sub>-CsPb<sub>2</sub>Br<sub>5</sub> phases by the means of an RF magnetron sputtering equipment<sup>72</sup>.

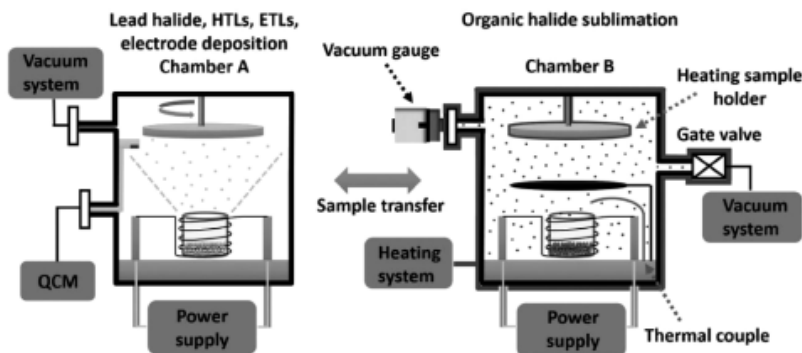


Figure 1.11 Example of sequential thermal evaporation. Reprinted with permission by ref. 48, Copyright © 2020 Chem. Rev.



## 1.3 Perovskites modulation

There are many ways to tune metal halide perovskites properties. All of them can be divided into two groups: chemical modulation techniques or physical modulation techniques.

The first ones, as the word “chemical” suggests, involve a change in the chemical content of the material: for instance, we are speaking about an A cation substitution or a chemical doping.

The second ones involve instead a physical modification, such as a phase transition or a local distortion of the crystal structure.

Researchers have extensively dealt with chemical modulation techniques because this field does not require either special equipment or a “mixed” educational background: usually, it is sufficient to have a good chemical preparation and a little more than a hot plate and a spin coater, or a furnace (in terms of physical tools) to perform the substitution of any ion present in the structure of the perovskite<sup>73–78</sup>.

The most diffuse experimental procedures are:

- Liquid synthesis from solid precursors<sup>79</sup>, in which proper amounts (usually stoichiometric) of precursors are dissolved in solvent(s)
- Liquid synthesis with amine injection<sup>80,81</sup>, that involves the addition of the desired amine(s) after the dissolution in acid(s) of the solid precursor(s)
- Ionic exchange (usually for nanoparticles)<sup>82,83</sup>, in which a solid or liquid precursor is injected in a suspension of the starting perovskite and stirred (and possibly heated) for the time necessary to obtain the desired exchange

However, although these methods proved to be convenient for the research scale, the same cannot be asserted for the eventual production one, as the vast majority of examples in literature consist of solution techniques, with all the struggles mentioned in paragraph 1.2.1.

These reasons, the lack of examples in the literature, and the availability of the right equipment let us towards the application of the physical methods.

# RF MAGNETRON SPUTTERING

Sputter deposition is a physical vapor deposition (PVD) method to grow thin films. The general sputtering method can be used to prepare a variety of materials such as metals, semiconductors, insulators, etc., and has the advantages of simple equipment, easy control, large coating area, and strong adhesion<sup>84</sup>.

Briefly, this involves ejecting material from a “target”, that is a source, onto a “substrate”: the application of a potential difference between a cathode (covered with a target material) and an anode (usually in the form of a ferrule and set at a defined distance) ionizes the inert gas particles of the rarefied atmosphere of the chamber, causing their collision to the target and the following ejection of material (see Figure 2.1).

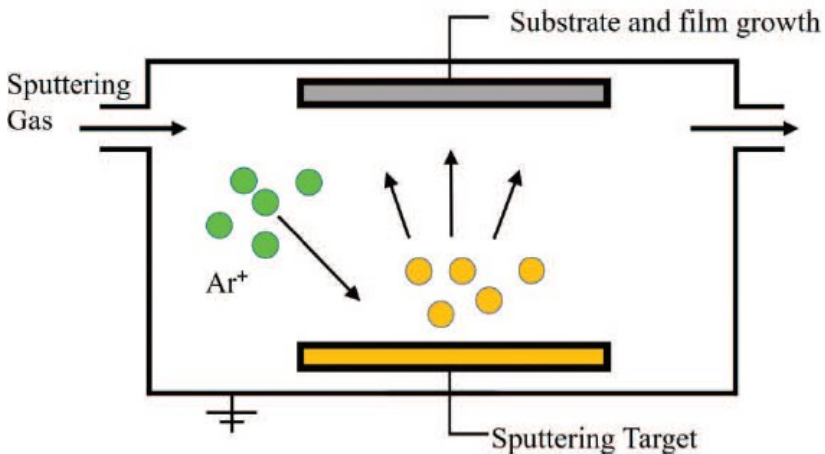


Figure 2.1 Sputtering scheme. Reprinted with permission by ref. 84, Copyright © 2020 IntechOpen.

The addition of a magnetron was developed in the 1970s and is the dominant method to grow thin films because a large number of them can be prepared at relatively high purity, high speed, low temperature, and low cost<sup>85,86</sup>.

The magnetron (see Figure 2.2) is based on the interaction between the magnetic field and the electric field that causes the electrons to spiral in the vicinity of the target surface, thereby increasing the probability that electrons will strike the argon gas to generate ions. The generated ions collide with the target surface under the action of an electric field to sputter the target<sup>84</sup>.

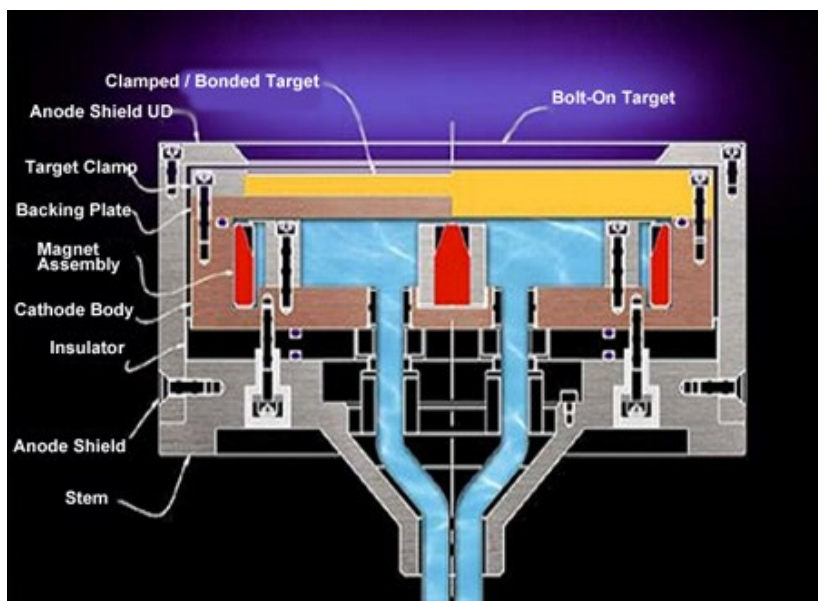


Figure 2.2 Scheme of a magnetron-holding cathode. Reprinted with permission by ref. AngstromSciences, Copyright © 2020.

It is possible to apply different sources. The main advantage of the radio frequency source is that it does not require an electrically conductive target. Therefore, any material can be

theoretically sputter-deposited using RF magnetron sputtering<sup>84</sup>, also because the technique can be reactive or non-reactive.

Due to all its positive features, RF magnetron sputtering can be employed in many fields, among the others:

- Renewable energy (solar cells<sup>87</sup>, batteries<sup>88</sup>, fuel cells<sup>89</sup>)
- Optics (sensors<sup>90</sup>, antireflective films<sup>91</sup>, low-emissivity glass<sup>92</sup>)
- Microelectronics (coating films)<sup>93</sup>
- Machining industry (functional films, super hard coatings<sup>94</sup>, self-lubricating films<sup>95</sup>)
- Decoration (total reflective or translucent films)<sup>96</sup>
- Biomedical supports (cochlear implants, drug delivery<sup>97</sup>)

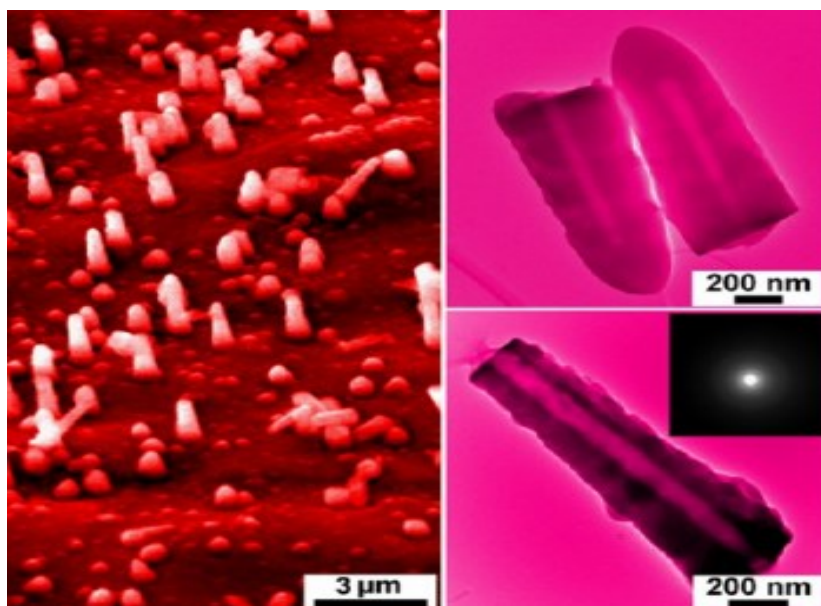


*Figure 2.3* SEM (Scanning Electron Microscope) images of submicrometer hollow bioactive glass cones deposited by RF magnetron sputtering for drug delivery applications.

Considering that one of our aims was the employment and optimization of a vapor-based technique to deposit metal halide perovskites thin films, we have seen in this technique the winning choice.

Starting from the following paragraph, several papers are reported. They have all been published during this Ph.D. period and are divided in relation with the hosting chapter:

- in “RF Magnetron Sputtering” every paragraph corresponds to a paper related to the application of this vapor-based technique in depositing perovskite thin films;
- “High Pressure Studies” contains a paper about the high-pressure in-situ study of lead-free perovskites carried out at the European Synchrotron Radiation Facility;
- “Physical Modulation Techniques” is separated into two paragraphs (each one with its related paper) dealing with the application of High Pressure Quenching and of Extended Ball Milling;

## 2.1 MAPbI<sub>3</sub>

### **Novel Physical Vapor Deposition Approach to Hybrid Perovskites: Growth of MAPbI<sub>3</sub> Thin Films by RF-Magnetron Sputtering**

#### *Purpose and scope*

Methylammonium lead iodide is the first hybrid metal halide perovskite used to build a solar device and it is still one of the most interesting and efficient materials for perovskite-based solar cells. Therefore, it is also the most known and studied hybrid metal halide perovskite.

We have been the first group in the world to employ RF magnetron sputtering to deposit this class of materials, demonstrating the possibility to use this advantageous technique to obtain thin films suitable to produce many different devices. This work gave us the preliminary results that kicked off the longer, more complete, and more varied one illustrated in this Ph.D. thesis.

#### *Introduction*

Simple fabrication routes represent a major advantage of hybrid organic-inorganic perovskites for the manufacturing of efficient yet low-cost solar cells. Solution-based methods are the most widespread approach to prepare perovskite thin films, being at the same time reliable and cost-effective<sup>1-5</sup>. However, even optimized solution-process methods are affected by shortcomings. One is a lack of control over the low-temperature crystallization process, which is affected by many factors such as solvents and precursors, surface properties of the substrate,

solvent evaporation during the deposition and annealing conditions, often leading to poor reproducibility of films morphology, thickness, crystallinity, and crystal size, properties that in turn have crucial influences on the photovoltaic performance. The second major shortcoming, more fundamental than the first one, is that sequential film deposition from solution cannot produce perovskite-perovskite heterostructures, since the solvent employed in depositing subsequent layers washes away the underlying ones. As a consequence, multijunction tandem solar cells and p-n junctions all perovskite based are advancing very slowly.

A very promising alternative to solution-based methods are the vapor-based deposition techniques, which started in the last few years to attract significant interest as a possible route to overcome the aforementioned problems<sup>6-9</sup>. In general, these methods are expected to provide purity of precursors and deposited films due to the vacuum environment and fine control of the deposition parameters, resulting in a high level of perovskite crystallization and reproducible films. Furthermore, vapor methods are suited for a scale-up preparation and large area deposition. It is crucial that vapor methods do not require the use of solvents and of annealing steps, allowing perovskite-on-perovskite deposition to create heterostructures and junctions.

To date, the vapor-based methods applied to the synthesis of hybrid perovskites are mainly based on vacuum evaporation process and vapor-assisted solution processes (VASP), with few other attempts of flash evaporation and ultrasonic spray coating<sup>7,8</sup>. We propose here a route based on a sputtering technique to provide highly reproducible single-phase hybrid perovskite films, full coverage of substrate surface, with the added bonus of being an industry-tested technique for large area film growth. The relatively lower deposition efficiency of



sputtering is overcome by a magnetron-based device. To date, no reports about the deposition of hybrid perovskites thin films by sputtering has been reported.

Motivated by the above reported issues related to the preparation of hybrid organic-inorganic perovskites films, in this paper we demonstrate the successful one-pot growth of methylammonium lead iodide  $\text{CH}_3\text{NH}_3\text{PbI}_3$  (MAPI) films by means of RF-magnetron sputtering starting from a single target made of a  $\text{CH}_3\text{NH}_3\text{I}$  (MAI) and  $\text{PbI}_2$  mixture with a 30% w/w excess of MAI. Sputtering technique allows to finely tune the deposition conditions by adjusting different parameters such as, for example, RF-power, gas pressure, and target to substrate distance thus providing an excellent platform to further optimize perovskite films as well as to extend the approach presented here for MAPI to any other material of interest in the field of Perovskite Solar Cells (PSCs).

### Experimental Methods

**Film deposition.** Thin films of MAPI have been deposited on amorphous silica substrates (MaTek, roughness ca. 1 nm) by means of radio frequency magnetron sputtering starting from a MAI/ $\text{PbI}_2$  mixture (Aldrich, > 99.9%) with a 30% w/w excess of MAI. The target (diameter 5.08 cm, thickness 1 cm) was made of pressed powders of MAI/ $\text{PbI}_2$  mixture. Depositions parameters were: i) target-to-substrate distance, 2 cm, ii) RF-power, 40 W, iii) argon pressure,  $2 \times 10^{-2}$  mbar. The depositions have been carried out in DC-bias mode by setting the value to 80 V (with respect to the target electrode), thus assuring a good control over the deposition rate. Film thickness has been determined through a mechanical profilometer. Estimated film growth is about 30 nm/min.

**XRD Diffraction.** The structural properties of the deposited thin films were characterized by X-ray diffraction (XRD) by means of a Bruker D8 Advance instrument (Cu radiation) in a Bragg-Brentano set-up.

**Optical Properties Measurement.** Reflectance (R) and transmittance (T) measurements were performed at 8° angle of incidence using a dual-beam spectrophotometer with an integrating sphere accessory (Agilent Cary 5000 UV-Vis-NIR). Absorbance (A) was calculated as  $1-R-T$ .

Time-resolved photoluminescence. Samples were mounted excited by a regenerative amplifier laser (Coherent Libra) delivering 100-fs-long pulses at a repetition rate of 1 KHz. Photoluminescence was dispersed with a grating spectrometer (Princeton Instruments Acton SpectraPro 2300i equipped with a 50 gr/mm grating blazed at 600 nm), dispersed and detected by a streak camera (Hamamatsu).

CW photoluminescence. Samples were excited by a diode-pumped Nd:YVO<sub>4</sub> CW laser at 532 nm (Spectra Physics Millennia). Photoluminescence was dispersed by a grating spectrometer (Princeton Instruments Acton SpectraPro 2300i) and detected by a LN-cooled CCD camera (Princeton Instruments PIXIS). At the highest excitation intensities, laser beam was chopped to reduce the overall thermal loading.

**AFM Measurements.** Surface topography and film roughness were measured by atomic force microscopy (AFM) with a NT-MDT Solver P47H-Pro instrument in semi contact mode at 1 Hz scan speed by a Etalon high-resolution non-contact silicon tip. Images were analyzed by WSxM software.

### Results and discussion

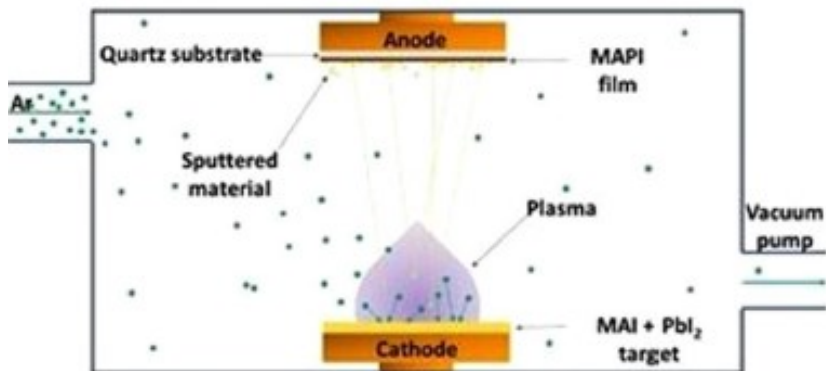


Figure 2.4 Schematic representation of the sputtering deposition method used in the present work to growth MAPI thin films

Figure 2.4 presents a sketch of the MAPI thin films growth method used in the present work, i.e. the RF-magnetron sputtering starting from a target made of MAI and  $\text{PbI}_2$  with a MAI excess of 30 wt%. Depositions were carried out at a RF-power of 40 W, with argon ( $P = 2 \times 10^{-2}$  mbar) as the sputtering gas in the DC-bias mode by setting its value to 80 V.

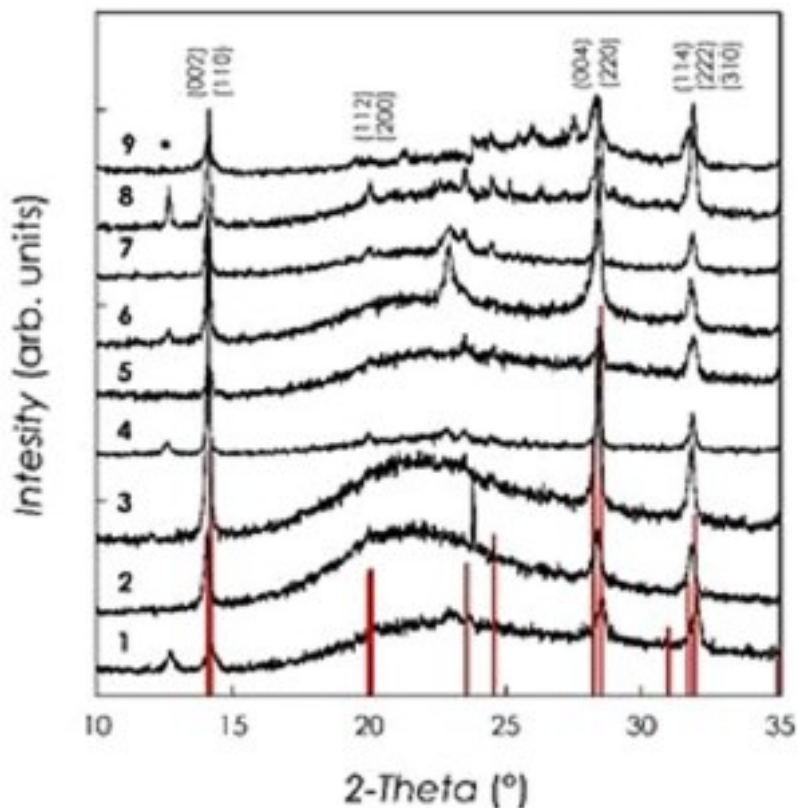


Figure 2.5 XRD patterns of MAPI films reported in Table 2.1

Figure 2.5 shows the X-ray diffraction patterns (XRD) of a series of representative MAPI films with variable thicknesses from below 200 nm (Film 1) up to about 3.2  $\mu\text{m}$  (Film 9) (details are reported in Table 2.1). Optimal growth conditions were obtained after extensive optimization work and are reported in the Experimental Section. The starting target for the sputtering deposition was a mixture of MAI and  $\text{PbI}_2$  with a 30% w/w excess of MAI.

*Table 2.1* Band Gaps ( $E_g$ ) for Select MHPs with variable chemistries and dimensionality

<b>Film</b>	<b>Thickness (nm)</b>	<b>Lifetime (ns)</b>
1	<200	1.2
2	220	1.9
3	300	1.7
4	350	4.3
5	440	13.2
6	510	2.7
7	640	5.6
8	940	1.8
9	3200	2.7

The films reported in Figure 2.5 have a crystal structure compatible with that of tetragonal MAPI (vertical red bars in Figure – main reflections indicated in the figure) and are single-phase or present very low  $\text{PbI}_2$  impurities (below 5% - the only peak of  $\text{PbI}_2$  observed is marked with an asterisk in the Figure). In addition, the diffraction peaks are quite narrow, indicating a good crystallization due to the sputtering process which is a significant result considering that the substrate is not heated during the deposition. The possibility of growing crystalline MAPI thin films on any substrate without in-situ and/or ex-situ thermal treatments, together with the use of a single target, are unique advantages of the present deposition process. In general, from Figure 2.5, it can be observed a slight preferential growth along the (00 l) directions, as suggested by the relative intensity of the experimental peaks corresponding to the (002) and (004) reflections compared to the calculated intensities. No significant shifts of the peaks as a function of film thickness are evident in the XRD patterns.

The surface morphology of the MAPI films has been investigated by Atomic Force Microscopy (AFM).

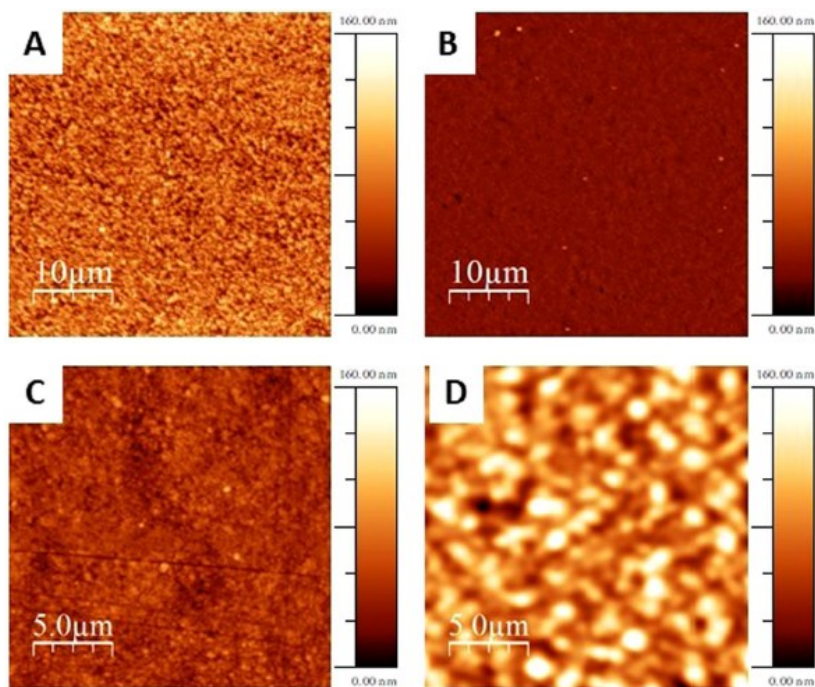
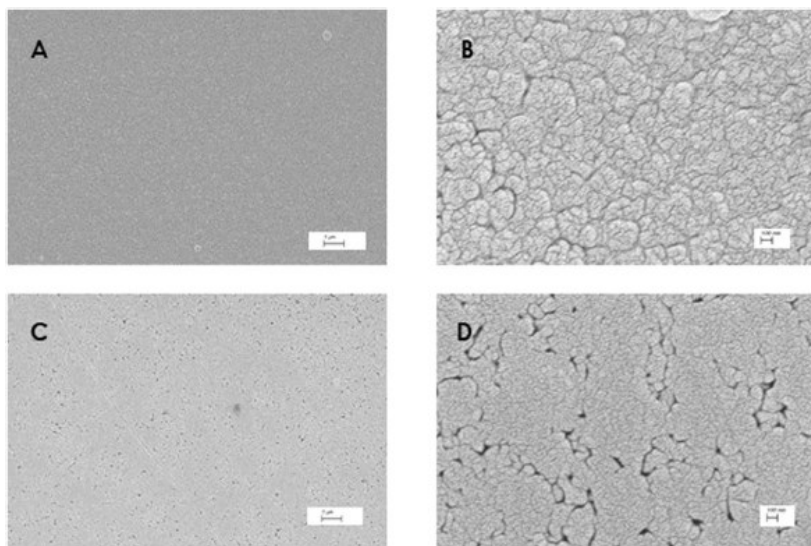


Figure 2.6 AFM topography images of MAPI film over  $40 \times 40 \mu\text{m}$  for film 1 (A), 4 (B), 7 (C) and 9 (D).

Figure 2.6 reports some selected images of films with variable thickness.

From the images of Figure 2.6, it is possible to see complete coverage of the substrate surface starting from film 4 (Figure 2.6-B) which has an estimated thickness of about 340 nm. The morphology of the deposited layers is made of small spherical grains with size in the 100–200 nm range which tends to increase by increasing the film thickness. In particular, Figure 2.6-D shows that, for a bulk-like film (thickness  $\sim 3200$  nm), the grain size is comparable to that of a polycrystalline powder. The average roughness estimated from the AFM maps, and defined as root mean square (RRMS) of surface height, is around 20 nm

for film 1 (thickness <200 nm), 7 nm for film 4 (thickness ~340 nm), 10 nm for film 7 (thickness ~640 nm) and 20 nm for film 9 (thickness ~3200 nm), values low enough to suggest a deposition mechanism based on layer growth on the fused silica substrate used here. Further insight into the morphology of the deposited film has been achieved by SEM microscopy.



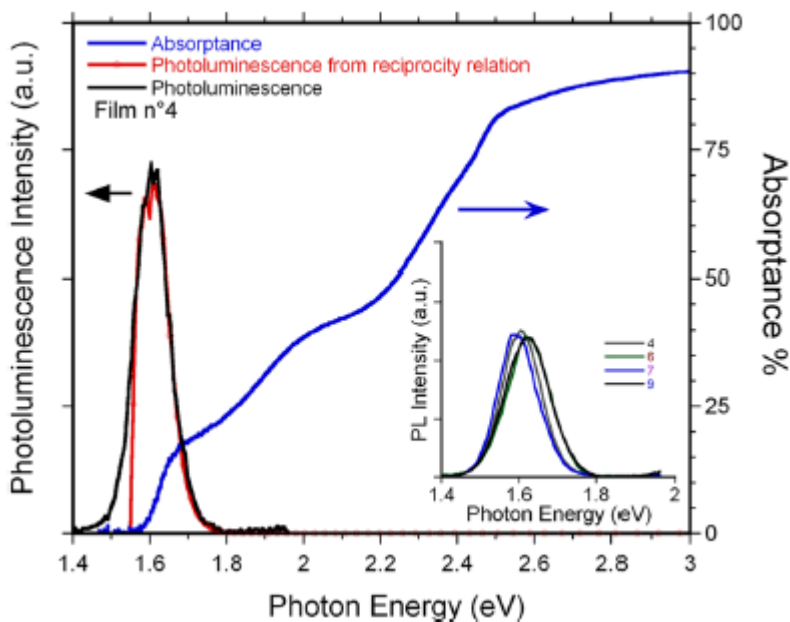
*Figure 2.7* SEM images of MAPI film 4 (A) magnification at 20 kX and (B) magnification at 100 kX) and film 7 (C) magnification at 20 kX and (D) magnification at 100 kX).

Figure 2.7 reports some representative images for film 4 (ca. 350 nm) and film 7 (ca. 640 nm) collected at two different magnifications (i.e., 20 kX and 100 kX).

SEM inspection reveals and confirms the very good coverage of the substrate obtained with the present technique. In addition, a more compact structure is observed in the images of the thicker sample, i.e. figures 2.6-C and 2.6-D, suggesting a coalescence of the film as the thickness increases. The morphology observed

in the present films has some similarities with the morphology reported for MAPI films deposited from different vapor methods (such as CVD and thermal evaporation)<sup>10,11</sup>. However, in the present case, a more compact layer is always observed with respect to the other techniques together with a better coverage of the substrate<sup>10,11</sup>.

Optical and excited-state properties of the deposited film have been assessed by absorptance (A) and photoluminescence (PL) measurements.



*Figure 2.8* Photoluminescence and absorptance spectra of MAPI films. Main panel. Blue line: absorptance (A) spectrum of the film No. 4. The black and red lines are the photoluminescence spectra. The former is the directly measured spontaneous emission spectrum. The second one is the emission spectrum calculated from the absorbance by using the reciprocity relation; the sharp drop of the calculated emission intensity at the low energy side of the spectrum stems from the experimental noise of the absorbance baseline. Inset. Directly measured photoluminescence spectra of various films.



Figure 2.8 shows a representative absorbance spectrum of a thin MAPI film (4) grown by sputtering. The spectrum of thicker samples clearly showed saturation phenomena for increasing photon energies above the band-gap, caused by the strong increase of the band-to-band absorption coefficient. As expected, a sharp absorption edge is found in the typical region of MAPI bandgap, i.e. around 1.6 eV<sup>12</sup>. No evidence of enhanced light absorption at 550 nm due to PbI<sub>2</sub> is present, confirming its absence or, when present, its relatively low amount according to the XRD analysis. The measured photoluminescence spectrum is also reported in Figure 2.8. The spontaneous emission is almost resonant with absorption, suggesting an intrinsic origin. Small variations of the emission peak energy from sample to sample, in the range of 10–20 meV, were observed (see inset of Figure 2.8); an analogous effect was indeed reported on solution-processed MAPI thin films, too<sup>13</sup>. The measured photoluminescence spectrum was compared with the expected spectrum according to the reciprocity relation between absorption and emission:  $PL(\hbar\omega) \propto A(\hbar\omega) \omega^2 e^{\frac{-\hbar\omega}{k_B T}}$ <sup>14</sup>. As the strong absorbance is due to direct band-to-band transitions, the photoluminescence spectrum derived in this way stems from spontaneous photon emission involving the very same intrinsic states. The excellent agreement between the expected and the measured spectra (red and black curves in Figure 2.8) further supports the absence of any extrinsic contribution to light emission in MAPI films grown by sputtering.

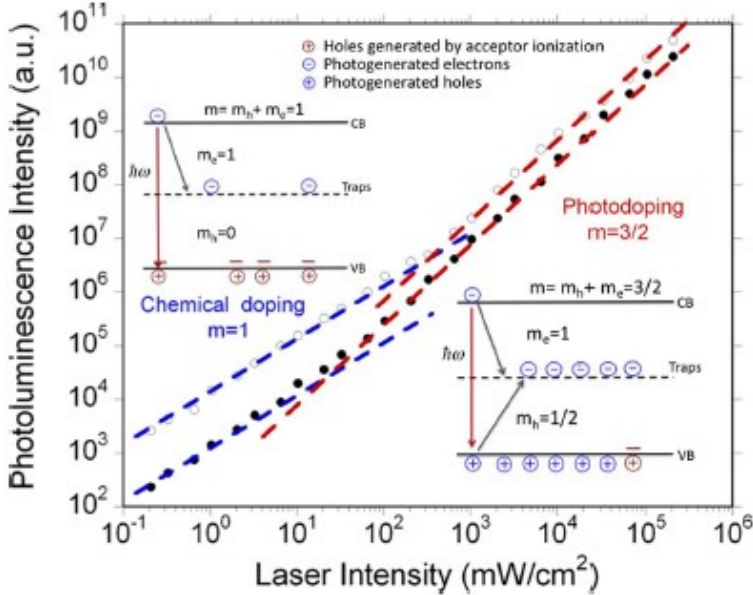


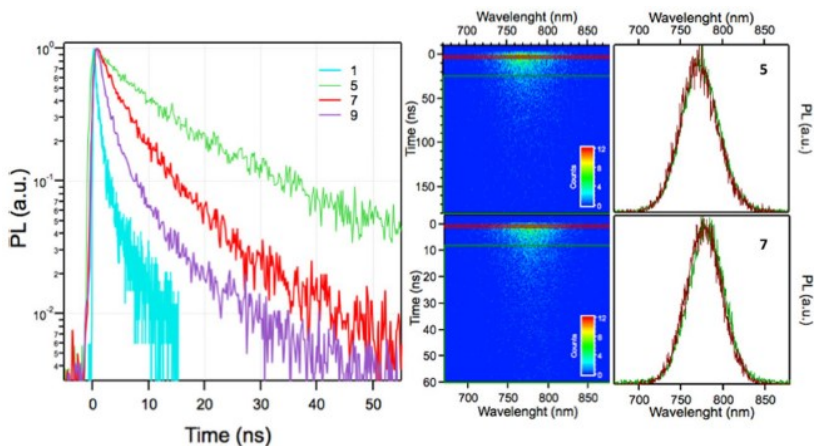
Figure 2.9 Photoluminescence dependence on excitation light intensity. Log-log plot of the photoluminescence intensity versus laser intensity. Full circles: film No. 4; Empty circles: film No. 12. The photoluminescence signal follows a power law as a function of the laser intensity. At low excitation density, the power index is  $m = 1$ ; at higher excitation densities,  $m = 3/2$ . Insets: recombination processes at low and high intensities. Electrons and holes mostly decay non-radiatively via mid-gap energy traps (dashed line), which are assumed to capture only one type of carrier. At low excitations, the majority of holes are generated by ionization of shallow acceptors (unintentional chemical doping). At high excitations, the majority of holes are generated by light. According to the Shockley-Read-Hall model, a high concentration of free holes in the valence band (VB) is created, which turns out as a sort of photodoping because most of electrons are trapped and the subsequent concentration of free electrons in the conduction band (CB) remains low.

Figure 2.9 reports the dependence of the photoluminescence intensity on the excitation power level of two films (4 and 12). The reported behavior is representative of the whole set of samples investigated in this work: in all films, the spontaneous emission scaled linearly ( $m = 1$ ) with the laser intensity at low excitation regimes, then grew superlinearly at higher pumping

intensities, following a  $m = 3/2$  power-law. In absence of nonradiative processes, light emission intensity is expected to linearly scale with the excitation level, independently of the nature of the involved electronic states, as all absorbed photons are subsequently reemitted. Nonradiative channels change this functional dependence. We have recently developed a simple approach to relate nonradiative processes with the dependence of the photoluminescence intensity on the excitation power<sup>15</sup>. In simple terms, if the concentration of electrons (holes) as a function of the laser intensity scales as a power law with index  $m_e$  ( $m_h$ ), the ensuing photoluminescence intensity also follows a power-law, but with index  $m = m_e + m_h$ . We found that the kinetics triggered by deep traps leads to  $m = m_e + m_h = 1 + 1/2 = 3/2$ , under the assumption (Shockley-Read-Hall model) that traps in their ground state can be filled by only one type of carrier (in the following we assume to be electrons)<sup>15</sup>. This result can be intuitively understood by looking at the recombination paths sketched in Figure 2.9. Electrons undergo a conventional first order decay process; their density is thereby linearly dependent on the laser intensity in steady-state ( $m_e = 1$ ). Holes recombine with trapped electrons, following a true bimolecular process; the square of the hole density is thus proportional to the laser intensity, which leads to  $m_h = 1/2$ . The hole lifetime is much longer than that of electrons, owing to the fact that the bimolecular recombination is a slow process at low carrier concentration. As a consequence, the densities of electrons and holes are unbalanced: the concentration of holes is much larger, and the semiconductor behaves as p-doped.  $m = 3/2$  is indeed the most common response observed in solution-processed MAPI films<sup>16–19</sup>.

In order to explain the linear behavior observed at low excitation regime, we first note that  $m = 1$  in our samples cannot be explained in terms of radiative recombinations. At low power

levels, the measured photoluminescence quantum yield was in fact around  $10^{-3}$ , proving that nonradiative recombinations are the most efficient decays. Figure 2.8 shows the proposed model to explain the experimental findings. We assume that films contain a low concentration of shallow acceptors (unintentional chemical p-doping). As long as the excitation rate is low, the hole concentration is independent of excitation ( $m_h = 0$ ), while the dynamics of electrons remains unaffected ( $m_e = 1$ ) and thus  $m = m_e$ . Increasing the excitation level, the concentration of photogenerated holes becomes dominant and the  $m = 3/2$  behavior is recovered. This analysis is consistent with the observation that laser intensity, at which the transition from chemical doping to photodoping occurs, depends on sample, ranging from  $10 \text{ mW/cm}^2$  (i.e., below the light intensity delivered by sun) to a few  $10^2 \text{ W/cm}^2$ . Unintentional doping (both p- and n-type) is often reported also in solution-processed MAPI films<sup>20,21</sup>.



*Figure 2.10* Time resolved photoluminescence. Left panel. Decay curves of the spectral-integrated photoluminescence signal for four films of different thicknesses. Central panels. Photoluminescence spectrograms of film 5 and 7, respectively. Right panels. Spectra of the spontaneous emission emitted in time window delimited by the red and green rectangles shown in the spectrograms reported in the central panels.

The time-resolved PL spectra of samples, representative of thin, intermediate and thick samples, are shown in Figure 2.10, together with the spectrograms of the two films with the longest lifetimes. The spectrograms of all films show no spectral shift of the emission with time (see the spectra recorded at two different delays in the left panel of Figure 2.10), as expected from intrinsic band-to-band emission following carrier thermalization at the band edges.

The photoluminescence lifetimes of all the films investigated in the present work are reported in Table 2.1 and provide a measure of trap concentration and non-radiative recombination rates associated to them. In general, the lifetimes are comparable to those of as-prepared solution-processed MAPI thin films<sup>22–26</sup>, but fall short with respect to state-of-the-art MAPI thin films optimized with post-growth treatments to passivate deep traps that have been demonstrated to enhance the photoluminescence lifetime and, consequently, quantum yield<sup>27–31</sup>. The results reported in this work refer to films which did not undergo any post-growth treatment and suggest that MAPI thin films produced by sputtering could be also substantially improved in their physico-chemical properties with future optimization work. By way of example, a possible morphology tuning and/or substrate heating to reduce the surface area of the film and/or to modulate the grain size, and therefore the surface defects, could already provide a significant increase in optical emission yield. Figure 2.10 shows that the longest carrier lifetimes have been obtained for intermediate thicknesses, which are close to the optimal values for PSCs absorbing layers. On other hand, for thinner and thicker films a reduction below 2 ns is observed. For thinner films this may be related to a major role played by surface defects, while for thicker film such reduction could be possibly related to an increase of the polycrystallinity which is known to enhance the nonradiative channels<sup>27–31</sup>.

## Conclusions

We reported the successful deposition of MAPI thin films by RF-magnetron sputtering. MAPI films were grown starting from a single-target made of MAI and  $\text{PbI}_2$  (with a 30% w/w excess of MAI) and appeared to be single-phase, with full surface coverage and thickness ranging from less than 200 nm to more than 3  $\mu\text{m}$ . The optical properties of the deposited films are comparable to as-grown solution-processed MAPI films and, in the future, the photoluminescence quantum yield could be substantially improved with post-growth passivation treatments. The development of vapor-phase deposition methods is of great interest in the current research on hybrid perovskites in view of a scale-up of device fabrication, the precise control of stoichiometry and the possibility of growing perovskite-perovskite heterostructures.

## References

1. Lee, M. M., Teuscher, J., Miyasaka, T., Murakami, T. N. & Snaith, H. Efficient Hybrid Solar Cells Based on Meso-Superstructured Organometal Halide Perovskites. *Science* 638, 643 (2012).
2. Jeon, N. J., Noh, J. H., Kim, Y. C., Yang, W. S. & Seok, S. II Solvent engineering for high-performance inorganic-organic hybrid perovskite solar cells. *Nat. Mater.* 13, 897 (2014).
3. Chen, Y., He, M., Peng, J. & Liang, Z. Structure and Growth Control of Organic-Inorganic Halide Perovskites for Optoelectronics: From Polycrystalline Films to Single Crystals. *Adv. Sci.* 3, 1500392 (2016).

4. Burschka, J. et al. Sequential deposition as a route to high-performance perovskite-sensitized solar cells. *Nature* 499, 316 (2013).
5. Xiao, M. et al. A fast deposition-crystallization procedure for highly efficient lead iodide perovskite thin-film solar cells. *Angew. Chem. Int. Ed.* 126, 10056 (2014).
6. Liu, M., Jhonston, M. B. & Snaith, H. J. Efficient planar heterojunction perovskite solar cells by vapour deposition. *Nature* 501, 395 (2013).
7. Ono, L. K., Leyden, M. R., Wang, S. & Qi, Y. Organometal halide perovskite thin films and solar cells by vapor deposition. *J. Mater. Chem. A* 4, 6693 (2016).
8. Shen, P.-S., Chang, Y.-H., Li, M.-H., Guo, T.-F. & Chen, P. Research Update: Hybrid organic-inorganic perovskite (HOIP) thin films and solar cells by vapor phase reaction APL. *Materials* 4, 091509 (2016).
9. Li, Z. et al. Scalable fabrication of perovskite solar cells. *Nature Rev. Mater.* 3, 18017 (2018).
10. Avila, J., Momblona, C., Boix, P. P., Sessolo, M. & Bolink, H. J. Vapor-Deposited Perovskites: The Route to High-Performance Solar Cell Production? *Joule* 1, 431 (2017).
11. Sessolo, M., Momblona, C., Gil-Escrig, L. & Bolink, H. J. Photovoltaic Devices Employing Vacuum-deposited Perovskite Layers. *MRS Bull.* 40, 660 (2015).
12. Saba, M. et al. Correlated electron-hole plasma in organometal perovskites. *Nature Comm.* 5, 5049 (2014).
13. D’Innocenzo, V., Kandada, A. R. S., De Bastiani, M., Gandini, M. & Petrozza, A. Tuning the Light Emission Properties by Band Gap Engineering in Hybrid Lead Halide Perovskite. *J. Am. Chem. Soc.* 136, 17730–17733 (2014).
14. Würfel, P., Würfel, U. *Physics of solar cells: from basic principles to advanced concepts*. Wiley-VCH Verlag GmbH & Co. KGaA: Weinheim, 2009.

15. Sarritzu, V. et al. Optical determination of Shockley-Read-Hall and interface recombination currents in hybrid perovskites. *Sci. Reports* 7, 44629 (2017).
16. Manser, J. S. & Kamat, P. V. Band filling with free charge carriers in organometal halide perovskites. *Nature Photon* 8, 737–743 (2014).
17. Colella, S., Mazzeo, M., Rizzo, A., Gigli, G. & Listorti, A. The Bright Side of Perovskites. *J Phys Chem Lett* 7, 4322–4334 (2016).
18. Cadelano, M. et al. Can Trihalide Lead Perovskites Support Continuous Wave Lasing? *Advanced Optical Materials* 3, 1557–1564 (2015).
19. Wehrenfennig, C., Eperon, G. E., Johnston, M. B., Snaith, H. J. & Herz, L. M. High charge carrier mobilities and lifetimes in organolead trihalide perovskites. *Adv. Mater.* 26, 1584–1589 (2014).
20. Shao, Y., Xiao, Z., Bi, C., Yuan, Y. & Huang, J. Origin and elimination of photocurrent hysteresis by fullerene passivation in  $\text{CH}_3\text{NH}_3\text{PbI}_3$  planar heterojunction solar cells. *Nat. Commun.* 5, 5784 (2014).
21. Xiao, Z. et al. Giant switchable photovoltaic effect in organometal trihalide perovskite devices. *Nat. Commun.* 14, 193 (2015).
22. Stoumpos, C. C., Malliakas, C. D. & Kanatzidis, M. G. Semiconducting Tin and Lead Iodide Perovskites with Organic Cations: Phase Transitions, High Mobilities, and Near-Infrared Photoluminescent Properties. *Inorg. Chem.* 52, 9019–9038 (2013).
23. Stranks, S. D. et al. Electron-Hole Diffusion Lengths Exceeding 1 Micrometer in an Organometal Trihalide Perovskite Absorber. *Science* 342, 341–344 (2013).



24. Xing, G. et al. Long-range balanced electron- and hole-transport lengths in organic-inorganic  $\text{CH}_3\text{NH}_3\text{PbI}_3$ . *Science* 342, 344–347 (2013).
25. Edri, E. et al. Why Lead Methylammonium Tri-Iodide Perovskite-Based Solar Cells Require a Mesoporous Electron Transporting Scaffold (but Not Necessarily a Hole Conductor). *Nano Lett.* 14, 1000–1004 (2014).
26. Brenes, R. et al. Metal Halide Perovskite Polycrystalline Films Exhibiting Properties of Single Crystals. *Joule* 1, 155–167 (2017).
27. Yang, B. et al. Controllable Growth of Perovskite Films by Room-Temperature Air Exposure for Efficient Planar Heterojunction Photovoltaic Cells. *Angew. Chem. Int. Ed.* 54, 14862–14865 (2015).
28. Tachikawa, T., Karimata, I. & Kobori, Y. Surface Charge Trapping in Organolead Halide Perovskites Explored by Single-Particle Photoluminescence Imaging. *J. Phys. Chem. Lett.* 6, 3195–3201 (2015).
29. Kong, W., Ding, T., Bi, G. & Wu, H. Optical characterizations of the surface states in hybrid lead–halide perovskites. *Phys. Chem. Chem. Phys.* 18, 12626–12632 (2016).
30. Peng, W. et al. Influence of growth temperature on bulk and surface defects in hybrid lead halide perovskite films. *Nanoscale* 8, 1627–1634 (2016).
31. De Quilettes, D. W. et al. Solar cells. Impact of microstructure on local carrier lifetime in perovskite solar cells. *Science* 348, 683–686 (2015).

## 2.2 CsSnBr<sub>3</sub>, CsSn<sub>2</sub>Br<sub>5</sub> and Cs<sub>2</sub>SnBr<sub>6</sub>

### **Versatile vapor phase deposition approach to cesium tin bromide materials CsSnBr<sub>3</sub>, CsSn<sub>2</sub>Br<sub>5</sub> and Cs<sub>2</sub>SnBr<sub>6</sub>**

#### *Purpose and scope*

In this work, we reported on the successful application of RF-magnetron sputtering to deposit, by using a single type of target, three different materials in the form of thin films within the Cs–Sn–Br compositional range

All that highlighted the wide tunability of the technique, the possibility of using it to stabilize metastable phases, and its successful application in the deposition of lead-free and all-inorganic phases.

#### *Introduction*

In recent times, there has been a growing interest towards all-inorganic perovskite materials for their application in perovskite solar cells (PSCs) and optoelectronics. Among others, it is possible to mention the use of CsPbBr<sub>3</sub> and CsPbI<sub>3</sub>, and their solid solutions, in the fabrication of PCSs, as well as their possible use in optical devices due to the superior emission properties when dealing with nanosized materials.<sup>1–5</sup> Besides the well-established Pb-based all inorganic 3D perovskites, there is an intense and continuous interest in developing lead-free phases together with the search of more stable compositions by reducing the dimensionality of 3D materials, thus exploring 2D, 1D, 0D, and perovskite related phases.<sup>6–10</sup> 3D lead-free all-inorganic materials are now currently employed in the fabrication of photovoltaic devices, as can be seen by the recent

use of CsSnI<sub>3</sub> or Bi-based double perovskites.<sup>11</sup> On the other hand, the exploration of lower-dimensional lead-free perovskite and perovskite-related phases is still a challenge. One of the main reasons can be found in the difficulty in achieving thin films of all-inorganic materials, where the common wet-chemistry protocols used for hybrid organic–inorganic (HOIP) phases do not reliably assure good results. For example, CsBr has a poor solubility in some apolar solvents such as dimethyl formamide, DMF, dimethyl sulfoxide, DMSO, etc. thus limiting the use of one-step depositions methods.<sup>12</sup> Even with modified one-step depositions, the methods do not provide uniform films and in other cases annealing at elevated temperatures is required, which is impractical and leads to a reduction of the overall device performance.<sup>13</sup> Two-step deposition methods provide better results in terms of uniformity but are more time-consuming and require the control of several parameters.<sup>12</sup>

One possible method to overcome such limitation is the use of vapor phase deposition methods, but also in this case the current methods of target evaporation by heating (commonly used for HOIPs) cannot be easily used for inorganic materials showing low volatility. In many cases, after vacuum deposition methods, a thermal annealing at temperature up to 320 °C is required.<sup>14</sup> In addition to this, when dealing with tin-based systems, one of the most exploited choice to substitute for lead, the stabilization of Sn<sup>2+</sup> oxidation state during usual solution-based synthetic procedures can be a challenge, thus requiring the use of additives or complex synthetic approaches.<sup>7</sup>

In this paper, we are going to focus on a series of phases, within the Cs–Sn–Br compositional phase diagram, by showing a vapor phase deposition approach based on RF-magnetron sputtering which allows, by tuning the deposition parameters or the post-synthetic treatments, to access at least three single-phase compounds, namely: CsSnBr<sub>3</sub>, CsSn<sub>2</sub>Br<sub>5</sub> and Cs<sub>2</sub>SnBr<sub>6</sub>, by using

the same starting target material. RF-magnetron sputtering has been already shown, by our group, to be a suitable technique for metal halide perovskites because of its benefits in terms of reliability, simplicity, and scalability, among others. In addition, in most of the cases, a fully crystalline and uniform film is obtained without the requirement of any thermal annealing. Quite surprisingly, however, this method has not yet been fully explored in the photovoltaic field.<sup>15</sup>

### Experimental methods

**Film deposition.** All the thin films have been deposited on amorphous silica substrates (MaTek, roughness ca. 1 nm) by means of radiofrequency (RF) magnetron sputtering starting from a CsBr/SnBr<sub>2</sub> mixture (Aldrich, > 99.9%). The target (diameter 5.08 cm, thickness 1 cm) was made of pressed powders of CsBr/SnBr<sub>2</sub> mixture. Depositions parameters were: (i) target-to-substrate distance, 8 cm, (ii) RF-power, 50 W and 70 W (iii) argon pressure,  $2 \cdot 10^{-2}$  mbar (iv) argon flux 20 SCCM (v) substrate temperature, 0 °C, 200 °C. The depositions have been carried out in power-control mode. Film thickness has been determined by means of a P-6 stylus profilometer KLA Tencor.

**Post-deposition heating.** After the deposition selected films have been heated and cooled in vacuum by using a BÜCHI glass drying oven. Others were instead heated and cooled in air by means of an oven.

**XRD diffraction.** The structural properties of the deposited thin films were characterized by X-ray diffraction (XRD) by means of a Bruker D8 Advance instrument (Cu radiation) in a Bragg-Brentano setup. EDX analysis provided an agreement within 5%

between nominal and experimental compositions. Microstructural characterization of the samples was made using a high-resolution scanning electron microscope (SEM, TESCAN Mira 3) operated at 25 kV.

**Optical properties measurement.** Absorptance (A) spectra were collected by using a UV-vis spectrophotometer Jasco750 with an integration sphere.

**AFM.** Atomic Force Microscopy (AFM) images (256 x 256 pixels) were obtained with an AutoProbe CP microscope (ThermoMicroscopes-VEECO), operating in contact mode (CAFM), by means of sharpened silicon tips onto V-shaped cantilevers (resonance frequency: 15 kHz; force constant: 0.03 N m<sup>-1</sup>). For each analyzed film, scans of 10 mm x 10 mm and 4.0 mm x 4.0 mm have been carried out with a scan rate ranging from 1.0 to 1.5 Hz. A standard second-order flatten processing of the images has been performed to correct the scanner nonlinearity.

### Results and discussion

CsSnBr<sub>3</sub> is a typical 3D perovskite with a cubic unit cell and a band-gap around 1.72 eV, and was object of few studies addressing the growth of films by using spin-coating and reactive thermal deposition to achieve epitaxial materials.<sup>16–18</sup>

CsSn<sub>2</sub>Br<sub>5</sub> has never been reported in the form of film (except as an impurity phase in ref. 17), and the few data available refer to crystal structure investigation in single crystals.<sup>19</sup> CsSn<sub>2</sub>Br<sub>5</sub> has a 2D tetragonal crystal structure belonging to the I4/mcm space group, and is composed by two adjacent Sn<sub>2</sub>Br<sub>5</sub> layers separated by a Cs layer along the c-axis. Significant work has been carried

out on the Pb-based counterpart, namely  $\text{CsPb}_2\text{Br}_5$ , which is considered a promising candidate for optoelectronic applications.<sup>20–22</sup> Finally,  $\text{Cs}_2\text{SnBr}_6$  is a Sn(IV) containing phase of great actual interest for both solar cells and optoelectronic applications, and is a vacancy ordered double perovskite with cubic symmetry (space group  $\text{Fm}\bar{3}\text{m}$ ), and a reported band-gap around 3.2 eV.<sup>23–25</sup> For this phase no reports on thin film preparation have been reported. A sketch of the crystal structures of the three compounds is reported in Figure 2.11.

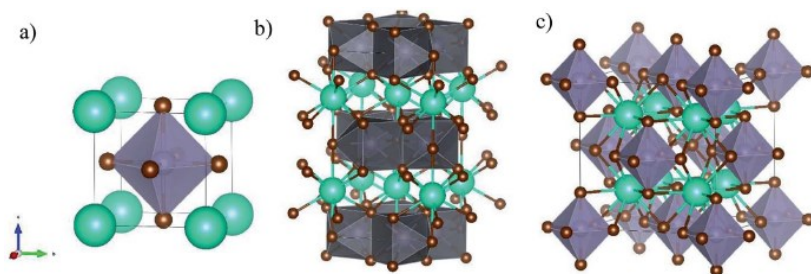


*Figure 2.11* Sketch of the crystal structures of (a)  $\text{CsSnBr}_3$ , (b)  $\text{CsSn}_2\text{Br}_5$ , and (c)  $\text{Cs}_2\text{SnBr}_6$  showing the peculiar octahedra arrangement in the different structures (see main text for details).

The samples have been prepared in form of film on fused silica substrates by RF-magnetron sputtering starting from a target made of  $\text{CsBr}$  and  $\text{SnBr}_2$ . In this paper, we are reporting representative data for the three single-phase compounds obtained, which are the results of several replica of film depositions. As mentioned above, the three compositions have been prepared using a single target by varying the sputtering conditions as shown in Table 2.2.

Table 2.2 Sputtering conditions used in the experiment. Average thickness of all films was in the range of 800–1000 nm

Phase	Pressure (mbar)	Argon gas flux (sccm)	Power (W)	DC-bias (V)	Deposition time (min)	Thermal treatment
CsSnBr <sub>3</sub>	0.02	1.2	20	50	10	200°C during deposition
CsSn <sub>2</sub> Br <sub>5</sub>	0.02	1.9	20	70	10	-
Cs <sub>2</sub> SnBr <sub>6</sub>	0.02	1.7	20	70	10	200°C during deposition

Essentially, the film growth conditions were quite similar for the three phases, with tuning of sputtering power and thermal treatments as key parameters to modulate the phase composition. By heating the substrate during film depositions to 200 °C, CsSnBr<sub>3</sub> was prepared, while a post-deposition annealing to 200 °C allowed forming Cs<sub>2</sub>SnBr<sub>6</sub>. Without in situ or postdeposition heating, CsSn<sub>2</sub>Br<sub>5</sub> is the stable phase formed under selected conditions.

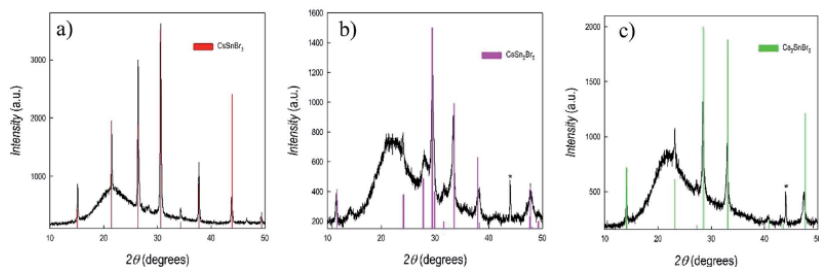


Figure 2.12 X-ray diffraction patterns of (a) CsSnBr<sub>3</sub>, (b) CsSn<sub>2</sub>Br<sub>5</sub>, and (c) Cs<sub>2</sub>SnBr<sub>6</sub>. Vertical red bars refer to the calculated pattern for each phase. Asterisk indicates reflection from the sample holder.

Figure 2.12 shows the X-ray diffraction patterns of three films of about 1 mm thickness representing  $\text{CsSnBr}_3$ ,  $\text{CsSn}_2\text{Br}_5$  and  $\text{Cs}_2\text{SnBr}_6$ , together with the reference patterns for each of them (as vertical bars).

As can be seen from Figure 2.12, the three films are single-phase with very good crystallinity, also for the sample prepared without any thermal treatment (i.e.  $\text{CsSn}_2\text{Br}_5$ ). No signs of peculiar preferential orientation effects are found in the patterns. Hump around  $22^\circ$  in Figure 2.12 is due to the amorphous nature of the substrate (fused silica). Chemical composition of the prepared films was checked by EDX (energy dispersive X-ray analysis) and was found in very good agreement with nominal stoichiometries. The results reported above clearly indicate the versatility of sputtering approach in modulating the deposited phases by simply changing the deposition and/or heat treatment parameters. Being the sputtering a quite complex process, often far from equilibrium, it is not simple, and goes beyond the scope of the present work, to understand the specific conditions leading to the stability of the different phases, probably related to the different sputtering efficiencies of  $\text{CsBr}$  and  $\text{SnBr}_2$  and to surface reactions. Notwithstanding, the method is extremely reliable and, by keeping the same sputtering conditions/thermal treatments, the three phases are always obtained. The lattice parameters determined from the refinement of the patterns reported in Figure 2.12 are:  $a = 5.8196(7) \text{ \AA}$  for cubic  $\text{CsSnBr}_3$ ;  $a = 8.4958(6) \text{ \AA}$  and  $c = 15.180(1) \text{ \AA}$  for tetragonal  $\text{CsSn}_2\text{Br}_5$ ; and  $a = 10.8417(8) \text{ \AA}$  for cubic  $\text{Cs}_2\text{SnBr}_6$ .

On the representative films shown in Figure 2.12, we performed UV-vis absorption spectroscopy measurements, which are shown in Figure 2.13, below.



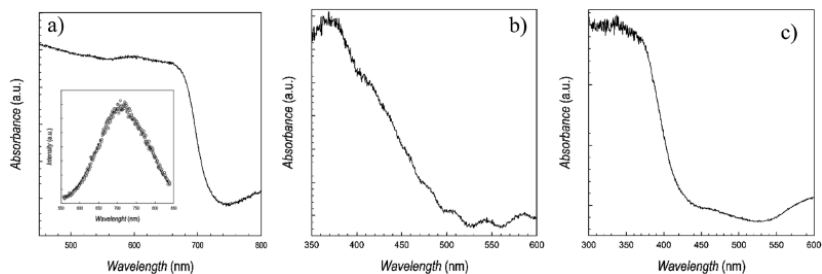


Figure 2.13 UV-vis absorption spectra of (a) CsSnBr<sub>3</sub>, (b) CsSn<sub>2</sub>Br<sub>5</sub>, and (c) Cs<sub>2</sub>SnBr<sub>6</sub>. Inset of panel (a) reports the photoluminescence spectrum of CsSnBr<sub>3</sub>.

The spectra of CsSnBr<sub>3</sub> well matches with the data reported for the bulk phase, as well as for the few thin films available, with a very sharp absorbance around 700 nm, and a band-gap of  $\sim 1.73$  eV.<sup>16–18,26</sup> For this material, having an absorption in a range of interest for photovoltaic applications, also the photoluminescence (PL) spectra has been determined, and it is shown in the inset of Figure 2.13-a, indicating a maximum of emission around 710 nm. This result is also in agreement with previous data.<sup>26</sup> The quality of the absorption spectra of CsSnBr<sub>3</sub> film, prepared by sputtering, is significantly higher with respect to the data reported for films prepared by wet-chemistry route, showing edges extending from 400 to 700 nm.<sup>11</sup> The spectra of CsSn<sub>2</sub>Br<sub>5</sub> shows broader features, possibly related to the lack of any thermal treatment, with a first edge around 390 nm and a band-gap of about 3.2 eV, in fair agreement with the only available report on this phase, which is however for a very thin film used as a barrier layer.<sup>17</sup> Finally, Figure 2.13-c reports the absorption spectra of Cs<sub>2</sub>SnBr<sub>6</sub> showing again a very sharp edge and an estimated band-gap of about 2.85 eV, in good agreement with previous reports on bulk materials, being this the first time Cs<sub>2</sub>SnBr<sub>6</sub> is prepared in form of film.<sup>23,24</sup>

Finally, the morphology of the three films reported above has been determined by Atomic Force Microscopy (AFM) and some

representative images (4 mm x 4 mm area) are shown below (Figure 2.14).

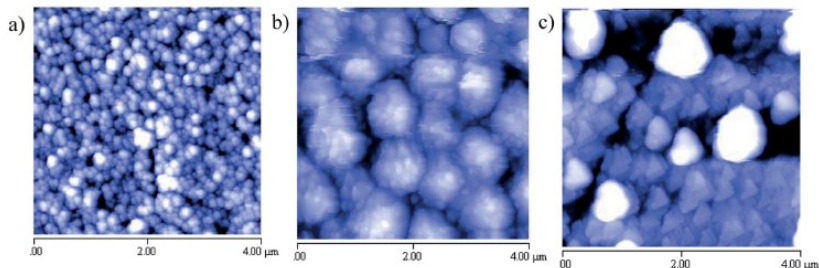


Figure 2.14 Selected AFM images of (a)  $\text{CsSnBr}_3$ , (b)  $\text{CsSn}_2\text{Br}_5$ , and (c)  $\text{Cs}_2\text{SnBr}_6$  on 4 mm x 4 mm area.

There is a markedly different morphology in the three films deposited.  $\text{CsSnBr}_3$  (a) shows well-defined spherical grains of average dimension around 100–150 nm and a surface roughness ( $R_{\text{rms}}$ ) around 30 nm;  $\text{CsSn}_2\text{Br}_5$  (b) is composed of grains of about 150 nm agglomerated into relatively big spherical objects (500–700 nm) which can be the result of the absence of any thermal treatment; and finally  $\text{Cs}_2\text{SnBr}_6$  films (c) is characterized by polygonal-shaped grains of a size around 200 nm. The peculiar shape of these last grains are in some way reminiscent of the hexagonal form found in nanosized samples of  $\text{Cs}_2\text{SnBr}_6$  particles.<sup>24</sup> Substrate coverage as well resulted to be quite good for these sputtered films as can be inferred by 10 mm x 10 mm images.

Unfortunately, there are not direct AFM images collected on analogous film to perform any relevant comparison. It is interesting to note, however, that any specific composition leads to a peculiar morphology (for analogous film thicknesses) (Figure 2.14).

## Conclusions

This paper reports the successful deposition of three distinct single-phase materials in form of thin films of the Cs–Sn–Br system by RF-magnetron sputtering, namely CsSnBr<sub>3</sub>, CsSn<sub>2</sub>Br<sub>5</sub> and Cs<sub>2</sub>SnBr<sub>6</sub>. The deposition approach used in this work allowed using the same starting target material and tuning the preparation of the desired phase by changing the sputtering parameters or applying mild post-deposition heat treatments.

Structural, optical and morphology measurements confirm the quality of the prepared films. The accessibility of complex all-inorganic phases, which may be difficult to deposit in form of films by means of traditional wet-chemistry routes, is demonstrated through a simple, reliable and scalable vapor-phase method such as sputtering.

## References

1. H. Yuan, Y. Zhao, J. Duan, Y. Wang, X. Yang and Q. Tang, *J. Mater. Chem. A*, 2018, 6, 24324–24329.
2. X. Li, Y. Tan, H. Lai, S. Li, Y. Chen, S. Li, P. Xu and J. Yang, *ACS Appl. Mater. Interfaces*, 2019, 11, 29746–29752.
3. C. F. J. Lau, Z. Wang, N. Sakai, J. Zheng, C. H. Liao, M. Green, S. Huang, H. J. Snaith and A. Ho-Baillie, *Adv. Energy Mater.*, 2019, 9, 1901685.
4. K. Chen, W. Jin, Y. Zhang, T. Yang, P. Reiss, Q. Zhong, U. Bach, Q. Li, Y. Wang, H. Zhang, Q. Bao and Y. Liu, *J. Am. Chem. Soc.*, 2020, 142, 3775–3783.
5. J. Shamsi, A. S. Urban, M. Imran, L. De Trizio and L. Manna, *Chem. Rev.*, 2019, 119, 3296–3348.
6. T.-B. Song, T. Yokoyama, S. Aramaki and A. G. Kanatzidis, *ACS Energy Lett.*, 2017, 2, 897–903.

7. S. Gupta, T. Bendikov, G. Hodes and D. Cahen, *ACS Energy Lett.*, 2016, 1, 1028–1033.
8. I. Chung, J. Song, J. Im, J. Androulakis, C. Malliakas, H. Li, A. Freeman, J. Kenney and M. Kanatzidis, *J. Am. Chem. Soc.*, 2012, 134, 8579–8587.
9. L. Mao, C. C. Stoumpos and M. G. Kanatzidis, *J. Am. Chem. Soc.*, 2018, 141, 1171–1190.
10. H. Lin, C. Zhou, Y. Tian, T. Siegrist and B. Ma, *ACS Energy Lett.*, 2018, 3, 54–62.
11. S. M. Jain, T. Edvinsson and J. R. Durrant, *Commun. Chem.*, 2019, 2, 91.
12. M. B. Faheem, B. Khan, C. Feng, M. U. Farooq, F. Raziq, Y. Xiao and Y. Li, *ACS Energy Lett.*, 2020, 5, 290–320.
13. J. K. Nam, S. M. Jung, S. U. Chai, Y. J. Choi, D. Kim and J. H. Park, *J. Phys. Chem. Lett.*, 2017, 8, 2936–2940.
14. L. A. Frolova, D. V. Anokhin, A. A. Piriyazev, S. Y. Luchkin, N. N. Dremova, K. J. Stevenson, J. Keith and P. A. Troshin, *J. Phys. Chem. Lett.*, 2017, 8, 67–72.
15. S. Bonomi, D. Marongiu, N. Sestu, M. Saba, M. Patrini, G. Bongiovanni and L. Malavasi, *Sci. Rep.*, 2018, 8, 15388.
16. F. A. Akublatov, S. A. Tsarev, M. Elshobaki, S. Y. Luchkin, I. S. Zhidkov, E. Z. Kurmanev, S. M. Aldoshin, K. J. Stevenson and P. A. Troshin, *J. Phys. Chem. C*, 2019, 123, 26862–26869.
17. L. Wang, P. Chen, N. Thongprong, M. Young, P. S. Kuttipillai, C. Jiang, P. Zhang, K. Sun, P. M. Duxbury and R. R. Lunt, *Adv. Mater. Interfaces*, 2017, 4, 1701003.
18. C. Hartmann, S. Gupta, T. Bendikov, X. Kozina, T. Kunze, R. Felix, G. Hodes, R. G. Wilks, D. Cahen and M. Baer, *ACS Appl. Mater. Interfaces*, 2020, 12, 12353–12361.
19. I. Abrahams, D. Z. Demetriou, R. T. Kroemer, H. Taylor and M. Motevalli, *J. Solid State Chem.*, 2001, 160, 382–387.
20. Z. Zhang, Y. Zhu, W. Wang, W. Zheng, R. Lin and F. Huang, *J. Mater. Chem. C*, 2018, 6, 446–451.

21. Y.-Q. Zhou, L. Jian and B.-X. Liu, *J. Phys. Chem. Lett.*, 2019, 10, 6118–6123.
22. M. Li, X. Zhang, W. Tao, P. Wang, K. Matras-Postolek and P. Yang, *J. Phys. Chem. C*, 2018, 122, 28968–28976.
23. M. M. S. Karim, A. M. Ganose, L. Pieters, W. W. Winnie Leung, J. Wade, L. Zhang, D. O. Scanlon and R. G. Palgrave, *Chem. Mater.*, 2019, 22, 9430–9444.
24. A. Veronese, M. Patrini, D. Bajoni, C. Ciarrocchi, P. Quadrelli and L. Malavasi, *Front. Chem.*, 2020, 8, 35.
25. A. D. Jodlowski, D. Rodriguez-Padron, R. Luque and G. de Miguel, *Adv. Energy Mater.*, 2018, 8, 1703120.
26. A. Bernasconi, A. Rizzo, A. Listorti, A. Mahata, E. Mosconi, F. De Angelis and L. Malavasi, *Chem. Mater.*, 2019, 31, 3527–3533.

## 2.3 $\text{Cs}_3\text{Bi}_2(\text{I}_{1-x}\text{Br}_x)_9$

### **Optical and Structural Properties Tuning in Physical Vapor Deposited Bismuth Halides $\text{Cs}_3\text{Bi}_2(\text{I}_{1-x}\text{Br}_x)_9$ ( $0 \leq x \leq 1$ )**

#### *Purpose and scope*

Here, crystalline films of lead-free all-inorganic  $\text{Cs}_3\text{Bi}_2\text{X}_9$  ( $\text{X}=\text{Br}, \text{I}$ ) perovskites have been deposited by RF-magnetron sputtering providing high-quality single-phase films as confirmed by structural, morphological, and optical properties characterization.

The work not only confirmed the versatility of the technique and its successful application in growing lead-free thin films suitable to produce devices but also demonstrated that it is possible to use this method to deposit solid solutions and subsequently chemically tune the structural and optoelectronic properties of metal halide perovskites.

Finally, preliminary photocatalytic activity tests on the degradation of methylene blue provided solid data indicating the future possible exploitation of Bi-based perovskite derivative materials as active photocatalysts.

#### *Introduction*

Bismuth-based perovskite derivatives of general formula  $\text{Cs}_3\text{Bi}_2\text{X}_9$  ( $\text{X}=\text{Br}, \text{I}$ ) are attracting a huge interest in several diverse communities for their technological potential spanning from photocatalysis to photodetectors, organic synthesis and photovoltaics.<sup>1-11</sup>

Triggered by the issue to overcome the concerns related to Pb-toxicity in Metal Halide Perovskite (MHPs) for photovoltaics,

the field of lead-free perovskite and perovskite derivatives has significantly extended towards novel applications by exploiting the photoactivity of lead-free materials which possess, in addition to relevant catalytic performance, water-stability which is still a key problem of lead-based systems. Among Bi-containing perovskites,  $\text{Cs}_3\text{Bi}_2\text{Br}_9$  and  $\text{Cs}_3\text{Bi}_2\text{I}_9$  have been object of several recent publications highlighting, in particular, their potential use in organic synthesis and photodetection.<sup>5,6,8,11</sup>  $\text{Cs}_3\text{Bi}_2\text{Br}_9$  has a trigonal crystal structure (Space Group. S.G.,  $P-3m$ ) characterized by a layered structure of alternated corner-sharing octahedra, and shows strong optical absorbance around 400-500 nm depending on the material state, *i.e.* powder, single-crystals, thin films.<sup>12-16</sup> Its large excitonic binding energy prevents this material being suitable for photovoltaics, nevertheless it has offered good performance as active layer in photodetectors and, even more interestingly, in photocatalytic applications.<sup>6,11,12</sup>  $\text{Cs}_3\text{Bi}_2\text{Br}_9$  showed to be effective in the direct selective photocatalyzed oxidation of hydrocarbons with high conversion rates and excellent selectivity and in the ring-opening reaction of epoxides.<sup>11</sup> In both cases,  $\text{Cs}_3\text{Bi}_2\text{Br}_9$  exhibited good stability and recyclability while the lead-based counterpart performed significantly worse.  $\text{Cs}_3\text{Bi}_2\text{I}_9$  perovskite, crystallizing in a hexagonal symmetry (S.G.,  $P6_3/mmc$ ), on the other hand, has been deeply investigated for its possible use as active layer in Perovskite Solar Cells (PSCs) since 2015, due to its high absorption coefficient and a band-gap of about 2.10 eV.<sup>1</sup> Strong efforts have been put in place in optimizing the film morphology for PSCs due to the known dissolution problems of inorganic precursors when applying solution-based methods.<sup>1</sup> The potential applications of  $\text{Cs}_3\text{Bi}_2\text{I}_9$  have been further extended in the last years to photodetection and photocatalysis, in analogy with the bromide-containing phase.<sup>5,6,9</sup> As an example, perovskite single crystal thin films of  $\text{Cs}_3\text{Bi}_2\text{I}_9$  have

been grown by a space-limited solvent evaporation crystallization method providing highly efficient photodetectors with impressive stability without any encapsulation for 1000 h in humid air (50% RH).<sup>17</sup> The same compound has been used in photocatalysis for hydrogen evolution and organic pollutant degradation.<sup>18,19</sup>

Mixed  $\text{Cs}_3\text{Bi}_2\text{I}_{9-x}\text{Br}_x$  have been also the object of some investigation for both photovoltaics and photodetection applications.<sup>2,5</sup> An extensive and deep study of the I/Br solid solution is reported in the work of Yu et al., where thin films of both end members and intermediate mixed compositions have been prepared by spin coating and used in PSCs.<sup>2</sup> While showing relatively low power conversion efficiencies (PCEs), with  $\text{Cs}_3\text{Bi}_2\text{I}_6\text{Br}_3$  delivering 1.15% as best performing compound, the data confirm the significant stability of Bi-based phases.<sup>2</sup> Liu *et al.*, studied the performances of  $\text{Cs}_3\text{Bi}_2\text{Br}_{9-x}\text{I}_x$  films by varying  $x$ , and achieved the best performance for the  $\text{Cs}_3\text{Bi}_2\text{I}_6\text{Br}_3$  composition with an excellent photosensitivity of  $4.1 \times 10^4$  at zero bias as well as with the responsivity and detectivity reaching 15 mA/W and  $4.6 \times 10^{11}$  Jones.<sup>5</sup> Also in this case, an excellent stability in the ambient environment, maintaining over 96% of the initial value after 100 days, was observed.<sup>5</sup>

All the evidences reported so far refer to works carried out in the last couple of years suggesting that Bi-based layered perovskites show promise for future exploration and possible applications in several technologically relevant fields, as also recently demonstrated by the interest in tunable  $\text{Cs}_3\text{Bi}_2(\text{Cl}_{1-x}\text{I}_x)_9$  halide perovskites.<sup>20</sup> In this respect, the possibility of film deposition scale-up is an urgent issue. Recently, physical vapor deposition methods are triggering significant interest; they seem a valuable path to make the required step from the laboratory scale to the industrial scale in all the fields where good quality thin films are required, in particular when considering all-inorganic perovskite



materials where solution processing is more complicated with respect to hybrid organic-inorganic phases.<sup>21</sup>

Based on the above considerations and the strong appeal of Bi-based layered perovskites, in this work we carried out the vapor phase deposition by means of RF-magnetron sputtering of the  $\text{Cs}_3\text{Bi}_2(\text{I}_{1-x}\text{Br}_x)_9$  system ( $0 \leq x \leq 1$ ). To date, no vapor phase approaches have been used to prepare  $\text{Cs}_3\text{Bi}_2(\text{I}_{1-x}\text{Br}_x)_9$  films and, in addition, RF-magnetron sputtering has scarcely used for perovskite films notwithstanding its huge potential for scale-up, providing stoichiometry control, good morphology and high crystallinity and quality of deposited films, as we demonstrated recently.<sup>22,23</sup> Together with the structural and optical properties characterization of the deposited films we report a significant photocatalytic activity in organic pollutant degradation combined to excellent water stability of the prepared materials. In the following, we start discussing the two end-members of the solid solution, namely  $\text{Cs}_3\text{Bi}_2\text{Br}_9$  and  $\text{Cs}_3\text{Bi}_2\text{I}_9$ , and then moving to the investigation of the mixed compositions.

### Experimental methods

**Film deposition.** All the thin films have been deposited by means radiofrequency (RF) magnetron sputtering on substrates made by cutting microscope slides (1 mm thick) in 25x25 mm pieces. Substrates have been mechanically cleaned with 2-propanol (Aldrich,  $\geq 99.7\%$ ), sonicated in the same solvent for 15 minutes, and heated at 200°C on a hot plate just before deposition. The targets (diameter 5.08 cm, thickness 1 mm) were made of pressed powders of stoichiometric CsBr/CsI/BiI<sub>3</sub>/BiBr<sub>3</sub> mixtures (Aldrich, 99.9%). Overall starting mass of the target was about 10 grams.

Deposition parameters were: (i) target-to-substrate distance, 10 cm, (ii) RF-power, 50 W (iii) Argon pressure,  $2.3 \times 10^{-2}$  mbar (iv) Argon flux 20 SCCM. The depositions have been carried out in power-control mode. Film thickness has been determined by means of a P-6 stylus profilometer KLA Tencor equipped with a silicon tip (tip radius 2  $\mu\text{m}$ ; applied force 2 mg). After the deposition the films have been heated and cooled in vacuum by using a BÜCHI glass drying oven for 2 hours at 200°C.

**XRD diffraction.** The structural properties of the deposited thin films were characterized by X-ray diffraction (XRD) by means of a Bruker D8 Advance instrument (Cu radiation) in a Bragg–Brentano setup.

**EDX and SEM.** EDX analysis and microstructural characterization of the samples was made using a high-resolution scanning electron microscope (SEM, TESCAN Mira 3) operated at 25 kV.

**AFM.** Atomic Force Microscopy (AFM) images were obtained with an AutoProbe CP microscope (ThermoMicroscopes-Veeco), operating in tapping mode, by means of sharpened silicon tips Nanosensors (resonance frequency: 300 kHz; force constant: 40 N/m). For each analyzed film, scans from 90  $\mu\text{m}$  x 90  $\mu\text{m}$ , to 4  $\mu\text{m}$  x 4  $\mu\text{m}$  have been carried out with a scan rate ranging from 0.5 to 1 Hz. A standard second-order flatten processing of the images has been performed to correct the scanner nonlinearity.

**Absorption and Diffuse Reflectance Spectroscopy.** Ultraviolet-Visible-Near Infrared (UV-Vis-NIR) optical measurements were performed under ambient conditions using a Varian Cary 6000i spectrophotometer equipped with a double

monochromator, a deuterium lamp and a tungsten filament lamp as light sources, a photomultiplier (UV-Vis) and an InGaAs photodiode (NIR) as detectors. Spectral range was 200-1800 nm, in step of 1 nm. Both near normal absorption spectra and diffuse reflectance spectra with a 110 mm diameter integrating sphere were performed.

**Raman Spectroscopy.** Micro-Raman measurements were carried out at room temperature by using a Labram Dilor spectrometer equipped with an Olympus microscope HS BX40. The 632.8 nm light from He-Ne laser was employed as excitation radiation. The samples, mounted on a motorized xy stage, were tested with a 50x objective and with a laser spot of  $\sim 1.5 \mu\text{m}$  of diameter. The spectral resolution was about  $1 \text{ cm}^{-1}$ . A cooled CCD camera was used as a detector and the typical integration times were about 2 minutes. The sample phase homogeneity was verified by performing linear scanning over a length of about  $30 \mu\text{m}$  in three different sample regions. From these scans an average spectrum for each sample has been derived. These spectra were processed by best-fitting procedures based on lorentzian functions.

**Methylene blue Photodegradation.** The methylene blue degradation was conducted in a batch set up. 3 mL of methylene blue solution ( $0.5 \text{ g L}^{-1}$ ) were placed in a quartz cuvette together with the catalyst film, sputtered onto a  $0.8 \text{ cm} \times 4.0 \text{ cm}$  glass substrate. The progress of the reaction was monitored measuring the absorption of the solution at 664 nm. The catalyst film was placed in a direction perpendicular to irradiation path. The irradiation was conducted in a solar box equipped with a Xe lamp, and the irradiance was set to  $250 \text{ W/m}^2$ , to avoid excessive degradation of the methylene blue during the photolysis (without the catalyst). Before the start of the irradiation, the filled cuvette

was kept in the dark for half an hour to enable the establishment of an adsorption-desorption equilibrium between the methylene blue and the thin film. The experiments were repeated 3 times (RSD < 10%).

## Results and discussion

### **Cs<sub>3</sub>Bi<sub>2</sub>I<sub>9</sub> and Cs<sub>3</sub>Bi<sub>2</sub>Br<sub>9</sub> perovskites films**

RF-magnetron sputtering has been adopted to deposit high-quality films of Bi-based layered perovskites starting with the preparation of Cs<sub>3</sub>Bi<sub>2</sub>I<sub>9</sub> and Cs<sub>3</sub>Bi<sub>2</sub>Br<sub>9</sub>.

Cs<sub>3</sub>Bi<sub>2</sub>I<sub>9</sub> films of average thickness of about 500-1000 nm (as determined by profilometry, see Experimental Methods) have been deposited on glass substrates starting from a target composed of stoichiometric amounts of CsI and BiI<sub>3</sub> without substrate heating. Post-deposition thermal treatment has been carried out at 200°C for 2 hours under mild vacuum.

Characterization has been initially carried out by X-ray Diffraction (XRD) checking the crystal structure. Figure 1a displays the film pattern superimposed to the calculated diffraction for hexagonal (*P*6<sub>3</sub>/*mmc* – JCPDS card 01-070-0666) Cs<sub>3</sub>Bi<sub>2</sub>I<sub>9</sub>. There is a perfect match between experimental and calculated data confirming the deposition of single-phase films with good crystallinity as also evidenced by the narrow diffraction peaks. The lattice parameters are *a*=*b*=8.4081(5) Å and *c*=21.1520(8) Å.

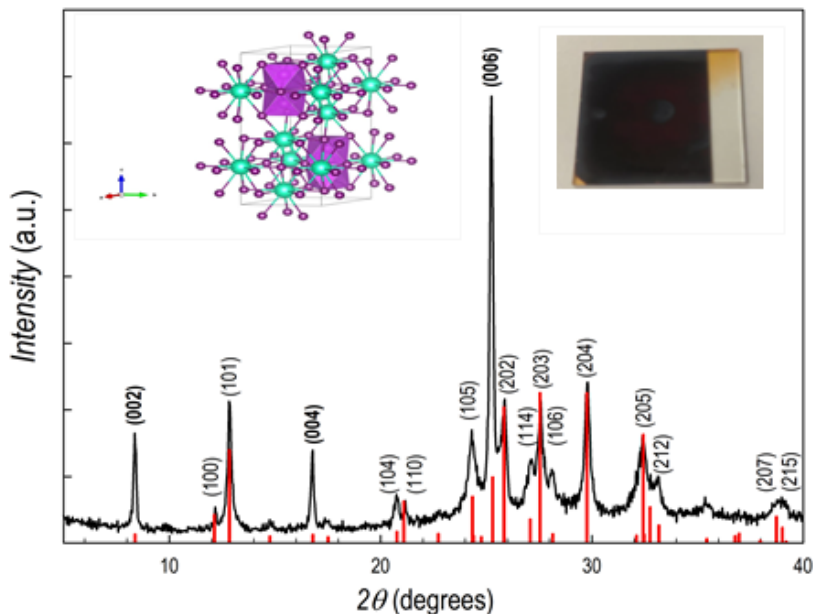


Figure 2.15 XRD pattern of a  $\text{Cs}_3\text{Bi}_2\text{I}_9$  film superimposed to the calculated pattern of the hexagonal structure (vertical red lines), inset: left, photo of the  $\text{Cs}_3\text{Bi}_2\text{I}_9$  film deposited on glass substrate; right: sketch of the crystal structure of  $\text{Cs}_3\text{Bi}_2\text{I}_9$

The inset of Figure 2.15 shows a picture of the film deposited by sputtering which looks dark-red and highly reflective. A sketch of the hexagonal crystal structure is as well reported in the inset of Figure 1a. In addition, a slight preferential orientation along the (00 $l$ ) direction (Miller indexes in bold in Figure 2.15) is observed by comparing expected and experimental intensities. In addition, nearly ( $h0l$ ) fully oriented films can be obtained by slightly changing the depositions conditions and, in general, such an effect is observed for films of thickness of about 500-600 nm. A typical pattern of such an oriented film of  $\text{Cs}_3\text{Bi}_2\text{I}_9$  is shown in Figure 2.16.

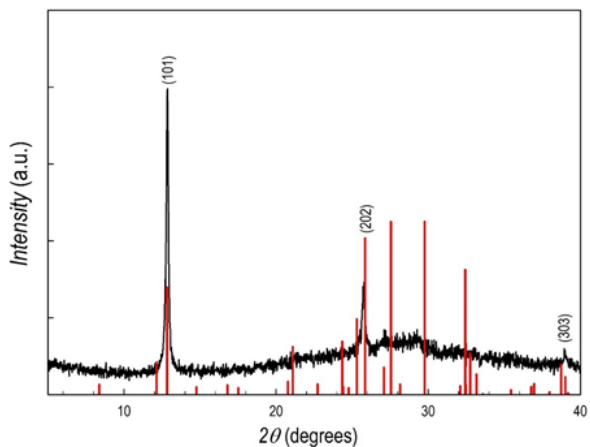


Figure 2.16 XRD pattern of a (h0k) fully oriented film of  $\text{Cs}_3\text{Bi}_2\text{I}_9$ .

Further insight into the film crystal quality has been obtained by Raman spectroscopy. Figure 2.17 shows the spectra of the films reported in Figure 2.15 and 2.16.

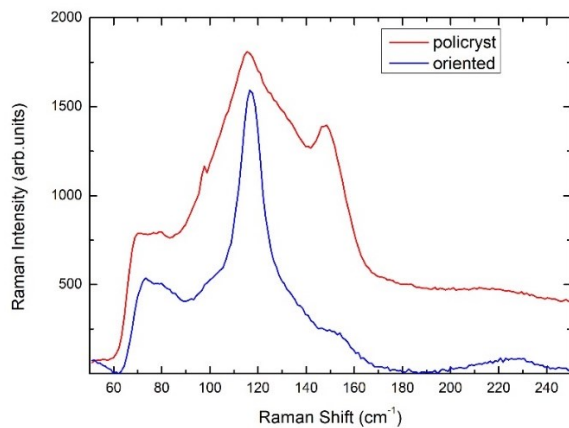


Figure 2.17 Raman spectra of the unoriented (red line) and oriented (blue line)  $\text{Cs}_3\text{Bi}_2\text{I}_9$  film

The spectrum of the unoriented film shows broadened Raman features with respect to reference Raman spectra of a single-crystalline sample of  $\text{Cs}_3\text{Bi}_2\text{I}_9$ .<sup>24</sup> Nevertheless, one can appreciate different peaks: according to ref. 23, bridge Bi-I asymmetric stretch around  $90\text{ cm}^{-1}$ , terminal Bi-I asymmetric stretch around  $120\text{ cm}^{-1}$  and the terminal Bi-I symmetric stretch at about  $150\text{ cm}^{-1}$ , are clearly visible, while other vibrational modes are less defined. On the other hand, for the oriented film, an intrinsic mode selection leads to a Raman spectrum dominated by the signal of asymmetric stretch around  $120\text{ cm}^{-1}$ . Finally, the optical response of  $\text{Cs}_3\text{Bi}_2\text{I}_9$  sputtered films have been determined by Absorption and Diffuse Reflectance spectroscopy. The absorption edge has been first argued at about  $670\text{ nm}$ , *i.e.*  $1.85\text{ eV}$  on films of different thickness. The bandgap has been then better estimated from the extrapolation of the linear part of  $[\text{F(R)}\text{ } h\nu]^2$  where  $\text{F(R)}$  is the Kubelka-Munk function  $\text{F(R)} = (1-R)^2/2R$ , as reported in Figure 2.18 for an oriented  $\text{Cs}_3\text{Bi}_2\text{I}_9$  film.

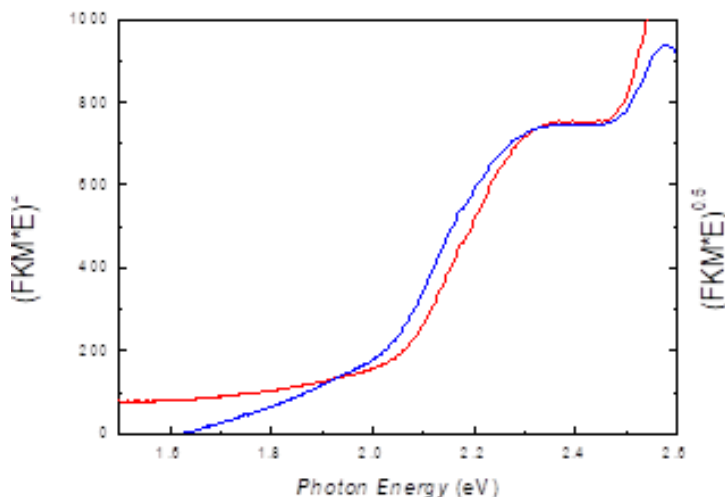


Figure 2.18 Optical absorption edge of an oriented  $\text{Cs}_3\text{Bi}_2\text{I}_9$  film (direct gap red curve and indirect gap blue curve extrapolations)

A clear absorption edge is observed corresponding to a direct bandgap of about 2.0 eV. Such a value is in agreement with the only paper reporting thin films of  $\text{Cs}_3\text{Bi}_2\text{I}_9$  prepared by spin-coating where, however, the authors observed a more structured absorption edge identifying a direct and an indirect band-gap.<sup>25</sup> The indirect gap edge is estimated at 1.96 eV (blue curve) from the indirect-gap extrapolation of the linear part of  $[F(R) h\nu]^{1/2}$ .  $\text{Cs}_3\text{Bi}_2\text{Br}_9$  films have been deposited starting from stoichiometric amounts of  $\text{CsBr}$  and  $\text{BiBr}_3$  followed by a thermal treatment at 200°C for 2 hours under mild dynamic vacuum (as for the  $\text{Cs}_3\text{Bi}_2\text{I}_9$  material).



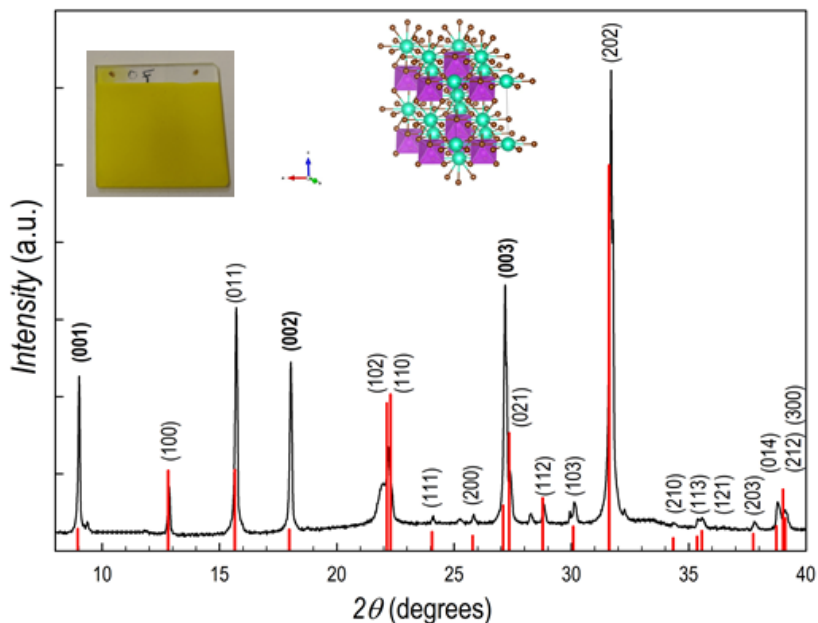


Figure 2.19 XRD pattern of  $\text{Cs}_3\text{Bi}_2\text{Br}_9$  film superimposed to the calculated pattern of the  $\text{Cs}_3\text{Bi}_2\text{Br}_9$  crystal structure (red lines), inset: from the left: typical aspect of deposited film and sketch of the crystal structure of  $\text{Cs}_3\text{Bi}_2\text{Br}_9$

This approach allowed us to prepare single-phase, highly crystalline  $\text{Cs}_3\text{Bi}_2\text{Br}_9$  films as shown in Figure 2.19, with the typical aspect of the yellow film reported in the inset.  $\text{Cs}_3\text{Bi}_2\text{Br}_9$  films grow in the trigonal crystal structure ( $P-3m$  – JCPDS card 01-070-0493) as sketched in the inset of the Figure, with a slight preferential growth along the  $(00l)$  direction (Miller indexes in bold in Figure 2.19) as can be inferred by comparing the experimental pattern with the calculated one (vertical red lines). Raman spectroscopy has been used also in this case to further probe the film structure.

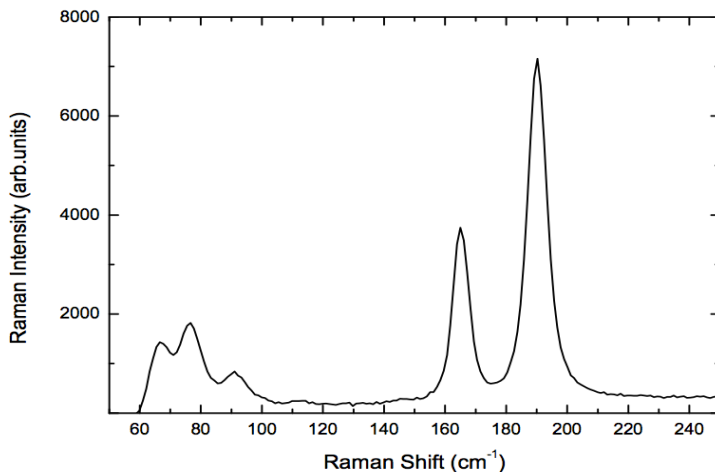


Figure 2.20 Raman scattering spectrum of single-phase  $\text{Cs}_3\text{Bi}_2\text{Br}_9$  film

Figure 2.20 shows the Raman spectrum of a single-phase  $\text{Cs}_3\text{Bi}_2\text{Br}_9$  film which is in excellent agreement with published data.<sup>24</sup> Indeed, the two expected  $A_{1g}$  and  $E_g$  normal modes give strong Raman features centered at  $\sim 190 \text{ cm}^{-1}$  and  $165 \text{ cm}^{-1}$ , respectively, as a result of Bi-Br vibrations inside the corner-sharing  $[\text{BiBr}_6]^{3-}$  octahedra. Additional weaker Raman features are correctly measured at 91, 76 and  $66 \text{ cm}^{-1}$ . The high quality of the obtained structure is confirmed by the FWHM values of  $A_{1g}$  and  $E_g$  bands ( $6.9$  and  $5.3 \text{ cm}^{-1}$  respectively), very close to the values obtained for single crystals.<sup>26</sup>

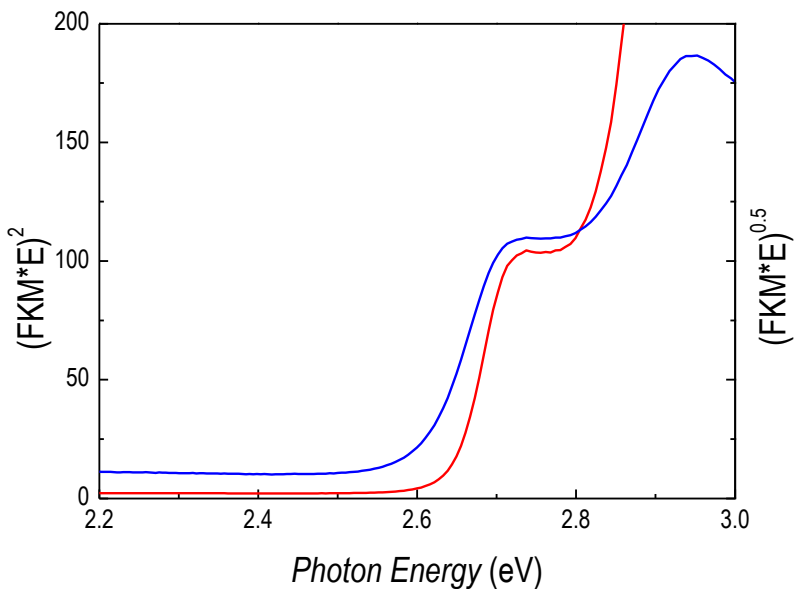


Figure 2.21 Optical absorption edge of the same film (direct gap red curve and indirect gap blue curve extrapolations)

The optical response is blue-shifted with respect to  $\text{Cs}_3\text{Bi}_2\text{I}_9$ , as shown in Figure 2.21, and is characterized by a sharp edge corresponding to a band-gap of about 2.64 eV to be compared to the value of 2.67 eV reported for the only available  $\text{Cs}_3\text{Bi}_2\text{Br}_9$  film study in current literature.<sup>2</sup> Indirect edge is at 2.6 eV (blue curve). The presence of a direct and indirect band gap in  $\text{Cs}_3\text{Bi}_2\text{Br}_9$  has been described in detail by Zhang and co-workers.<sup>27</sup>

So far it has been demonstrated the first successful application of RF-magnetron sputtering to growth high-quality, single-phase  $\text{Cs}_3\text{Bi}_2\text{I}_9$  and  $\text{Cs}_3\text{Bi}_2\text{Br}_9$  films, reporting also the first vapor phase growth on these Bi-based perovskite derivatives. The two compositions have distinct crystal structures and optical properties which, as shown in the next section, can be tuned by

halide alloying, also providing a demonstration of the effectiveness of sputtering method to grow mixed phases.

### Mixed $\text{Cs}_3\text{Bi}_2(\text{I}_{1-x}\text{Br}_x)_9$ ( $0 \leq x \leq 1$ ) films

Mixed  $\text{Cs}_3\text{Bi}_2(\text{I}_{1-x}\text{Br}_x)_9$  ( $0 \leq x \leq 1$ ) have been grown by RF-magnetron sputtering according to the experimental conditions. Figure 2.22 reports the XRD patterns of a series of mixed films of average thickness of about 300 nm as a function of  $x$  (bromide content).

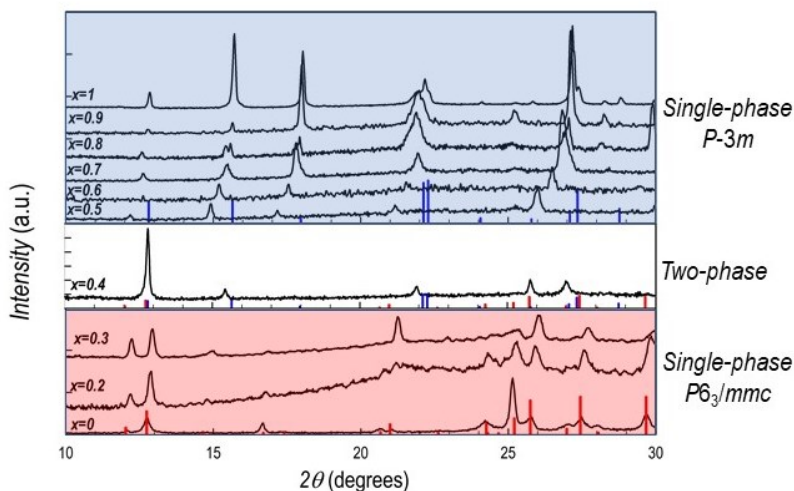


Figure 2.22 XRD pattern of the  $\text{Cs}_3\text{Bi}_2(\text{I}_{1-x}\text{Br}_x)_9$  ( $0 \leq x \leq 1$ ) series of films

EDX analysis was used to determine the effective Br/I content which resulted to be very close to the nominal one with deviations of the order of  $\pm 5\%$ . EDS analysis also confirmed the good atomic homogeneity of the prepared films.

For the range  $0 \leq x \leq 0.3$  the crystal structure of the mixed compositions is the same as that of  $\text{Cs}_3\text{Bi}_2\text{I}_9$  ( $P6_3/mmc$ ), with the diffraction lines of the samples showing a progressive shift

towards higher angle (smaller lattice parameters) by increasing the Br-amount. At  $x$  around 0.4, the XRD pattern shows the presence of the characteristic diffraction peaks of  $\text{Cs}_3\text{Bi}_2\text{I}_9$  (with significant preferential orientation along the  $00l$  reflections) together with the appearance of diffraction peaks related to the trigonal crystal structure of  $\text{Cs}_3\text{Bi}_2\text{Br}_9$  ( $P-3m$ , marked with an asterisk in Figure 5a) which are, in addition, found at significant lower angles with respect to reference structure (vertical red lines of the top part of Figure 2.22), indicating a bigger unit cell due to iodide presence. By further increasing the Br-amount,  $x$ , to 0.5, single-phase samples in mixed system  $\text{Cs}_3\text{Bi}_2(\text{I}_{1-x}\text{Br}_x)_9$  are found. Now, the crystal structure is compatible with that of  $\text{Cs}_3\text{Bi}_2\text{Br}_9$ . As it can be appreciated by the top panel of Figure 2.22, and with reference to the reflection of  $\text{Cs}_3\text{Bi}_2\text{Br}_9$  (vertical blue bars), the diffraction peaks of the mixed compositions in the  $0.5 \leq x \leq 0.9$  range are shift to lower angles as a result of the presence of bigger I which increases the cell volume. The trend of lattice volume, determined by profile matching of the diffraction patterns, for the series of films reported in Figure 2.22 is shown in Figure 2.23.

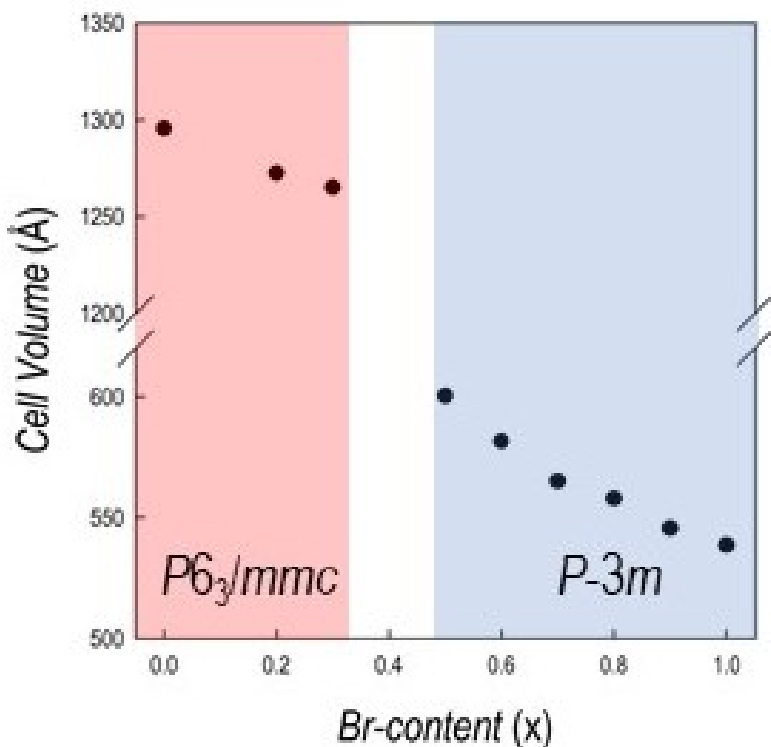


Figure 2.23 Trend of lattice volume of  $\text{Cs}_3\text{Bi}_2(\text{I}_{1-x}\text{Br}_x)_9$  ( $0 \leq x \leq 1$ ) films as a function of Br-content

It is observed a roughly linear trend of  $V$  in the two regions of phase stability, with different slopes, as a function of bromide content.

The present results mark a transition from hexagonal to trigonal symmetry at about  $x=0.3$ , *i.e.*  $\text{Cs}_3\text{Bi}_2\text{I}_{6.3}\text{Br}_{2.7}$ , a small intermediate region of mixed-phase samples, and another region of single-phase mixed compositions with trigonal symmetry

from  $\text{Cs}_3\text{Bi}_2\text{I}_{4.5}\text{Br}_{4.5}$  to  $\text{Cs}_3\text{Bi}_2\text{Br}_9$ . The data reported on spin-coated films by Yu *et al.* evidenced a similar phase transition at a composition equal to  $\text{Cs}_3\text{Bi}_2\text{I}_6\text{Br}_3$ , indicating the existence of mixed samples around  $\text{Cs}_3\text{Bi}_2\text{I}_7\text{Br}_2$ , while alloying in the analogous system in form of nanocrystals occurs at  $\text{Cs}_3\text{Bi}_2\text{I}_{3.6}\text{Br}_{5.4}$  in excellent agreement with the present data.<sup>6</sup> Morphological characterization of some selected films of the  $\text{Cs}_3\text{Bi}_2(\text{I}_{1-x}\text{Br}_x)_9$  ( $0 \leq x \leq 1$ ) series has been assessed by Atomic Force Microscopy (AFM).

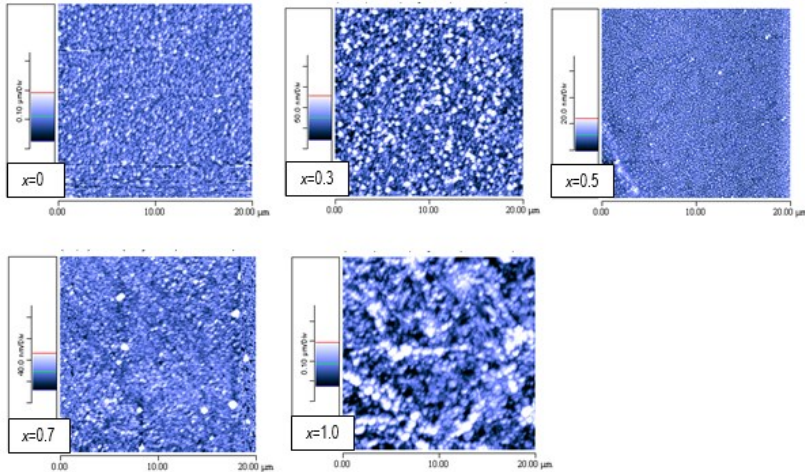


Figure 2.24 AFM images on  $20 \times 20 \mu\text{m}$  area for  $\text{Cs}_3\text{Bi}_2(\text{I}_{1-x}\text{Br}_x)_9$  samples for  $x=0$ , 0.3, 0.5, 0.7 and 1

In Figure 2.24 are reported the images collected on  $20 \times 20 \mu\text{m}$  area for films at  $x=0$ , 0.3, 0.5, 0.7 and 1. From the  $90 \times 90 \mu\text{m}$  area images it is evident that the RF-magnetron sputtering method provides a very good substrate coverage. The RMS roughness spans from 15 to 60 nm, with no clear trend as a function of the Br content with a value around 30 nm for  $\text{Cs}_3\text{Bi}_2\text{I}_9$  and around 60 nm for  $\text{Cs}_3\text{Bi}_2\text{Br}_9$ . From the images in Figure 2.24 (and the  $4 \times 4 \mu\text{m}$  in SI) it is possible to note that the

films are composed of small particles of about 50-300 nm depending on the composition (*e.g.*, average grains size around 40-70 nm for  $\text{Cs}_3\text{Bi}_2\text{I}_9$  and around 200-300 nm for  $\text{Cs}_3\text{Bi}_2\text{Br}_9$ ). In general, there are no significant differences in film morphology, apart from the slightly less compacted film obtained for  $\text{Cs}_3\text{Bi}_2\text{Br}_9$ .

The behavior derived from XRD results for mixed samples is further confirmed by Raman data. Room temperature Raman spectra have been registered for all the investigated samples in the region  $50\text{-}1000\text{ cm}^{-1}$ .

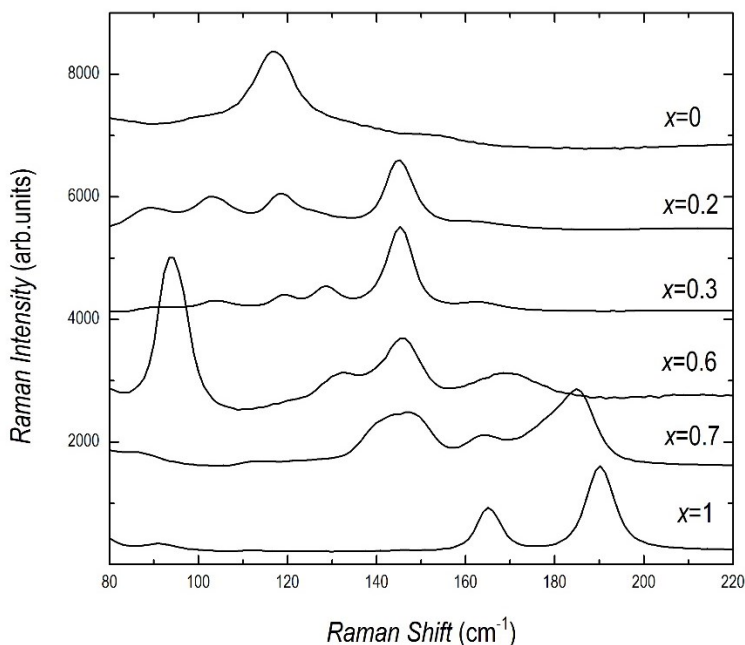


Figure 2.25 Raman spectra at room temperature of different mixed samples plotted with the two end-members



In Figure 2.25, for ease of viewing, a selection of mixed samples is reported in the region  $80\text{-}220\text{ cm}^{-1}$  where a Raman yield can be measured. The Raman spectra from the two end-members are also reported for comparison. The spectra in Figure 2.25 result by averaging all the spectra obtained from linear scans. This protocol allowed to check the homogeneity of the Raman behavior the deposited films from different sample regions. In particular, for  $x < 0.4$  and  $x > 0.6$ , the films exhibit a higher degree of homogeneity.

The initial substitution of I by Br leads to a Raman spectrum dominated by the typical A' mode due to terminal Bi-I symmetric vibrations in  $\text{Cs}_3\text{Bi}_2\text{I}_9$ , differently from what already observed for the pure sample, whose spectrum is mainly due to the mode at about  $117.0\text{ cm}^{-1}$  attributed to terminal Bi-I asymmetric vibrations. This fact confirms that the addition of low amounts of Br leads to films with a crystal structure equal to that of  $\text{Cs}_3\text{Bi}_2\text{I}_9$  but with different orientation, in accordance with XRD data. Increasing the Br alloying causes the increasing Raman activity at energies higher than  $160\text{ cm}^{-1}$ . A very weak signal at around  $162\text{ cm}^{-1}$  is already present in the spectrum for the sample with  $x=0.3$  and become more and more pronounced with clear blue-shifting with increasing the Br content. In the range  $0.3 < x < 0.6$  it is possible to observe Raman features pertinent to both crystal structures. Indeed, the Raman spectrum in the region  $100\text{-}200\text{ cm}^{-1}$  were obtained for the sample with  $x = 0.5$  during a linear scan. The data are interpolated by a superposition of six lorentzian curves evidencing a mixing between the two phases. It is important to underline that this kind of spectra are in any case rarely observed and, by averaging over 15 spectra, the contribution from the minority phase tends to be smeared out. At higher Br amounts, the Raman activity in the region  $80\text{-}150\text{ cm}^{-1}$  decreases indicating that the contribution from Bi-I vibrations is gradually quenched while, on the

contrary, that from Bi-Br is strengthened. The transition between the two different crystal structures can be further appreciated by monitoring Raman band parameters as reported in Figure 2.26.

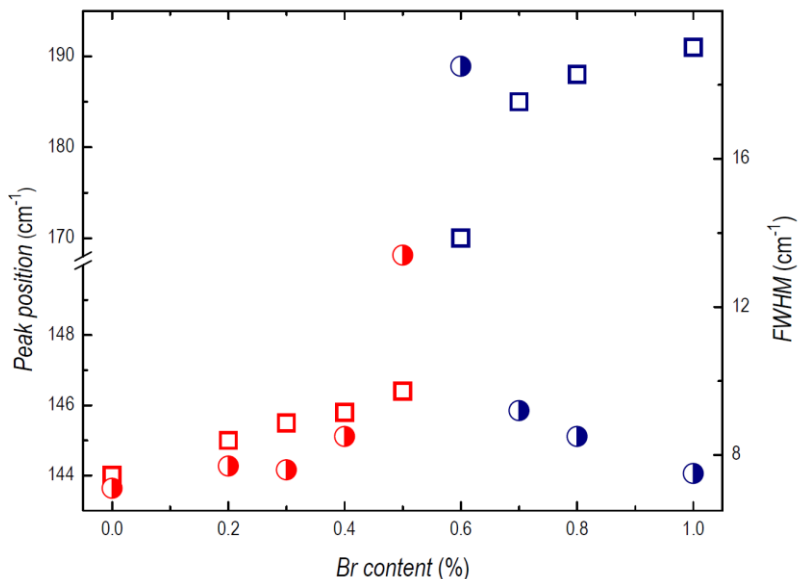


Figure 2.26 Peak position (open symbols) and linewidth (fully symbols) for the Raman bands corresponding to A' mode in  $\text{Cs}_3\text{Bi}_2\text{I}_9$  (squares) and to  $\text{A}_{1g}$  mode in  $\text{Cs}_3\text{Bi}_2\text{Br}_9$  (circles)

The Raman modes we used as reference are the already mentioned A' symmetric mode, involving terminal Bi-I vibrations, for  $\text{Cs}_3\text{Bi}_2\text{I}_9$ , and the  $\text{A}_{1g}$  mode due to the Bi-Br vibrations inside the corner-sharing  $[\text{BiBr}_6]^{3-}$  octahedra in  $\text{Cs}_3\text{Bi}_2\text{Br}_9$ , peaked in pure samples at  $144.0 \text{ cm}^{-1}$  and  $191.0 \text{ cm}^{-1}$ , respectively. According to Yu *et al.*, the insertion of Br causes a small blue-shift of the A' phonon energy with an hardening of the mode of about  $2 \text{ cm}^{-1}$  for the  $x=0.4$  sample.<sup>2</sup> On the other hand, the linewidth of this Raman mode increases markedly as

the result of the disordering due to the Br insertion in the Bi-I vibrations units. At higher Br amounts the Raman fingerprints of the trigonal crystal structure ( $P-3m$ ) appear at around  $160\text{ cm}^{-1}$ . The broadened and unresolved feature denotes a higher disorder degree which is gradually quenched leading to the fully ordered phase in pure sample. In this case the blue-shift of  $A_{1g}$  mode is greater than that observed for  $A'$  mode but this is consistent with the contraction of cell volume and the involved anion masses. The higher disorder in the mid-range of substitution and the presence of Raman features ascribable to both crystal systems indicate the presence of a mixed phase.

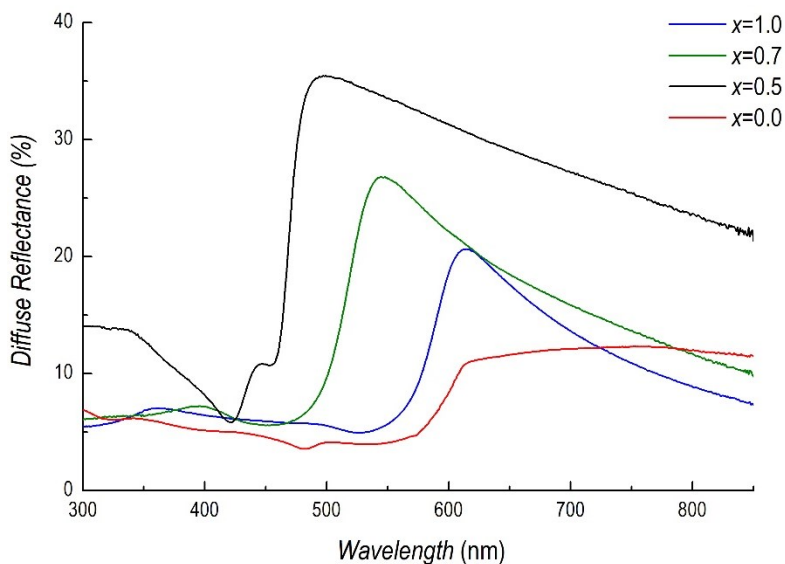


Figure 2.27 Diffuse reflectance spectra of different mixed  $\text{Cs}_3\text{Bi}_2(\text{I}_{1-x}\text{Br}_x)_9$  samples plotted with the two end-members

Figure 2.27 reports the diffuse reflectance spectra of selected films (for ease of representation) for the  $\text{Cs}_3\text{Bi}_2(\text{I}_{1-x}\text{Br}_x)_9$  system showing a clear blue-shift from  $x=0$  to  $x=1$ . The direct gap energy for all the films considered shows a progressive shift of the fundamental absorption edge towards higher energies with increasing Br content, with a good linear trend all through the visible range (Figure 2.28) and with a slight deviation at  $x=0.5$  which could be possibly correlated to the Raman results indicating, locally, a mixed-phase nature of the sample.

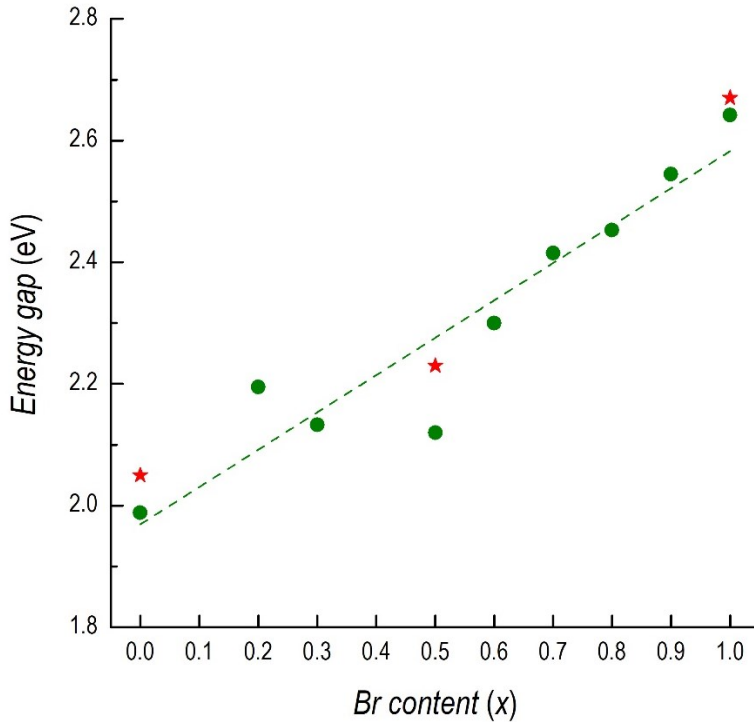


Figure 2.28 Fundamental gap energy trend (dots) with linear trend interpolation and the comparison with literature data (asterisks)

The monotonic bandgap variation with increasing the Br content, as shown in Figure 2.28, well follows the literature trend, as experimentally observed by Gu et al. on only three compositions.<sup>25</sup>

Finally, we report in the present work some preliminary results aiming at testing the photocatalytic properties of  $\text{Cs}_3\text{Bi}_2\text{I}_9$  and  $\text{Cs}_3\text{Bi}_2\text{Br}_9$  films, which have been assessed by determining their ability in the photodegradation of an organic dye by selecting methylene blue (MB) as a representative model compound of this class. As mentioned in the Introduction,  $\text{Cs}_3\text{Bi}_2\text{I}_9$  and  $\text{Cs}_3\text{Bi}_2\text{Br}_9$  have attracted a significant recent interest due to their relevant photoactivity which however has been to date determined on powdered samples.<sup>18,19</sup>

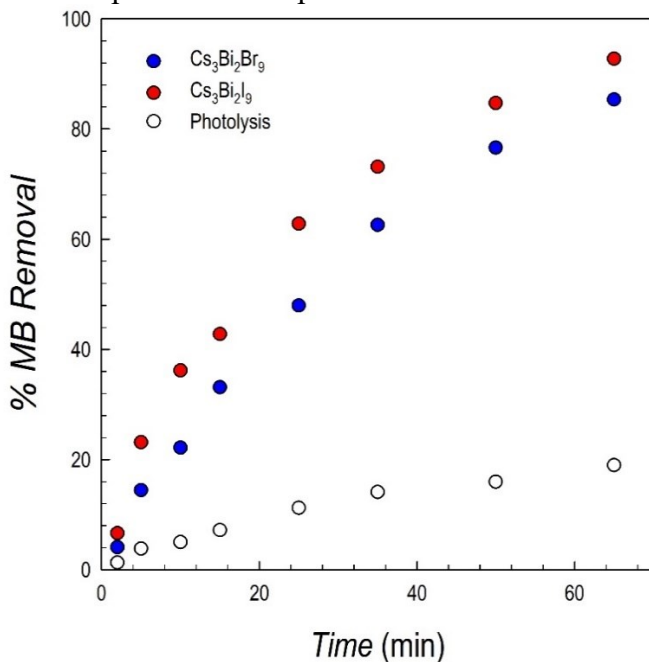


Figure 2.29 Percent of MB removal as a function of irradiation time for  $\text{Cs}_3\text{Bi}_2\text{I}_9$  (red dots) and  $\text{Cs}_3\text{Bi}_2\text{Br}_9$  (blue dots) films, compared to the photolysis effect (empty dots); conditions:  $0.5 \text{ g L}^{-1}$  catalyst,  $250 \text{ W m}^{-2}$  simulated solar light. RSD < 10% ( $n = 3$ ).

Figure 2.29 shows the variation of percentage removal of MB (calculated as  $C_0 - C/C_0$  where  $C_0$  is the initial concentration) as a function of irradiation time, compared to that of direct photolysis.

It is clear from the Figure above that the two films have a relevant activity in the degradation of MB which provides the first evidence of photoactivity by  $\text{Cs}_3\text{Bi}_2\text{Br}_9$  and  $\text{Cs}_3\text{Bi}_2\text{I}_9$  thin films. Slightly different behavior in the MB degradation between the two compositions may be the result of morphology/grain size effects (see AFM data above). The degradation of MB was also investigated concerning the kinetics. For quantitative evaluation, experimental data for MB photodegradation were fitted to different kinetic equations to determine the suitable model to represent the kinetics of degradation.<sup>28</sup> Plotting the natural logarithm of the ratio between the original concentration and the concentration after photocatalytic degradation  $\ln([\text{MB}_0]/[\text{MB}]_t)$  versus the irradiation time (min) provided a linear relationship. The apparent first-order rate constants ( $\text{min}^{-1}$ ) were 0.0295 and 0.0389 for  $\text{Cs}_3\text{Bi}_2\text{Br}_9$  and  $\text{Cs}_3\text{Bi}_2\text{I}_9$  films, respectively. Concerning the mechanism of MB degradation, previous data on bulk  $\text{Cs}_3\text{Bi}_2\text{Br}_9$  and  $\text{Cs}_3\text{Bi}_2\text{I}_9$  indicated that the MB degradation occurs via the formation of hydroxyl radicals.<sup>29,30</sup> These promising results open the way to further explore the application of Bi-based perovskites in a series of relevant photocatalytic reactions.

## Conclusions

In the present paper we provide and demonstrate an efficient vapor deposition route for the preparation of single-phase, high-quality films of  $\text{Cs}_3\text{Bi}_2\text{Br}_9$  and  $\text{Cs}_3\text{Bi}_2\text{I}_9$  based on RF-magnetron

sputtering, which is a simple and effective method making use of a single target source. The films have been characterized in terms of crystal structure, morphology, optical and Raman spectroscopies and by assessing preliminary photocatalytic activity by investigating the solar-driven MB degradation. RF-sputtering has been also successfully employed to prepare mixed I/Br films  $\text{Cs}_3\text{Bi}_2(\text{I}_{1-x}\text{Br}_x)_9$  ( $0 \leq x \leq 1$ ), confirming the suitability of this approach in preparing alloyed compositions with a very good stoichiometry control, as well. A structural phase transition has been observed at about  $x=0.4$ , as confirmed by X-ray diffraction with a scaling of lattice parameters with halide content. Raman spectroscopy revealed to be effective in following the structural evolution of mixed compositions. Finally, a variation of the fundamental bandgap from 2.0 eV for  $\text{Cs}_3\text{Bi}_2\text{I}_9$  to about 2.64 eV for  $\text{Cs}_3\text{Bi}_2\text{Br}_9$  has been observed with a tuning of the  $E_g$  between the two end-members achieved in the mixed compositions. To conclude, this paper demonstrates the efficiency of sputtering in preparing thin films of all-inorganic lead-free Bi-based perovskites which are of huge interest for the wide community of photovoltaics, optoelectronics and, more recently, photocatalysis. As we already demonstrated for other metal halide perovskites, sputtering seems to be a method to be extended to several systems to further boost the scale-up of perovskite-based technology, in particular for all-inorganic systems which face relevant problems in wet-chemistry depositions.<sup>21-23</sup>

## References

- (1) Jin, Z.; Zhang, Z.; Xiu, J.; Song, H.; Gatti, T.; He, Z. A Critical Review on Bismuth and Antimony Halide Based Perovskites and Their Derivatives for Photovoltaic

- Applications: Recent Advances and Challenges. *J. Mater. Chem. A* 2020, 8 (32), 16166–16188. <https://doi.org/10.1039/D0TA05433J>.
- (2) Yu, B.-B.; Liao, M.; Yang, J.; Chen, W.; Zhu, Y.; Zhang, X.; Duan, T.; Yao, W.; Wei, S.-H.; He, Z. Alloy-Induced Phase Transition and Enhanced Photovoltaic Performance: The Case of Cs<sub>3</sub>Bi<sub>2</sub>I<sub>9</sub>–xBr<sub>x</sub> Perovskite Solar Cells. *J. Mater. Chem. A* 2019, 7 (15), 8818–8825. <https://doi.org/10.1039/C9TA01978B>.
- (3) Waykar, R.; Bhorde, A.; Nair, S.; Pandharkar, S.; Gabhale, B.; Aher, R.; Rondiya, S.; Waghmare, A.; Doiphode, V.; Punde, A.; Vairale, P.; Prasad, M.; Jadkar, S. Environmentally Stable Lead-Free Cesium Bismuth Iodide (Cs<sub>3</sub>Bi<sub>2</sub>I<sub>9</sub>) Perovskite: Synthesis to Solar Cell Application. *Journal of Physics and Chemistry of Solids* 2020, 146, 109608. <https://doi.org/10.1016/j.jpcs.2020.109608>.
- (4) Pazoki, M.; Johansson, M. B.; Zhu, H.; Broqvist, P.; Edvinsson, T.; Boschloo, G.; Johansson, E. M. J. Bismuth Iodide Perovskite Materials for Solar Cell Applications: Electronic Structure, Optical Transitions, and Directional Charge Transport. *J. Phys. Chem. C* 2016, 120 (51), 29039–29046. <https://doi.org/10.1021/acs.jpcc.6b11745>.
- (5) Liu, D.; Yu, B.-B.; Liao, M.; Jin, Z.; Zhou, L.; Zhang, X.; Wang, F.; He, H.; Gatti, T.; He, Z. Self-Powered and Broadband Lead-Free Inorganic Perovskite Photodetector with High Stability. *ACS Appl. Mater. Interfaces* 2020, 12 (27), 30530–30537. <https://doi.org/10.1021/acsami.0c05636>.
- (6) Ghosh, S.; Mukhopadhyay, S.; Paul, S.; Pradhan, B.; De, S. K. Control Synthesis and Alloying of Ambient Stable Pb-Free Cs<sub>3</sub>Bi<sub>2</sub>Br<sub>9(1-x)</sub>I<sub>9x</sub> (0 ≤ x ≤ 1) Perovskite Nanocrystals for Photodetector Application. *ACS Appl. Nano Mater.* 2020, 3 (11), 11107–11117. <https://doi.org/10.1021/acsanm.0c02288>.



- (7) Chen, G.; Wang, P.; Wu, Y.; Zhang, Q.; Wu, Q.; Wang, Z.; Zheng, Z.; Liu, Y.; Dai, Y.; Huang, B. Lead-Free Halide Perovskite  $\text{Cs}_3\text{Bi}_{2x}\text{Sb}_{2-2x}\text{I}_9$  ( $x \approx 0.3$ ) Possessing the Photocatalytic Activity for Hydrogen Evolution Comparable to That of  $(\text{CH}_3\text{NH}_3)\text{PbI}_3$ . *Advanced Materials* 2020, 32 (39), 2001344. <https://doi.org/10.1002/adma.202001344>.
- (8) Dai, Y.; Poidevin, C.; Ochoa-Hernández, C.; Auer, A. A.; Tüysüz, H. A Supported Bismuth Halide Perovskite Photocatalyst for Selective Aliphatic and Aromatic C–H Bond Activation. *Angewandte Chemie International Edition* 2020, 59 (14), 5788–5796. <https://doi.org/10.1002/anie.201915034>.
- (9) Han, J. S.; Le, Q. V.; Kim, H.; Lee, Y. J.; Lee, D. E.; Im, I. H.; Lee, M. K.; Kim, S. J.; Kim, J.; Kwak, K. J.; Choi, M.-J.; Lee, S. A.; Hong, K.; Kim, S. Y.; Jang, H. W. Lead-Free Dual-Phase Halide Perovskites for Preconditioned Conducting-Bridge Memory. *Small* 2020, 16 (41), 2003225. <https://doi.org/10.1002/smll.202003225>.
- (10) Bhosale, S. S.; Kharade, A. K.; Jokar, E.; Fathi, A.; Chang, S.; Diau, E. W.-G. Mechanism of Photocatalytic  $\text{CO}_2$  Reduction by Bismuth-Based Perovskite Nanocrystals at the Gas–Solid Interface. *J. Am. Chem. Soc.* 2019, 141 (51), 20434–20442. <https://doi.org/10.1021/jacs.9b11089>.
- (11) Dai, Y.; Tüysüz, H. Lead-Free  $\text{Cs}_3\text{Bi}_2\text{Br}_9$  Perovskite as Photocatalyst for Ring-Opening Reactions of Epoxides. *ChemSusChem* 2019, 12 (12), 2587–2592. <https://doi.org/10.1002/cssc.201900716>.
- (12) Shi, M.; Li, G.; Tian, W.; Jin, S.; Tao, X.; Jiang, Y.; Pidko, E. A.; Li, R.; Li, C. Understanding the Effect of Crystalline Structural Transformation for Lead-Free Inorganic Halide Perovskites. *Advanced Materials* 2020, 32 (31), 2002137. <https://doi.org/10.1002/adma.202002137>.
- (13) Tran, M. N.; Cleveland, I. J.; Aydil, E. S. Resolving the Discrepancies in the Reported Optical Absorption of Low-

Dimensional Non-Toxic Perovskites,  $\text{Cs}_3\text{Bi}_2\text{Br}_9$  and  $\text{Cs}_3\text{BiBr}_6$ . J. Mater. Chem. C 2020, 8 (30), 10456–10463. <https://doi.org/10.1039/D0TC02783A>.

(14) Timmermans, C. W. M.; Blasse, G. The Luminescence and Photoconductivity of  $\text{Cs}_3\text{Bi}_2\text{Br}_9$  Single Crystals. Journal of Luminescence 1981, 24–25, 75–78. [https://doi.org/10.1016/0022-2313\(81\)90224-6](https://doi.org/10.1016/0022-2313(81)90224-6).

(15) Timmermans, C. W. M.; Blasse, G. On the Luminescence of  $\text{Cs}_3\text{Bi}_2\text{Br}_9$  Single Crystals. physica status solidi (b) 1981, 106 (2), 647–655. <https://doi.org/10.1002/pssb.2221060230>.

(16) Timmermans, C. W. M.; Cholakh, S. O.; van der Woude, R. L.; Blasse, G. Some Optical and Electrical Measurements on  $\text{Cs}_3\text{Bi}_2\text{Br}_9$  Single Crystals. physica status solidi (b) 1983, 115 (1), 267–271. <https://doi.org/10.1002/pssb.2221150130>.

(17) Li, W.-G.; Wang, X.-D.; Liao, J.-F.; Jiang, Y.; Kuang, D.-B. Enhanced On–Off Ratio Photodetectors Based on Lead-Free  $\text{Cs}_3\text{Bi}_2\text{I}_9$  Single Crystal Thin Films. Advanced Functional Materials 2020, 30 (12), 1909701. <https://doi.org/10.1002/adfm.201909701>.

(18) Bresolin, B.-M.; Günnemann, C.; Bahnemann, D. W.; Sillanpää, M. Pb-Free  $\text{Cs}_3\text{Bi}_2\text{I}_9$  Perovskite as a Visible-Light-Active Photocatalyst for Organic Pollutant Degradation. Nanomaterials 2020, 10 (4), 763. <https://doi.org/10.3390/nano10040763>.

(19) Bresolin, B.-M.; Sgarbossa, P.; Bahnemann, D. W.; Sillanpää, M.  $\text{Cs}_3\text{Bi}_2\text{I}_9/\text{g-C}_3\text{N}_4$  as a New Binary Photocatalyst for Efficient Visible-Light Photocatalytic Processes. Separation and Purification Technology 2020, 251, 117320. <https://doi.org/10.1016/j.seppur.2020.117320>.

(20) Morgan, E. E.; Mao, L.; Teicher, S. M. L.; Wu, G.; Seshadri, R. Tunable Perovskite-Derived Bismuth Halides:

- Cs<sub>3</sub>Bi<sub>2</sub>(Cl<sub>1-x</sub>I<sub>x</sub>)<sub>9</sub>. *Inorg. Chem.* 2020, 59 (6), 3387–3393. <https://doi.org/10.1021/acs.inorgchem.9b03415>.
- (21) Bonomi, S.; Malavasi, L. Physical and Chemical Vapor Deposition Methods Applied to All-Inorganic Metal Halide Perovskites. *Journal of Vacuum Science & Technology A* 2020, 38 (6), 060803. <https://doi.org/10.1116/6.0000568>.
- (22) Bonomi, S.; Patrini, M.; Bongiovanni, G.; Malavasi, L. Versatile Vapor Phase Deposition Approach to Cesium Tin Bromide Materials CsSnBr<sub>3</sub>, CsSn<sub>2</sub>Br<sub>5</sub> and Cs<sub>2</sub>SnBr<sub>6</sub>. *RSC Adv.* 2020, 10 (48), 28478–28482. <https://doi.org/10.1039/D0RA04680A>.
- (23) Bonomi, S.; Marongiu, D.; Sestu, N.; Saba, M.; Patrini, M.; Bongiovanni, G.; Malavasi, L. Novel Physical Vapor Deposition Approach to Hybrid Perovskites: Growth of MAPbI<sub>3</sub> Thin Films by RF-Magnetron Sputtering. *Scientific Reports* 2018, 8 (1), 15388. <https://doi.org/10.1038/s41598-018-33760-w>.
- (24) McCall, K. M.; Stoumpos, C. C.; Kostina, S. S.; Kanatzidis, M. G.; Wessels, B. W. Strong Electron–Phonon Coupling and Self-Trapped Excitons in the Defect Halide Perovskites A<sub>3</sub>M<sub>2</sub>I<sub>9</sub> (A = Cs, Rb; M = Bi, Sb). *Chem. Mater.* 2017, 29 (9), 4129–4145. <https://doi.org/10.1021/acs.chemmater.7b01184>.
- (25) Gu, J.; Yan, G.; Lian, Y.; Mu, Q.; Jin, H.; Zhang, Z.; Deng, Z.; Peng, Y. Bandgap Engineering of a Lead-Free Defect Perovskite Cs<sub>3</sub>Bi<sub>2</sub>I<sub>9</sub> through Trivalent Doping of Ru<sup>3+</sup>. *RSC Adv.* 2018, 8 (45), 25802–25807. <https://doi.org/10.1039/C8RA04422H>.
- (26) Bator, G.; Baran, J.; Jakubas, R.; Karbowiak, M. Raman Studies of Structural Phase Transition in Cs<sub>3</sub>Bi<sub>2</sub>Br<sub>9</sub>. *Vibrational Spectroscopy* 1998, 16 (1), 11–20. [https://doi.org/10.1016/S0924-2031\(97\)00041-6](https://doi.org/10.1016/S0924-2031(97)00041-6).

- (27) Zhang, Y.; Yin, J.; Parida, M. R.; Ahmed, G. H.; Pan, J.; Bakr, O. M.; Brédas, J.-L.; Mohammed, O. F. Direct-Indirect Nature of the Bandgap in Lead-Free Perovskite Nanocrystals. *J. Phys. Chem. Lett.* 2017, 8 (14), 3173–3177. <https://doi.org/10.1021/acs.jpclett.7b01381>.
- (28) Riaz, N.; Hassan, M.; Siddique, M.; Mahmood, Q.; Farooq, U.; Sarwar, R.; Khan, M. S. Photocatalytic Degradation and Kinetic Modeling of Azo Dye Using Bimetallic Photocatalysts: Effect of Synthesis and Operational Parameters. *Environmental Science and Pollution Research* 2020, 27 (3), 2992–3006. <https://doi.org/10.1007/s11356-019-06727-1>.
- (29) Bresolin, B.-M.; Balayeva, N. O.; Granone, L. I.; Dillert, R.; Bahnemann, D. W.; Sillanpää, M. Anchoring Lead-Free Halide  $\text{Cs}_3\text{Bi}_2\text{I}_9$  Perovskite on UV100– $\text{TiO}_2$  for Enhanced Photocatalytic Performance. *Solar Energy Materials and Solar Cells* 2020, 204, 110214. <https://doi.org/10.1016/j.solmat.2019.110214>.
- (30) Bhattacharjee, S.; Chaudhary, S. P.; Bhattacharyya, S. Lead-Free Metal Halide Perovskite Nanocrystals for Photocatalysis in Water. 2019. <https://doi.org/10.26434/chemrxiv.9794270.v1>.

# HIGH PRESSURE STUDIES

Speaking about hybrid metal halide perovskites, while studies of temperature dependence ordering and hydrogen bonding of the organic cations exist, the knowledge of pressure-induced effects on hybrid perovskites and specifically on the organic-inorganic interaction and its structure remains scarce<sup>98</sup>.

Understanding correlations between pressure-induced structural and electronic changes can allow us to more precisely tune material properties through compression<sup>99</sup>. Pressures on the gigapascal scale affect a wide variety of transformations in the structural<sup>100,101</sup>, optical<sup>102</sup>, magnetic<sup>103,104</sup>, and electronic transport<sup>105,106</sup> properties of organic and inorganic solids. Furthermore, the compressibility of well-defined organic-inorganic hybrids can be modulated by fine-tuning both organic and inorganic components. In this regard, the effects of compression on crystalline hybrid perovskites are a subject of great interest<sup>107</sup>.

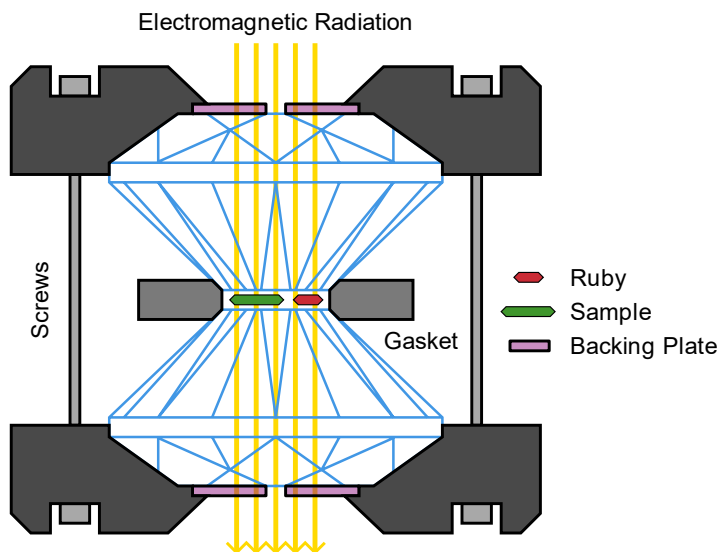


*Figure 3.1* Scheme of a Diamond Anvil Cell (DAC); This is the most diffuse equipment employed to carry on HP studies. Image by Tobias1984 (This W3C-unspecified vector image was created with Inkscape, CC BY-SA 3.0, <https://commons.wikimedia.org/w/index.php?curid=19419201>)

The high-pressure (HP) studies are usually carried on by the means of different apparatuses and the most common is the Diamond Anvil Cell (DAC; see Figure 3.1).

The HP investigation of hybrid perovskites is relatively recent and mainly focused on methylammonium lead iodide hybrid perovskite ( $\text{MAPbI}_3$ ). The research carried out on hybrid perovskites has clearly shown that a significant volume of compression activates a complex phenomenology involving both electronic and structural properties<sup>98</sup>.

High pressure can modify bond lengths and valence angles in hybrid perovskites without chemical interference, finely tuning the electronic structure responsible for basic properties of photovoltaic materials, like the energy gap and carrier diffusion length<sup>108</sup>. In response to pressure, the inorganic framework is

modified by the contraction of B–X bonds or/and bending of B–X–B bridges coupled with  $BX_6$  octahedra tilting. Generally, the shortening of bonds B–X narrows the bandgap, whereas it is widened by the B–X–B angle bending<sup>109,110</sup>. However, the resultant bandgap change depends on the contributions of these competitive structural pressure effects<sup>108</sup>.



*Figure 3.2* Example of industrial Spark Plasma Sintering (SPS) equipment; SPS is one of the most employed industrial techniques for sintering.

Anyway, all-inorganic metal halide perovskites HP studies are not lacking in interesting aspects and applications too. In fact,

these studies could permit to discover new phases or materials that could be subsequently synthesized on a large scale. Indeed, high-pressure synthesis on an industrial scale (an example is shown in Figure 3.2) is already applied to obtain synthetic diamonds and cubic boron nitride (c-BN), which are the super-hard abrasives of choice for cutting and shaping hard metals and ceramics<sup>111</sup>. Recently, high-pressure science has undergone a renaissance, with novel techniques and instrumentation permitting entirely new classes of high-pressure experiments<sup>111</sup>, that could therefore involve metal halide perovskites too.



### 3.1 $\text{MASnBr}_3$ and $\text{CsSnBr}_3$

#### **Band Gap Engineering in $\text{MASnBr}_3$ and $\text{CsSnBr}_3$ Perovskites: Mechanistic Insights through the Application of Pressure**

##### *Purpose and scope*

Here we reported on the first structural and optical high-pressure investigation of  $\text{MASnBr}_3$  ( $\text{MA}=[\text{CH}_3\text{NH}_3]^+$ ) and  $\text{CsSnBr}_3$  halide perovskites. Therefore, we obtained useful and new information about both hybrid and fully inorganic lead-free halide perovskites.

##### *Introduction*

The application of an external pressure is a fascinating and powerful tool to manipulate the crystal and electronic structure of any material and has shown great potential for the engineering of photovoltaic (PV) perovskites.<sup>1-5</sup> The interest of high-pressure (HP) research on PV materials is manifold: i) understand the basic phenomena occurring during hydrostatic/non-hydrostatic compression; ii) discover new behavior induced by HP; iii) stabilize new metastable phases; and iv) try to reproduce the in situ pressure effects by chemical-pressure and/or the strain induced by a substrate on thin films.<sup>1-</sup>

<sup>5</sup> Starting from the first HP studies on  $\text{ABX}_3$  three-dimensional hybrid perovskites, other systems have been investigated, namely double perovskites, zero-dimensional (0D) perovskites quantum dots or nanocrystals, and layered two-dimensional (2D) perovskites.<sup>3</sup>

The most relevant interest in these HP studies, together with the definition of the structural evolution with pressure, is the modulation, or engineering, of the optical bandgap ( $E_g$ ). With reference to 3D perovskites, where the most investigated systems have been MAPbX<sub>3</sub> compounds together with FAPbI<sub>3</sub>, FAPbBr<sub>3</sub> and CsPbBr<sub>3</sub>, some common HP features of  $E_g$  have been observed.<sup>6-17</sup> In particular, the bandgap is first red-shifted with P, followed by a blue-shift, which is usually connected to a structural phase transition to a more distorted crystal structure, if found, within few GPa.<sup>2</sup> The proposed mechanism for this trend is well-accepted and considers the first red-shift deriving from a shortening of Pb-X bond length, resulting in increased orbital coupling, while the following blue-shift arises from local strains generated in the distorted crystal structure, connected with the bending of the Pb-X-Pb bond angles, thus reducing the orbital coupling.<sup>5</sup> This scenario has been developed based on the significant number of papers published on pressure-induced effects on Pb-based perovskites for photovoltaics. However, due to the key role of the perovskite B-atom through its orbital contribution, it is clear that an extension to other systems with different metals should be provided in order to further understand the level of material properties tunability by substituting the metal atom at the B-site. Moreover, the basic idea of HP studies is to highlight the effect of structural modifications on the bandgap, with the aim of engineering them in chemical systems at ambient conditions, apart from investigating the crucially important effects of strains. The search for such effects on lead-free environmental-friendly systems is urgent.

As it is well known in the field of PV perovskites, Sn is a natural alternative to Pb. Recently there has been increasing interest toward Sn-based fully inorganic and hybrid perovskites, and an improvement in the PV performance and stability has been

achieved.<sup>18,19</sup> Concerning HP studies, only few Sn-based 3D hybrid perovskite systems have been investigated so far, none of them including Br.<sup>20-22</sup>

In view of the above reported considerations, in this paper we present the results of a high-pressure structural and optical properties investigation on CsSnBr<sub>3</sub> and MASnBr<sub>3</sub> perovskites carried out in diamond anvil cell (DAC). The choice of these two systems results from the fact that, recently, CsSnBr<sub>3</sub> showed an impressive tolerance towards aging and moisture stability.<sup>23</sup> This suggests that any pressure-induced phenomena could be ideally extended to highly stable Sn(II)-based systems. Moreover, the study of MASnBr<sub>3</sub>, and the comparison of the behavior between these two systems, sharing the same metal and halogen as well as the same crystal structure at ambient pressure (Pm-3m space group), could shed some light on the role of A-site cation (organic or inorganic) on the HP behavior of 3D perovskites, which, based on the available data on Pb-based systems, seems to be dominated by the B-site atom-halogen interaction alone. Finally, the comparison with the Pb-based analogue perovskites, namely CsPbBr<sub>3</sub> and MAPbBr<sub>3</sub>, will shed light on the role of the B-site metal on the pressure-induced effects.<sup>1,16</sup>

### Experimental methods

**Perovskites syntheses.** The MASnBr<sub>3</sub> bulky powder has been synthesized in nitrogen flux by dissolving tin (II) acetate in a large excess of HBr acid up to 100 °C, adding a stoichiometric quantity of methylamine, cooling to c.ca 60 °C, filtering by the means of a water pump, and drying the product in vacuum into a glass oven at 60 °C for one night.

The CsSnBr<sub>3</sub> bulky powder has been obtained by grinding stoichiometric amounts of CsBr and SnBr<sub>2</sub> with a ball miller equipment (Pulverisette 7, Fritsch). The mechanochemical reaction has been carried out employing tungsten carbide jars and spheres with a weight ratio between materials and balls of 1 : 10 and maintaining a speed of 400 rpm for 12 cycles (10 minutes of pause for every 20 minutes of grinding).

Then the experiment took place at ESRF (European Synchrotron Radiation Facility) ID-15B beamline.

**XRD.** Single crystal X-ray diffraction measurements have been carried out up to 9 GPa by the means of a Diamond Anvil Cell (DAC) filled with helium as pressure transmitting medium. The crystals have been manually selected from the powders by the beamline local contact.

**PL and Abs.** Photoluminescence and optical absorbance spectra have been collected in situ with the beamline equipment. The high-pressure PL spectra and the bandgap were extracted from absorption spectroscopy up to 3 GPa.

**DFT calculations.** Bandgap values have been obtained by Density Functional Theory calculations too.

### Results and discussion

The crystal structure up to 9 GPa was investigated in situ single crystal X-ray diffraction (XRD) in a DAC cell with helium as pressure transmitting medium. Figure 3.3 reports some selected integrated XRD patterns for CsSnBr<sub>3</sub> and MASnBr<sub>3</sub>.

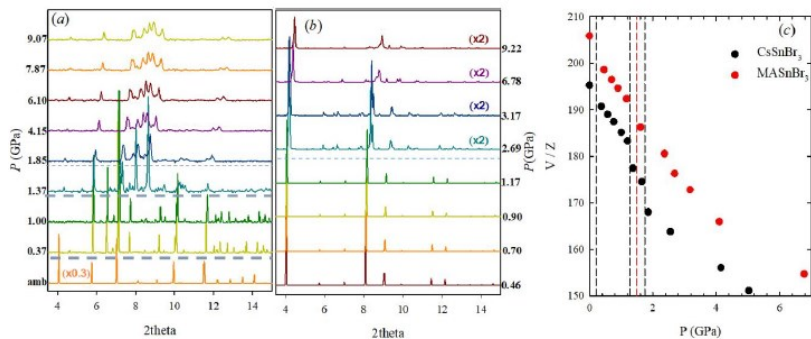


Figure 3.3 Selected integrated XRD patterns ( $\lambda = 0.400 \text{ \AA}$ ) as a function of pressure (reported in GPa on the side) upon compression for (a) CsSnBr<sub>3</sub> and (b) MASnBr<sub>3</sub>. (c) Formula-unit volume as a function of pressure for CsSnBr<sub>3</sub> (black) and MASnBr<sub>3</sub> (red). Dashed lines highlight phase transitions.

At ambient conditions CsSnBr<sub>3</sub> is cubic (space group Pm-3m) and is reported to exhibit three successive low-temperature phase transformations at 292, 274 and 247 K.<sup>24</sup> We observed that CsSnBr<sub>3</sub> transforms already at 0.37 GPa into the tetragonal phase with a primitive unit cell and lattice parameters  $a = b = \sqrt{2}a_c$  and  $c = 2a_c$ , where  $a_c$  refers to the cubic unit cell. Consistent with previous low-temperature investigations, the pressure-induced phase has space group P4/mbm and involves the in-phase rotation of the SnBr<sub>6</sub> octahedra about the  $c$  axis corresponding to an  $a^0a^0c^+$  tilt.<sup>24,25</sup> This phase is isostructural to the high-temperature phase II of CsPbBr<sub>3</sub>.<sup>26</sup> Another phase transformation occurs above 1.2 GPa, leading to a monoclinic phase with metric  $3a_c \cdot 2a_c \cdot 4a_c$ . At  $\sim 1.8$  GPa the crystal undergoes a further transition to a more disordered phase, evidenced by a sudden broadening of reflections. As shown in Figure 3.3c, continuous lattice contraction is observed at HP, with no clear evidence of amorphization. The primitive cubic phase is fully restored after decompression.

The other system investigated (Figure 3.3b), MASnBr<sub>3</sub>, shows a single transition at  $\sim 1.5$  GPa from the cubic ambient-pressure

phase (Pm-3m space group) to an orthorhombic phase ( $2\sqrt{2}a_c \cdot 2\sqrt{2}a_c \cdot 2a_c$ ), which is observed up to 9.0 GPa. Again, the cubic phase is restored upon decompression.

Compared to the analogous lead-based perovskites, the structural HP behavior of CsSnBr<sub>3</sub> and MASnBr<sub>3</sub> is different. Before the pressure-induced amorphization, the MAPbBr<sub>3</sub> ambient pressure phase of cubic space group Pm-3m transforms at 0.75 GPa to another cubic phase of space group Im-3 ( $2a \cdot 2a \cdot 2a$ ), and above 2 GPa to another lower-symmetry phase, probably orthorhombic of space group Pnma ( $a \cdot \sqrt{2}a \cdot a$ ). The cubic and orthorhombic phases coexist in the pressure range 2.1 – 2.7 GPa.<sup>1</sup> A similar evolution upon pressure is observed for other halide perovskites, where the orthorhombic phase is realized either with a doubling of the cubic lattice parameter, leading to the space group Immm for MASnI<sub>3</sub>, or with two parameters along the cubic base diagonals and space group Pnma, as observed for FAPbBr<sub>3</sub>.<sup>17</sup> The CsPbBr<sub>3</sub> crystal is of orthorhombic space group Pnma at ambient pressure and shows no change of space group until the onset of amorphization at about 2 GPa, but an isostructural transition was postulated around 1 GPa to reconcile the pressure-induced changes in the absorption edge.<sup>16</sup>

The sequence of HP phases does not match those at low temperature. As a matter of fact, by lowering T, MASnBr<sub>3</sub> transforms to a simpler orthorhombic phase ( $\sqrt{2}a_c \cdot \sqrt{2}a_c \cdot a_c$ ), which cannot account for all reflections observed here.<sup>27</sup> Swainson et al. found also a further transformation to a triclinic phase, not observed here. As to CsSnBr<sub>3</sub>, after the transformation to tetragonal P4/mbm, the lower-temperature form is orthorhombic Pnma rather than monoclinic as observed here.<sup>24</sup> Hence, some of the high-pressure phases of CsSnBr<sub>3</sub> and

MASnBr<sub>3</sub> do not correspond to structure reported so far for hybrid perovskites.

Another peculiarity of CsSnBr<sub>3</sub> and MASnBr<sub>3</sub> is their resistance against amorphization. MASnBr<sub>3</sub> is fully crystalline up to 9.2 GPa. The XRD patterns of CsSnBr<sub>3</sub> above 2 GPa become broad. However, sharp single crystal spots are still observed up to 9.1 GPa with no evidence of amorphous-like background. This suggests a sort of microstrain effect, with a wide distribution of lattice parameters rather than amorphization. Another possible explanation is the occurrence of different competing phases, as observed on coesite, which led a similar high pressure broadening.<sup>28</sup>

On the other hand, the equivalent Pb-based compounds of the present work, i.e. CsPbBr<sub>3</sub> and MAPbBr<sub>3</sub>, show a clear evidence of amorphization starting from ~2 GPa.<sup>1,16</sup> The occurrence of amorphization is nowadays considered as a driving force for the blue-shifted bandgap observed with pressure.

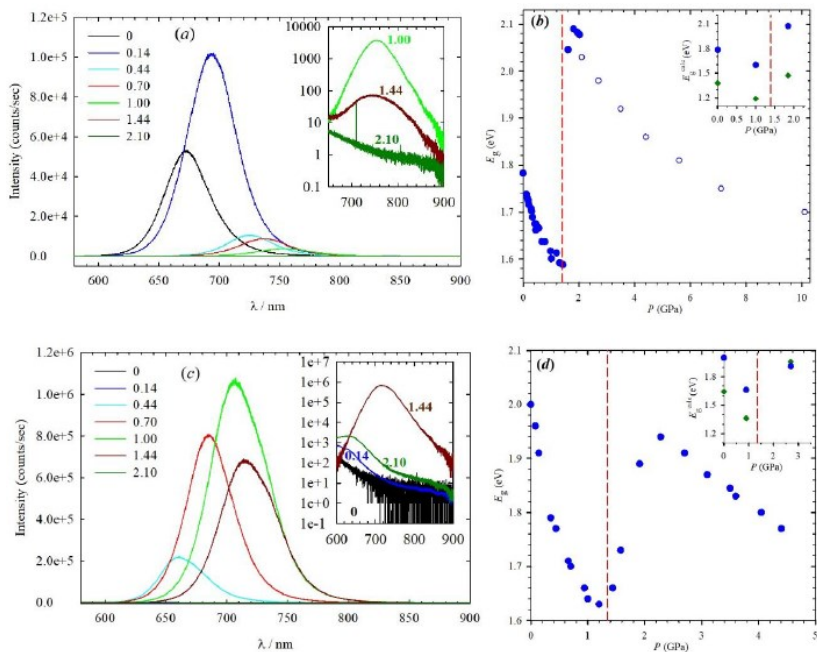


Figure 3.4 a) PL spectra and b) trend of optical bandgap vs. pressure for CsSnBr<sub>3</sub>; the vertical dashed line marks the tetragonal to monoclinic transition; as a pressure medium dafne oil was used to ~2 GPa (blue circles) and argon at higher pressures (empty circles). c) PL spectra and d) trend of optical bandgap vs. pressure for MASnBr<sub>3</sub>. The vertical dashed line in (d) marks the region of the cubic to orthorhombic phase transition. The insets report in green the bandgap values determined ab-initio, compared to experimental values in blue.

The optical properties under pressure have been measured by photoluminescence (PL) and optical absorbance spectroscopy. The high-pressure PL spectra and the bandgap extracted from absorption spectroscopy up to 3 GPa for CsSnBr<sub>3</sub> are reported in Figure 3.4-a and 3.4-b, respectively. The PL of CsSnBr<sub>3</sub> shows a strong signal at ambient pressure at about 670 nm, in agreement with available data.<sup>23</sup> This signal red-shifts and increases in intensity with slight application of pressure (0.14 GPa), then diminishes rapidly with no noticeable signal above



~1.4 GPa (see the inset, logarithmic scale). Notably, this is the pressure around which we found the tetragonal to monoclinic phase transition. The red-shift evidenced by PL is confirmed by absorption spectroscopy (Figure 3.4-b) where a progressive reduction of the bandgap energy is found up to the tetragonal to monoclinic phase transition, here observed at ~1.45 GPa. This behavior has been observed also in CsPbBr<sub>3</sub> up to the orthorhombic to orthorhombic transition occurring at about 1.2 GPa.<sup>16</sup> One remarkable difference between the two systems, however, is the magnitude of the red-shift. As observed in Figure 3.4-b, the overall variation of  $E_g$  from ambient pressure to the phase transition is close to 0.2 eV. In the analogous Pb-based material, the variation is of the order of 0.03 eV<sup>16</sup>; similar red-shifts were observed only in 2D perovskites, not before the application of 4-5 GPa<sup>29,30</sup>. Following the first red-shift, CsSnBr<sub>3</sub> has a sudden and impressive blue-shift of ~0.5 eV (Figure 3.4-b). Such a jump in the optical behavior of any fully inorganic or hybrid halide 3D perovskite has never been observed. Usually, there is a smooth upturn from a red-shift to a blue-shift occurring at a structural change, which is a very general trend irrespective to the crystallographic nature of the two phases involved,<sup>1-5</sup> even though nanostructuring might increase the magnitude of the blue-shift.<sup>31-32</sup> When entering the monoclinic phase above about 1.5 GPa, the bandgap has a slight further blue-shift up to the existence of a well-defined crystal structure (~3 GPa, see XRD data). Above this pressure, the material does not become amorphous, but a significant broadening of the diffraction peaks is found. In this HP regime, the bandgap red-shifts progressively up to the highest pressure we could measure (~10 GPa). Such a trend, even though to lesser extent, has been observed in MAPbI<sub>3</sub>, where a continuous reduction of the bandgap up to (eventually) a metallic state has been observed by conductivity measurements up to 60 GPa.<sup>33</sup>

The HP behavior of the optical properties of  $\text{MASnBr}_3$  are reported in Figure 3.4-c and 3.4-d. At ambient pressure, the sample shows weak PL signal with a broad peak near 580 nm, together with a Raman contribution. With increasing pressure, the PL signal redshifts and increases drastically in intensity up to 1.4 GPa. At  $\sim 2$  GPa, the PL signal blueshifts and diminishes in intensity with increasing pressure. The trend of the bandgap versus P (Figure 3.4-d) confirms the one of PL and extends it up to higher pressures. The upturn in the bandgap above  $\sim 1.5$  GPa is concomitant to the cubic to orthorhombic structural phase transition observed with XRD. Again, the variation of the bandgap in the region before the phase transition is huge compared to the Pb-based analogue. For  $\text{MASnBr}_3$  the change is from  $\sim 2.0$  eV (ambient pressure) to  $\sim 1.6$  eV (last before the phase transition), i.e. of  $\sim 0.4$  eV. On the other hand, the  $\text{MAPbBr}_3$  system, which is also primitive cubic at ambient pressure, shows overall red-shift of  $\sim 0.04$  eV within the ambient phase, while a progressive blue-shift of about 0.15 eV from 1 GPa to 3 GPa after the cubic to cubic phase transition.<sup>1</sup> We highlight that  $\text{MAPbBr}_3$  shows strong amorphization already at about 3 GPa, while  $\text{MASnBr}_3$ , after the blue-shift jump (of  $\sim 0.3$  eV) at the structural phase transition, shows a continuous red-shift of the bandgap while retaining the orthorhombic crystal structure without detectable amorphization.

To summarize,  $\text{MASnBr}_3$  and  $\text{CsSnBr}_3$  share a common trend of optical properties as a function of pressure: i) a huge red-shift of the bandgap in the region before a phase transition, of the order of 0.2-0.4 eV; ii) an abrupt blue-shift jump at the phase transition of the order of 0.3-0.5 eV; and iii) a further red-shift at higher pressures; iv) no appreciable amorphization up to 9 GPa.

Such an anomalous bandgap evolution with pressure was investigated by Density functional theory (DFT) calculations, comparing Sn- based perovskites to the analogous containing

Pb. For each system, we optimized the structure at ambient pressure and at the pressure with the lowest and the highest bandgap. The bandgap evolution matches nicely with the experimental trends (see insets in Figure 3.4-b and 3.4-d), showing a lowering of bandgap with increasing pressure as long as the ambient pressure phase is maintained; followed by a sudden increase of bandgap with pressure, associated to a structure change. The lower absolute bandgap in DFT compared to the experiment is due to the sizable structural flexibility of this kind of materials. The instantaneous structure could significantly differ from the time scale and experimental XRD structures (i.e. thermal averaged structure). In fact, the dynamic disorder of the A cation is not decoupled from inorganic lattice and has important consequences on the electronic properties.<sup>34</sup> Since the motivation of this work is to understand the bandgap evolution under pressure, the matching of absolute values of bandgap with experiment is not worthy to consider.

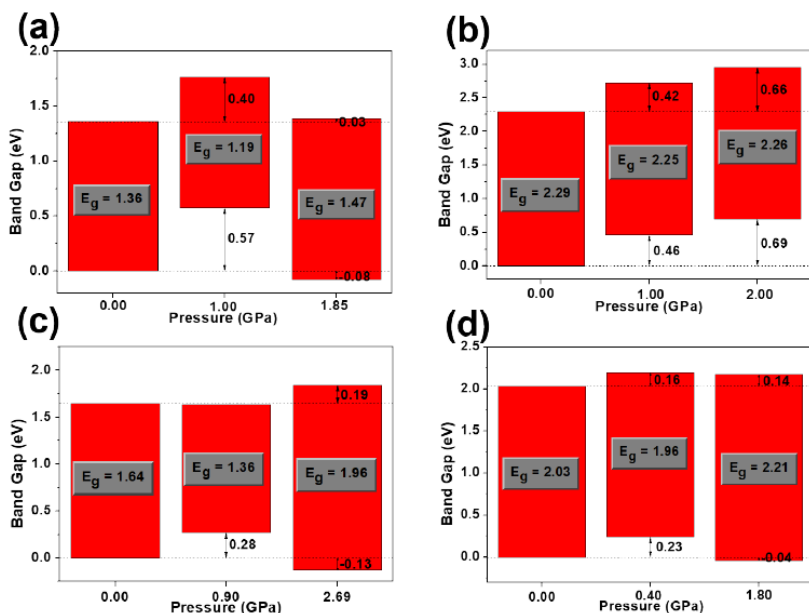


Figure 3.5 Alignment of band edges under different pressure for (a) CsSnBr<sub>3</sub>, (b) CsPbBr<sub>3</sub>, (c) MASnBr<sub>3</sub> and (d) MAPbBr<sub>3</sub>

To gain more insight into the shifting of band edges with pressure, we aligned the density of states (DOS) as shown in Figure 3.5. The valence band maxima (VBM) of ABX<sub>3</sub>-type halide perovskites derive from the antibonding hybrid state of the metal *s* and halide *p* orbitals, whereas the conduction band minimum (CBM) is a hybrid of metal *p* and halide *p* orbitals with less antibonding and more nonbonding character.<sup>35,36</sup>

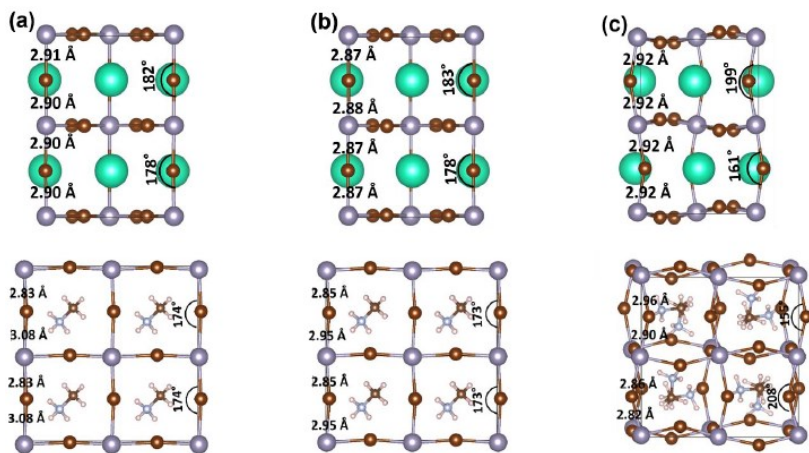


Figure 3.6 Optimized structures from DFT of CsSnBr<sub>3</sub> (top) and MASnBr<sub>3</sub> (bottom) at (a) ambient (b) 1.00 GPa and (c) 1.85 GPa.

With increasing pressure, the metal-halide bond length decreases (Figure 3.6-a,b) and the overlap between metal and halide increases, concomitantly destabilizing the VB. The CB, on the other hand, derives from metal p and halide p orbitals and having less orbital overlap, responds to a lesser extent than the VB. Both the Pb- and Sn-perovskites follow this trend irrespective of the A cation (see first two columns of Figure 3.5). A further increase of pressure induces the tilting of the metal-halide bond (Figure 3.6-c) concomitant with the phase transformations. The tilting has more impact on the HP behavior of Sn- than Pb-perovskites. Indeed, in the HP region, the VB of Sn-perovskites gets more stabilized compared to Pb-perovskites. As shown in the right panels of Figure 3.5, the VB is stabilized by 0.65 (from 0.57 to -0.08 eV) and 0.41 (from 0.28 to -0.13 eV) eV for CsSnBr<sub>3</sub> and MASnBr<sub>3</sub>, respectively. On the other hand, only 0.27 eV stabilization is obtained for MAPbBr<sub>3</sub> while CsPbBr<sub>3</sub> is even destabilized. This calls for a careful inspection

of the structural and electronic behavior of Pb and Sn-perovskites to understand the origin of this contrasting effect. Let us first consider CsSnBr<sub>3</sub>. The axial Sn-Br bond length is 2.90 Å at ambient pressure, it shortens to 2.87 Å at 1.00 GPa and, surprisingly, increases to 2.92 Å by further increasing pressure to 1.85 GPa. Therefore, while moving from cubic to tilted geometry, the Sn-Br bond length increases, thus reducing the Sn-Br overlap and promoting the shifting (by 0.65 eV) of VB towards lower energies. Notably, also the CB gets stabilized, but only to a lesser extent (0.37 eV). In fact, the stabilization is driven by spin orbit coupling (SOC) only, since the non-bonding metal p orbitals character is less influenced by distortion.

The picture gets clearer by considering the Sn content around the CB, which decreases up to 1.00 GPa followed by an increase up to 1.85 GPa. Because SOC is mainly associated with the heavy Sn centers, it is enhanced by an increase of Sn character. The variable amount of Sn character in the DOS with the tilt angle can be associated with the overlap extent in Sn-Br bonds, which decreases upon octahedral tilting, thus inducing effective increase of the Sn content up to 5 % at the CBM in CsSnBr<sub>3</sub>. The behavior is marginal at the VB since the SOC contribution of Sn is limited. However, to quantify further the role of tilting towards the bandgap, we considered the case of non-tilted geometry maintained at high pressure. This led to axial Sn-Br bond distance of 2.88 Å with bandgap of 1.12 eV. Therefore, the observed blue-shift cannot be obtained without producing a tilted phase with longer Sn-Br bond distance, which revealed unusual bandgap evolution at high-pressure.

As to the analogous Pb compound, CsPbBr<sub>3</sub>, the structure remains orthorhombic from ambient pressure throughout the pressure range,<sup>37</sup> showing a contraction of the Pb-Br bond length upon pressure, which gradually shifts the VB to higher energies. Similarly, the linear decrease of Pb content at the CBM

destabilizes the CM, thus neutralizing the shift of band edges from the two ends.

As observed for  $\text{CsSnBr}_3$ , also  $\text{MASnBr}_3$  exhibits bandgap reduction under moderate pressure, from 1.64 eV at ambient to 1.36 eV at 0.90 GPa. The bandgap becomes higher (1.96 eV) at 2.69 GPa after the cubic to orthorhombic phase transition. Notably, the Sn-Br bond distance of pristine  $\text{MASnBr}_3$  shows an alternating short/long nature of 2.83-3.08 Å. However, bond distances possess a typical dynamical average with shorter time step as shown for  $\text{FASnBr}_3$ .<sup>38</sup> The short/long nature tends to gradually equalize already at 0.90 GPa (2.85 and 2.95 Å) and at 2.69 GPa (2.86 and 2.91 Å). Therefore, the destabilization of VB under 0.90 GPa is understandable from the increase of overlap between Sn-Br bonds, similarly to  $\text{CsSnBr}_3$ . However, at 2.69 GPa the CB shifts to higher energy, a behavior not observed for  $\text{CsSnBr}_3$ . This means that the tilting and/or the bond length play a limited role towards the Sn contribution at CB. On the other hand, the cation orientation, which is significantly different in the pseudocubic lattice, plays the dominant role towards upshifting the CB by the virtue of hydrogen bonding<sup>39</sup> and Rashba/Dresselhaus effect,<sup>40</sup> which mainly influence the CB.<sup>41</sup> Eventually,  $\text{MAPbBr}_3$  follows a similar trend as  $\text{MASnBr}_3$ , but smaller in magnitude. This is due to the small difference in short-long nature of the Pb-Br bond (2.95 and 3.04 Å) compared to Sn-Br (2.83 and 3.08 Å) together with the prominent SOC effect of Pb compared to Sn. Hence, although the bandgap evolution with pressure for both  $\text{CsSnBr}_3$  and  $\text{MASnBr}_3$  perovskites is similar, the underlying structural mechanisms are different. The bandgap evolution depends on three competing parameters of structural alternations: bond length shortening, octahedral tilting and cation displacement. All of these three structural alternations occur in parallel, however, one dominates over another depending on the system. In a relatively low-pressure

domain, the main parameter is bond length shortening, whereas at higher pressure, octahedral tilting and cation displacement start to play an important role, having organic cation predominant role in hybrid perovskites compared to inorganic perovskites.

### Conclusions

To summarize, we reported on the first structural and optical HP investigation of  $\text{MASnBr}_3$  and  $\text{CsSnBr}_3$  halide perovskites up to  $\sim 10$  GPa by using a diamond anvil cell and in hydrostatic conditions. A massive red-shift of 0.4 eV for  $\text{MASnBr}_3$  and 0.2 eV for  $\text{CsSnBr}_3$  is observed from absorption spectroscopy within 1.3-1.5 GPa, followed by an important blue-shift of 0.3 and 0.5 eV. Further increase of pressure leads to a progressive red-shift. Whereas qualitatively this pressure-trend is common to other (mostly Pb-based) hybrid perovskites, the magnitude of red and blue-shifts is unprecedented among 3D perovskites for PV applications. The red-shift is confirmed also from PL spectra with the PL signal of  $\text{MASnBr}_3$  which is enhanced at moderate pressure, but vanishes at  $\sim 1.5$  GPa concomitantly with the blue-shift. Similarly, the PL signal of  $\text{CsSnBr}_3$  dies out in the same pressure range. The structure evolution with pressure was investigated by synchrotron HP single crystal diffraction. Both  $\text{CsSnBr}_3$  and  $\text{MASnBr}_3$  are cubic at ambient conditions. The upturn in optical properties (onset of blue-shift and PL decay) is consistent with structural changes, namely from cubic to orthorhombic ( $\sim 1.5$  GPa) in  $\text{MASnBr}_3$  and from tetragonal to monoclinic ( $\sim 1.3$  GPa) in  $\text{CsSnBr}_3$ . The  $\text{CsSnBr}_3$  crystal exhibits two further transformations: cubic to tetragonal below 0.4 GPa and an isostructural transformation at  $\sim 1.8$  GPa towards a more disordered state. The rule of reverse pressure and temperature



effects does not hold for these compounds and the HP crystal phases are different than those reported at low-temperature.  $\text{CsSnBr}_3$  and  $\text{MASnBr}_3$  are resistant to amorphization, which in other hybrid perovskites generally develops from  $\sim 2$  GPa. The structures obtained from XRD were employed as starting point for DFT calculations, aimed at explaining the origin of the peculiar bandgap evolution with pressure. DFT calculations allowed to describe the bandgap evolution as a competition of local structure deformations, such as bond length shortening, octahedral tilting and cation displacement. Although both  $\text{CsSnBr}_3$  and  $\text{MASnBr}_3$  perovskites show similar bandgap evolution with pressure, the underlying mechanisms are different.  $\text{CsSnBr}_3$  bandgap is controlled by the Sn-Br bond-length, which contracts with pressure thus enhancing orbital overlapping with consequent red-shift. Surprisingly, the structural distortion accompanying the phase transformation at  $\sim 1.3$  GPa promotes the lengthening of the Sn-Br length, thus reducing the overlap, giving rise to massive blue-shift. This applies to  $\text{MASnBr}_3$  only during red-shift, i.e. within the stability range of the cubic phase. By further increasing pressure, the orientational disorder of the organic cation together with the consequent H-bonding takes over the Sn-Br bond length to control the electronic properties. This promotes the increase of the CB energy across the cubic to orthorhombic transformation, resulting in a blue-shift.

Our study shows that the application of external pressure is a powerful tool for tuning the electronic properties of halide perovskites and, in this respect,  $\text{CsSnBr}_3$  and  $\text{MASnBr}_3$  proves to be particularly suitable candidates, as their response to external pressure is unprecedented. They are also an environment-friendly alternative to Pb-compounds, thus paving the way for the design of new materials exploring pressure-induced band-gap tuning.

## References

- (1) Szafranski, M.; Katrusiak, A. Photovoltaic Hybrid Perovskites under Pressure. *J. Phys. Chem. Lett.* 2017, 8, 2496–2506.
- (2) Postorino, P.; Malavasi, L. Pressure-Induced Effects in Organic–Inorganic Hybrid Perovskites. *J. Phys. Chem. Lett.* 2017, 8, 2613–2622.
- (3) Liu G.; Kong, L.; Yang, W.; Mao, Ho-W. Pressure Engineering of Photovoltaic Perovskites. *Materials Today* 2019, 27, 91-106.
- (4) Jaffe, A.; Lin, Y.; Karunadasa, H. I. Halide Perovskites Under Pressure: Accessing New Properties through Lattice Compression. *ACS Energy. Lett.* 2017, 2, 1549-1555.
- (5) Lu, X.; Yang, W.; Jia, Q.; Xu, H. Pressure-induced Dramatic Changes in Organic- Inorganic Halide Perovskites. *Chem. Sci.* 2017, 8, 6764-6776.
- (6) Wang, K.; Liu, R.; Qiao, Y.; Cui, J.; Song, B.; Liu, B.; Zou, B. Pressure-Induced Reversible Phase Transition and Amorphization of  $\text{CH}_3\text{NH}_3\text{PbI}_3$ . arXiv:1509.03717, 2015.
- (7) Ou, T.; Yan, J.; Xiao, C.; Shen, W.; Liu, C.; Liu, X.; Han, Y.; Ma, Y.; Gao, C. Visible Light Response, Electrical Transport, and Amorphization in Compressed Organolead Iodine Perovskites. *Nanoscale* 2016, 8, 11426–11431.
- (8) Jaffe, A.; Lin, Y.; Beavers, C. M.; Voss, J.; Mao, W. L.; Karunadasa, H. I. High- Pressure Single-Crystal Structures of 3D Lead-Halide Hybrid Perovskites and Pressure Effects on their Electronic and Optical Properties. *ACS Cent. Sci.* 2016, 2, 201–209.
- (9) Jiang, S.; Fang, Y.; Li, R.; Xiao, H.; Crowley, J.; Wang, C.; White, T. J.; Goddard, W. A., III; Wang, Z.; Baikie, T.; et al. Pressure-Dependent Polymorphism and

Band-Gap Tuning of Methylammonium Lead Iodide Perovskite. *Angew. Chem., Int. Ed.* 2016, 55, 6540–6544.

(10) Capitani, F.; Marini, C.; Caramazza, S.; Postorino, P.; Garbarino, G.; Hanfland, M.; Pisanu, A.; Quadrelli, P.; Malavasi, L. High-Pressure Behavior of Methylammonium Lead Iodide (MAPbI<sub>3</sub>) Hybrid Perovskite. *J. Appl. Phys.* 2016, 119, 185901.

(11) Szafranski, M.; Katrusiak, A. Mechanism of Pressure-induced Phase Transitions, Amorphization, and Absorption-Edge Shift in Photovoltaic Methylammonium Lead Iodide, *J. Phys. Chem. Lett.* 2016, 7, 3458-3466.

(12) Swainson, I.P.; Tucker, M.G.; Wilson, D.J.; Winkler B.; Milman, V. Pressure Response of an Organic-inorganic Perovskite: Methylammonium Lead Bromide, *Chem. Mater.* 2007, 19, 2401-2405.

(13) Wang, Y.; Lu, X.; Yang, W.; Wen, T.; Yang, L.; Ren, X.; Wang, L.; Lin, Z.; Zhao, Y. Pressure-Induced Phase Transformation, Reversible Amorphization and Anomalous Visible Light Response in Organolead Bromide Perovskite. *J. Am. Chem. Soc.* 2015, 137, 11144–11149.

(14) Wang, L.; Wang, K.; Xiao, G.; Zeng, Q.; Zou B. Pressure-Induced Structural Evolution and Band Gap Shifts of Organometal Halide Perovskite-Based Methylammonium Lead Chloride. *J. Phys. Chem. Lett.* 2016, 7, 5273-5279.

(15) Wang, P.; Guan, J.; Galeschuk, T.K.; Yao, Y.; He, C.F.; Jiang, S.; Zhang, S.; Liu, Y.; Jin, M.; Kin, C.; Song, Y. Pressure-Induced Polymorphic, Optical, and Electronic Transitions of Formamidinium Lead Iodide Perovskite, *J. Phys. Chem. Lett.* 2017, 8, 2119-2125.

(16) Zhang, L.; Zeng, Q.; Wang, K. Pressure-Induced Structural and Optical Properties of Inorganic Halide Perovskite CsPbBr<sub>3</sub>. *J. Phys. Chem. Lett.* 2017, 8, 3752–3758.

- (17) Wang, L.; Wang, K.; Zou, B. Pressure-Induced Structural and Optical Properties of Organometal Halide Perovskite-Based Formamidinium Lead Bromide. *J. Phys. Chem. Lett.* 2016, 7, 2556-2562.
- (18) Song, T.-B.; Yokoyama, T.; Aramaki, S.; Kanatzidis, M. G. Performance Enhancement of Lead-Free Tin-Based Perovskite Solar Cells with Reducing Atmosphere-Assisted Dispersible Additive. *ACS Energy Lett.* 2017, 2, 897-903.
- (19) Gupta, S.; Bendikov, T.; Hodes, G.; Cahen, D. CsSnBr<sub>3</sub>, A Lead-Free Halide Perovskite for Long-Term Solar Cell Application: Insights on SnF<sub>2</sub> Addition. *ACS Energy Lett.* 2016, 1, 1028-1033.
- (20) Lu, X.; Wang, Y.; Stoumpos, C. C.; Hu, Q.; Guo, X.; Chen, H.; Yang, L.; Smith, J. S.; Yang, W.; Zhao, Y.; Xu, H.; Kanatzidis, M. G.; Jia, Q. Enhanced Structural Stability and Photo Responsiveness of CH<sub>3</sub>NH<sub>3</sub>SnI<sub>3</sub> Perovskite via Pressure-Induced Amorphization and Recrystallization. *Adv. Mater.* 2016, 28, 8663-8668.
- (21) Wang, L.; Ou, T.; Wang, K.; Xiao, G.; Gao, C.; Zou, B. Pressure-Induced Structural Evolution, Optical and Electronic Transitions of Nontoxic Organometal Halide Perovskite-Based Methylammonium Tin Chloride. *Appl. Phys. Lett.* 2017, 111, 233901.
- (22) Lee, Y.; Mitzi, D. B.; Barnes, P. W.; Vogt, T. Pressure-induced Phase Transitions and Templating Effect in Three-dimensional Organic-inorganic Hybrid Perovskites. *Phys. Rev. B.* 2003, 68, 020103(R).
- (23) Bernasconi, A.; Rizzo, A.; Listorti, A.; Mahata, A.; Mosconi, E.; De Angelis, F.; Malavasi, L. Synthesis, Properties, and Modeling of Cs<sub>1-x</sub>Rb<sub>x</sub>SnBr<sub>3</sub> Solid Solution: A New Mixed-Cation Lead-Free All-Inorganic Perovskite System. *Chem. Mater.* 2019, 31, 3527-3533.

- (24) D. H. Fabini, G. Laurita, J. S. Bechtel, C. C. Stoumpos, H.A. Evans, A. G. Kontos, Y. S. Raptis, P. Falaras, A. Van der Ven, M. G. Kanatzidis, and R. Seshadri. Dynamic Stereochemical Activity of the  $\text{Sn}^{2+}$  Lone Pair in Perovskite  $\text{CsSnBr}_3$ . *J. Am. Chem. Soc.* 2016, 138, 11820–11832.
- (25) Mori, M.; Saito, H. An x-ray study of successive phase transitions in  $\text{CsSnBr}_3$ . *J. Phys. C: Solid State Phys.* 1986, 19, 2391-2401.
- (26) Hirotsu, S.; Harada, J.; Iizumi, M. Structural phase transitions in  $\text{CsPbBr}_3$ . *Journal of the physical society of Japan* 1974, 37, 1393-1398.
- (27) Swainson, I.; Chi, L.; Her, J.-H.; Cranswick, L.; Stephens, P.; Winkler, B.; Wilson, D. J.; Milman, V. Orientational Ordering, Tilting and Lone-pair Activity in the Perovskite Methylammonium Tin Bromide,  $\text{CH}_3\text{NH}_3\text{SnBr}_3$ . *Acta Cryst. B* 2010, 66, 422-429.
- (28) Hu, Q. Y.; Shu, J.-F.; Cadien, A.; Meng, Y.; Yang, W. G.; Sheng, H. W.; Mao, H.- K. Polymorphic Phase Transition Mechanism of Compressed Coesite. *Nature Comm.* 2015, 6, 6630.
- (29) Liu, G.; Kong, L.; Guo, P.; Stoumpos, C. C.; Hu, Q.; Liu, Z.; Cai, Z.; Gosztola, D. J.; Mao, H.-K.; Kanatzidis, M. G.; Schaller, R. D. Two Regimes of Bandgap Red Shift and Partial Ambient Retention in Pressure-Treated Two-Dimensional Perovskites. *ACS Energy Lett.* 2017, 2 (11), 2518-2524.
- (30) Yin, T., Liu, B.; Yan, J.; Fang, Y.; Chen, M.; Chong, W. K.; Jiang, S.; Kuo, J.-L.; Fang J., Liang, P.; Wei, S.; Ping, K.; Tze, L.; Sum, C.; White, T. J.; Shen, Z. X. Pressure-Engineered Structural and Optical Properties of Two-Dimensional  $(\text{C}_4\text{H}_9\text{NH}_3)_2\text{PbI}_4$  Perovskite Exfoliated nm-Thin Flakes. *J. Am. Chem. Soc.* 2019, 141 (3), 1235-1241.
- (31) Xiao, G.; Cao, Y.; Qi, G.; Wang, L.; Liu, C.; Ma, Z.; Yang, X.; Sui, Y.; Zheng, W.; Zou, B. Pressure Effects on Structure

and Optical Properties in Cesium Lead Bromide Perovskite Nanocrystals J. Am. Chem. Soc. 2017, 139 (29), 10087-10094.

(32) Zhu, H.; Cai, T.; Que, M.; Song, J.-P.; Rubenstein, B. M.; Wang, Z.; Chen, O. Pressure-Induced Phase Transformation and Band-Gap Engineering of Formamidinium Lead Iodide Perovskite Nanocrystals. J. Phys. Chem. Lett. 2018, 9 (15), 4199-4205

(33) Jaffe, A.; Lin, Y.; Mao, W. L.; Karundasa, H. I. Pressure-Induced Metallization of the Halide Perovskite (CH<sub>3</sub>NH<sub>3</sub>)PbI<sub>3</sub>. J. Am. Chem. Soc. 2017, 139, 4330-4333.

(34) Quarti, C; Mosconi, E.; De Angelis F. Structural and electronic properties of organo-halide hybrid perovskites from ab initio molecular dynamics. Phys. Chem. Chem. Phys., 2015, 17, 9394

(35) Lee, J. H.; Bristowe, N. C.; Lee, J. H.; Lee, S. H.; Bristowe, P. D.; Cheetham, A. K.; Jang, H. M. Resolving the Physical Origin of Octahedral Tilting in Halide Perovskites, Chem. Mater. 2016, 28, 4259-4266.

(36) Grote, C. and Berger, R. F. Strain Tuning of Tin–Halide and Lead–Halide Perovskites: A First-Principles Atomic and Electronic Structure Study, J. Phys. Chem. C 2015, 119, 22832-22837.

(37) Zhang, L.; Zeng, Q. and Wang, K. Pressure-Induced Structural and Optical Properties of Inorganic Halide Perovskite CsPbBr<sub>3</sub>. J. Phys. Chem. Lett. 2017, 8, 3752–3758.

(38) Pisanu, A.; Mahata, A.; Mosconi, E.; Patrini, M.; Quadrelli, P.; Milanese, C.; De Angelis, F.; Malavasi, L. Exploring the Limits of Three-Dimensional Perovskites: The Case of FAPb<sub>1-x</sub>Sn<sub>x</sub>Br<sub>3</sub>. ACS Energy Lett. 2018, 3, 1353–1359.

(39) Amat, A.; Mosconi, E.; Ronca, E.; Quarti, C.; Umari, P.; Nazeeruddin, M. K.; Grätzel, M.; De Angelis, F. Cation-Induced Band-Gap Tuning in Organohalide Perovskites: Interplay of

Spin–Orbit Coupling and Octahedra Tilting. *Nano Lett.* 2014, 14, 3608-3616.

(40) Quarti, C.; Mosconi, E. and De Angelis, F. Interplay of Orientational Order and Electronic Structure in Methylammonium Lead Iodide: Implications for Solar Cell Operation, *Chem. Mater.* 2014, 26, 6557–6569.

(41) Etienne, T.; Mosconi, E.; and De Angelis, F. Dynamical Origin of the Rashba Effect in Organohalide Lead Perovskites: A Key to Suppressed Carrier Recombination in Perovskite Solar Cells?, *J. Phys. Chem. Lett.* 2016, 7, 1638-1645.

# PHYSICAL MODULATION TECHNIQUES

As mentioned before, it is possible to tune the properties of metal halide perovskites by either chemical or physical modulation techniques.

For the reasons explained in paragraph 1.3, we decided to direct our attention to the physical ones.

Many physical parameters can be tuned to modulate materials, such as temperature<sup>112</sup> or pressure, and, as just seen in the previous chapter, the effect of temperature on metal halide perovskites is already largely studied.

This fact, the possibility to carry on preliminary high-pressure studies, and the interest in scalability led us to search for physical techniques that could not involve the temperature parameter and at least partially imply the use of high-pressure.

Therefore, in this chapter we focus on two techniques that are both easily scalable and already used in the industry: high-pressure quenching, by the means of a Spark Plasma Sintering apparatus, and extended ball milling



## 4.1 High-pressure quenching

In material science, quenching is a sudden change of a physical quantity, and it is usually applied to “freeze” a material property or situation.

The most diffuse version is related to the temperature: it is the rapid cooling of material in water, oil, air, or gas, and it is applied every day in the industry to produce metal artifacts.

Speaking about pressure quenching instead, the most of papers in the literature about this topic are related to gas quenching<sup>113,114</sup> and only a few to “physical” (in sense of pressure transmitted by physical contact) pressure quenching<sup>115</sup>.

### 4.1.1 MAPI

#### **Ambient condition retention of band-gap tuning in MAPbI<sub>3</sub> induced by high pressure quenching**

##### *Purpose and scope*

In the present work, we show a successful approach to achieve stable structural and optical changes induced by pressure on bulk amounts of MAPI after pressure release. Such effects on the optical properties resemble those achieved in situ (e.g., in diamond anvil cells) but are retained and stabilized under ambient conditions thanks to a partial quenching of the high-pressure state. The apparatus used to carry on the experiment is that of Spark Plasma Sintering, an easily scalable and already industrial technique.

## Introduction

High-pressure (HP) has been widely applied in recent times as a probe to tune the physical properties of hybrid organic–inorganic perovskites (HOIPs) such as methylammonium (MA) and formamidinium lead halides.<sup>1–3</sup> The common approach for HP investigation is by means of diamond anvil cells (DACs) coupled to in situ X-ray diffraction (XRD) and photoluminescence (PL) probes. After extensive investigation of several HOIPs, a general trend in the evolution of the crystal structure and of the optical properties with pressure has been observed. In particular, all the MAPbX<sub>3</sub> compounds experience two phase transitions upon increasing pressure (cubic-cubic-orthorhombic) followed by amorphization at a relatively low pressure of about 2 GPa, with a progressive lattice shrinkage.<sup>1–3</sup> An interesting feature of lead halide hybrid perovskites is that, even after compression up to 20–30 GPa, they recover the full crystalline phase under ambient conditions once the pressure is released.<sup>1–3</sup> This has been interpreted as due to the different behaviors of the organic component and of the inorganic framework under pressure, with a reduction of the average order of the crystal upon applying pressure.<sup>1,4</sup>

The trend of the optical properties of MAPbX<sub>3</sub> perovskites under pressure, determined by in situ PL measurements, shows, in general, an initial red-shift up to about 1 GPa, followed by a gradual blue-shift in the high-pressure crystal phases and a subsequent quenching of the PL in the amorphous phase.<sup>1–3</sup> For MAPbI<sub>3</sub> (MAPI), for example, the red-shift of  $E_g$  is around 30–40 meV, with the following blue-shift (up to about 2 GPa) being more or less of the same order. Such variations of the band-gap energies are usually correlated with the on-set of the different crystal structures as P increases.<sup>1–5</sup>

The tuning of the optical properties of hybrid organic–inorganic lead halide perovskites is of significant current interest and, in all of the in situ high-P works available, there is a clear suggestion towards the possible transfer (e.g., through substrate interactions and/or chemical pressure) of such modifications under ambient conditions, thus providing a further mean of engineering the hybrid perovskite properties. However, up to now, there is no evidence of ambient retention of pressure-induced effects on 3D hybrid perovskites. On the other hand, retention of the bandgap red shift and PL enhancement in a decompressed sample was recently shown for a 2D Ruddlesden–Popper perovskite.<sup>6</sup> This study demonstrated that pressure/strain engineering can be a real possibility for modifying material not only in situ but also ex situ.<sup>6</sup> However, also in this case the ex situ permanent engineering of pressure induced phenomena was carried out with a DAC cell.<sup>6</sup> It is well known that DACs operate on few crystallites of the material under investigation, and it is clear that they do not represent the real means to scale up the possible ex situ effects caused by pressure application. In view of these considerations, in the present work, we explored the possibility of achieving an ambient conditions retention of the pressure-induced effects on bulk amounts of MAPI.

### Experimental methods

**High-pressure equipment.** The pressure has been applied and measured by a homemade high-pressure apparatus usually employed for Spark Plasma Sintering too. Samples were pressed within 5 mm cells (containing about 100 mg of the starting material) by keeping the desired pressure for 5 minutes, followed by pressure release.

**XRD diffraction.** The structural properties of the deposited thin films were characterized by X-ray diffraction (XRD) by means of a Bruker D8 Advance instrument (Cu radiation) in a Bragg-Brentano setup.

**Photoluminescence spectroscopy.** PL spectra have been collected ex-situ by the means of a homemade Raman apparatus.

**SEM.** Microstructural characterization of the samples was made using a high-resolution scanning electron microscope (SEM, TESCAN Mira 3).

### Results and discussion

The experimental approach used in the present work was to apply pressure through the use of a home-made high-pressure apparatus. Samples were pressed within 5 mm cells (containing about 100 mg of the starting material) by keeping the desired pressure for 5 minutes, followed by pressure release, and were characterized for their crystal structure and optical properties. One peculiarity of this technique is the very fast pressure release which occurs within a few milliseconds after compression. A sketch of the apparatus employed to run the HP experiments is reported in Figure 4.1.

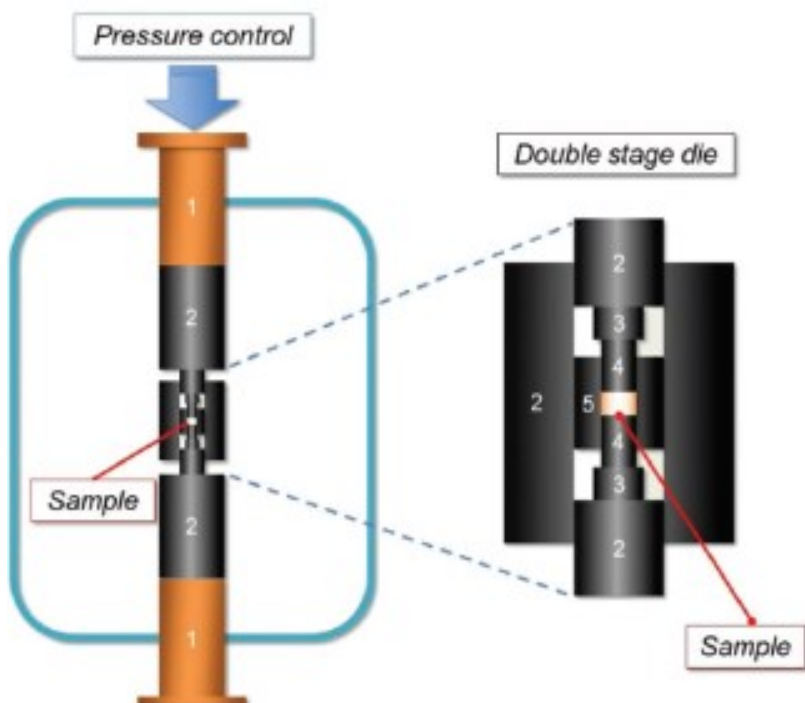


*Figure 4.1* High pressure schematics. The external rams applying the uniaxial pressure are made of copper (1). The double stage die is mainly made of graphite (2), with the exception of the inner parts (3, 4, and 5) which are made of SiC or WC

After pressure release, the sample was taken out from the cell and laboratory X-ray diffraction measurements were performed to determine the crystal structure. The patterns collected on a series of MAPI samples are reported in Figure 4.2.

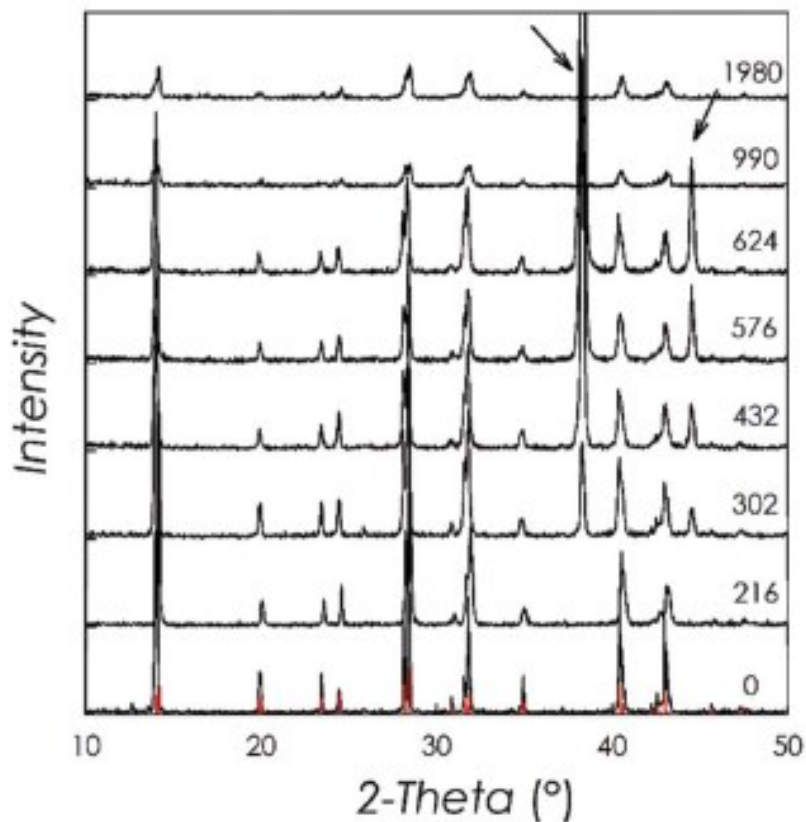
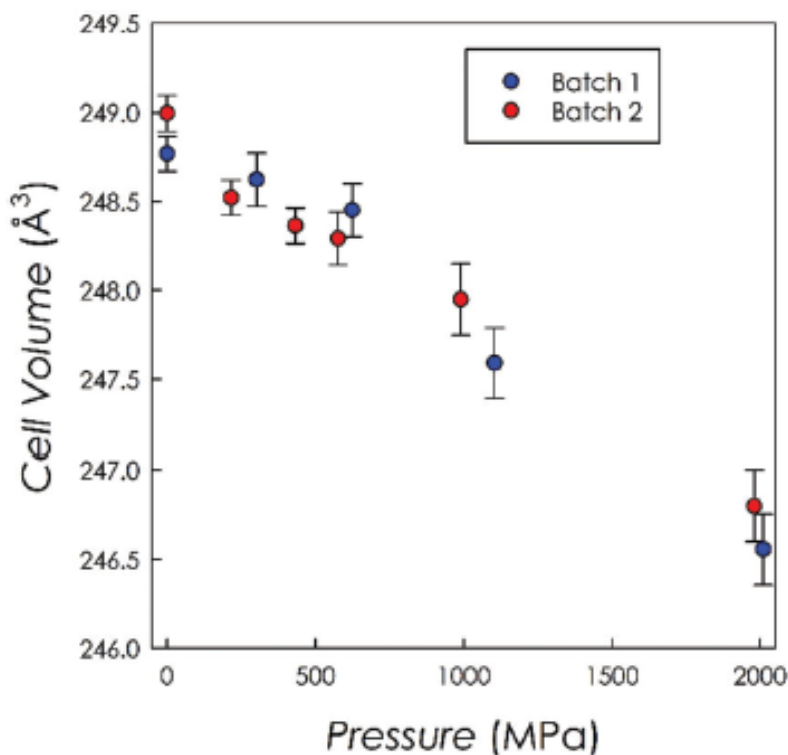


Figure 4.2 XRD patterns of MAPI samples reported in the paper with the corresponding compression pressures in MPa. Vertical red bars: reference patterns for tetragonal MAPI. Arrows in the figure refer to sample-holder signals.

We carried out all the experiments in duplicate in order to verify the reproducibility of the results.

The analysis of the XRD patterns shown in Figure 4.2 indicates that, after pressure application and removal from the cell, all the samples retain a crystalline state without detectable evidence of an amorphous phase. There is a slight loss of crystallinity as  $P$  increases, as can be noticed from the reduction of the  $K_{\alpha 1}$ – $K_{\alpha 2}$

splitting, due to the peak broadening and peak intensity reduction. At the same time, all the samples show the typical tetragonal crystal structure of MAPI (I4/mcm).<sup>7</sup> This result is in agreement with previous DAC studies, which showed that, after sample amorphization at around 1.5–2 GPa, MAPI recovers the crystal state upon pressure release.<sup>1–5</sup>



*Figure 4.3* Cell volume as a function of pressure for MAPI samples determined ex situ after pressure application for the two series of samples considered in the present work.

The cell volumes (normalized to  $Z = 1$ ) of all the samples investigated in the present work are reported Figure 4.3.

A nearly linear reduction of the cell volume as a function of pressure can be clearly observed from Figure 4.3. It should be highlighted that these data come from ex situ XRD measurements, i.e. on stabilized samples after pressure release, which confirmed that the present experimental approach was effective in inducing a permanent unit cell size reduction on MAPI samples. While an in situ compression of the unit cell is obviously observed in all the DAC experiments, this is the first report of a stable lattice shrinkage retained by MAPI samples after the application of pressure. Overall, the lattice volume reduction is around 1%. Such reduction of the cell volume is of about 1 order of magnitude lower, for an analogous P-range, than that observed in in situ XRD measurements.<sup>5</sup> Generally, in DAC experiments, slight volume changes of the samples recovered under ambient conditions, after pressure release, are observed. However, such decompression in DACs has been reported to occur with markedly slower pressure release (i.e., hours) if compared to the present approach where P is released very quickly (within few milliseconds), thus suggesting a possible partial quenching of the HP state. This is the required approach in order to stabilize any high-pressure induced phenomena at ambient pressure since MAPI has been shown to recover the original crystalline phase even after being compressed to tens of GPa.<sup>1,2</sup> Since a retention of pressure-induced effects on the crystal lattice has been observed from the structural data, it is of interest to evaluate a possible retention of an ex situ effect on the optical properties of the samples which have undergone compression.



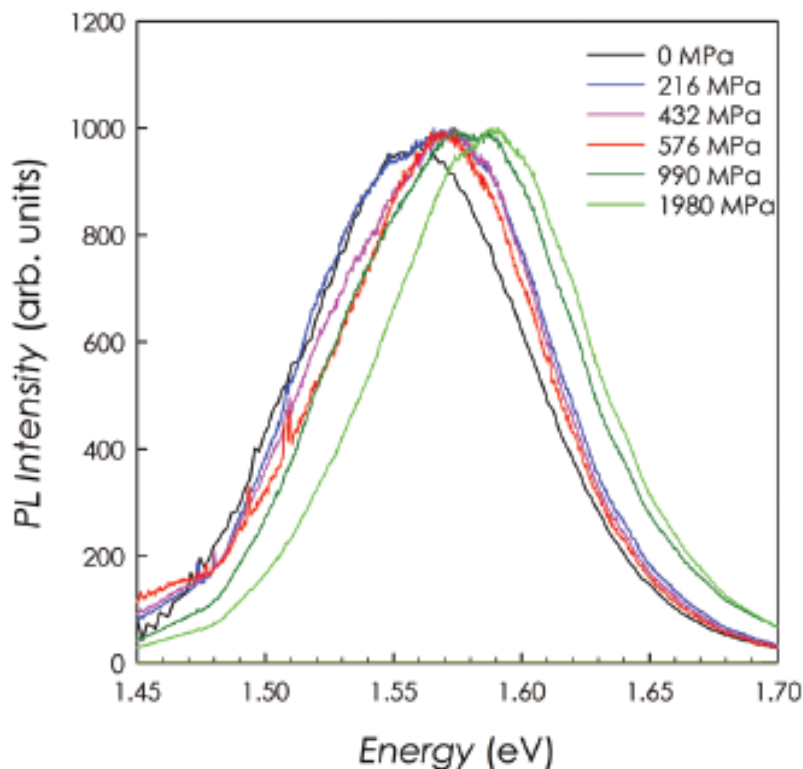


Figure 4.4 Normalized PL spectra for representative pressed MAPI samples

Figure 4.4 reports the normalized PL spectra (collected ex situ) as a function of energy (eV) for some representative samples (for sake of clarity), while Figure 4.5 reports the trend of the band gap value as a function of pressure for all the samples.

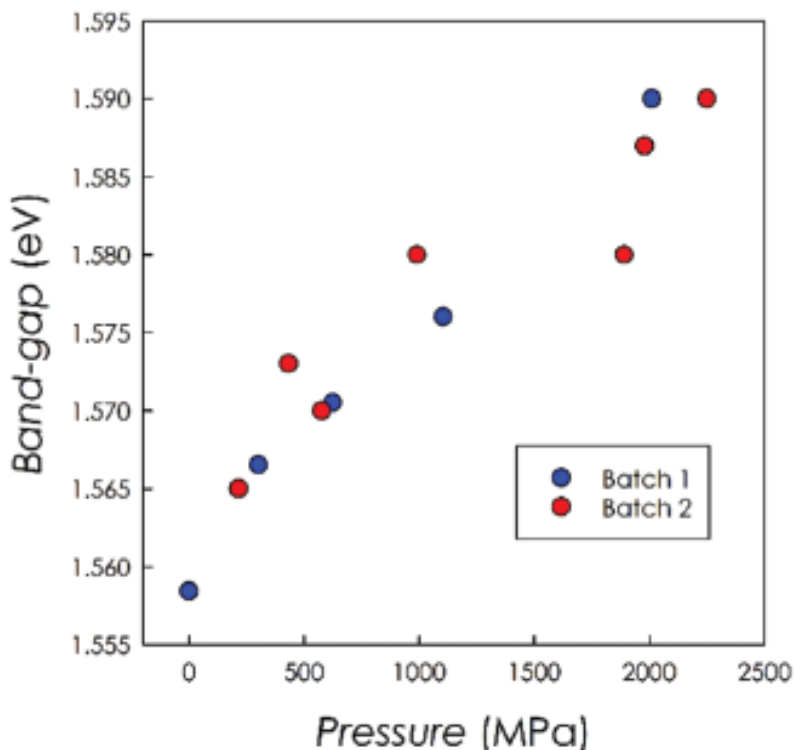


Figure 4.5 trend of band-gap as a function of pressure for all the samples

The steady-state PL spectra present a continuous blue shift of about 35 meV from the as-prepared sample to that pressed at 2000 MPa: this clearly indicates that the MAPI structure retains a modulation of the band-gap which is a consequence of the quenching of the high-pressure state. In addition, there is a fairly good agreement between the two series of independent samples prepared and measured, confirming the good reproducibility of the method. Again, we stress that the MAPI samples have been measured *ex situ* after pressure application with the HP-equipment, thus highlighting a permanent retention of pressure-induced engineering of the band-gap.

While, for the reasons reported above, a direct comparison with available in situ HP PL studies on MAPI is not straightforward, it is of interest to note that a blue-shift is as well commonly observed during DAC experiments.<sup>1-5,8</sup> In those cases, this occurs in situ around 1 GPa (followed by a progressive amorphization of the sample), and has been correlated to the onset of a structural phase transition, with a tilting of the octahedra and a deviation of the Pb-I-Pb angle from 180°. This should lead to a decrease of the contributions of Pb orbitals to the CBM and to a band-gap increase and a concomitant blue shift of the PL.<sup>9</sup> As shown by the structural data reported in this work, the present samples retain a tetragonal crystal structure under ambient conditions, thus indicating that such band-gap effects can be effectively achieved while preserving an average tetragonal symmetry. Most probably, the fast pressure release achieved with the technique employed in the present work may lead to a partial quenching of the HP structural features, which results in the retention, under ambient conditions, of local structural distortions and atomic configurations likely correlated to the average structural changes observed, for example, during in situ DAC experiments. In fact, hybrid perovskites are known to be naturally characterized by local distortions in the high-symmetry phases (cubic and tetragonal), and we may expect that they are prone to accommodate an even higher level of local structural distortions, induced by HP treatment, in the tetragonal structure shown, under ambient conditions, in the present work.<sup>10,11</sup> It is known that, for 2D perovskites, the energy difference between the metastable (quenched from HP) and ground states is small and, expecting an analogous trend also for 3D perovskites, this characteristic may be advantageously used through the application of a HP-quenching technique such as the one used here. One key point of the present approach is that it is possible to achieve a modulation of the pressure-induced

quenched state under ambient conditions by changing the applied pressure, which cannot be easily obtained with other methods such DACs (having a device-limited speed of pressure release). Further investigation of the possible local structure deformation will be the subject of future work by means of X-ray pair distribution function analysis.

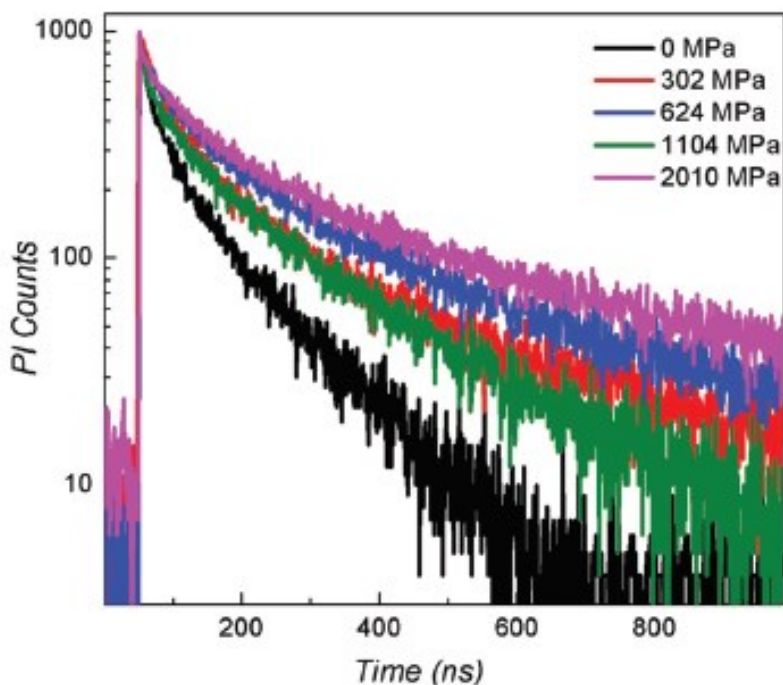


Figure 4.6 TR-PL spectra for representative pressed MAPI samples

On a series of selected samples, spanning the whole pressure range investigated, we performed time-resolved PL (TR-PL) measurements. The results are reported in Figure 4.6. Although one of the samples (302 MPa) does not lie in the picture, the general trend indicates a correspondence between the increase in the band-gap, induced by the pressure, and the increase in the

measured radiative lifetimes. Here the correspondence with the in situ DAC experiments is definitively lost, as in these the band-gap narrowing occurring between 0 and 300 MPa induced a lifetime increase meanwhile the blueshift following the phase transition (300 MPa–2 GPa) led to a PL lifetime decrease.<sup>8</sup>

Again, it is worth noticing the fundamental difference of our approach: inducing a long lasting modification on the systems persisting after pressure release. In balancing between the radiative and non-radiative phenomena in such complex materials, electronic trap density and distribution and material grain dimensions play a fundamental role. In addition, very recently theoretical and experimental works have shown that a complex scenario depicts the near-band-edge transition in MAPI comprising multiple direct transitions and, at least at room-temperature, an indirect band gap. The rationalization of the near-band-edge transition behaviour and the role of the indirect transition and its influence on the radiative carrier recombination are under debate and constitute a main field research focus.<sup>8,12–</sup>

<sup>14</sup> As showed above, herein the high pressure application followed by fast release induces a permanent modification, specifically a reduction of the cell volume associated to a retention, under ambient conditions, of the local structural distortions and atomic configurations, and these modifications can certainly have an effect on both the direct and indirect energy distributions with an impact on the carrier deactivation dynamics. We underline how this leads to the MAPI emission blue-shift and a concomitant increase of its radiative lifetime. The time stability of the effects observed on the optical properties has been checked by re-measuring the samples after 15 days from pressure treatment. By looking at the steady state PL spectra collected after compression and 15 days later, a very good overlap of the spectra can be seen, with  $E_g$  values within  $\pm 2\text{--}3\text{meV}$ . This is an important and encouraging result

suggesting an effective long-term retention of the P-induced phenomena.

Finally, since it is known that a modulation of the optical properties may be induced by variation on the grain-size of hybrid perovskites, we investigated the samples' morphology after each pressure application point through scanning electron microscopy (SEM) analysis. The images for low, intermediate and high pressure treatments show a very similar morphology for all the samples. These data allow us to rule out any dependence of the pressure-induced effects observed with a possible significant change of the crystal microstructure.

### Conclusions

In this work we explored and provided a novel approach to stabilize, under ambient conditions, high-pressure induced effects on a prototype hybrid perovskite system, namely MAPI. The very fast pressure release used in the present work provides a quenching of high-pressure states which are stably retained in the material, providing a significant modulation of the band gap energy. Such a novel approach can be applied to bulk amounts of material thus opening the way to a real possible use of pressure as a tool to modify the hybrid perovskite properties. Future work will aim at further extending the use to other classes of perovskites for optical and photovoltaic applications.

### References

1. P. Postorino and L. Malavasi, J. Phys. Chem. Lett., 2017, 8, 2613–2622.
2. M.Szafran'ski and A. Katrusiak, J. Phys. Chem. Lett., 2017, 8, 2496–2506.

3. A. Jaffe, Y. Lin and H. I. Karunadasa, *ACS Energy Lett.*, 2017, 2, 1549–1555.
4. M. Szafran'ski and A. Katrusiak, *J. Phys. Chem. Lett.*, 2016, 7, 3458–3466.
5. F. Capitani, C. Marini, S. Caramazza, P. Postorino, G. Garbarino, M. Hanfland, A. Pisanu, P. Quadrelli and L. Malavasi, *J. Appl. Phys.*, 2016, 119, 185901.
6. G. Liu, L. Kong, P. Guo, C. C. Stoumpos, Q. Hu, Z. Liu, Z. Cai, D. J. Gosztola, H.-K. Mao, M. G. Kanatzidis and R. D. Schaller, *ACS Energy Lett.*, 2017, 2, 2518–2524.
7. S. Colella, M. Todaro, S. Masi, A. Listorti, D. Altamura, R. Caliendo, C. Giannini, E. Carignani, M. Geppi, D. Meggiolaro, G. Buscarino, F. De Angelis and A. Rizzo, *ACS Energy Lett.*, 2018, 3, 1840–1847.
8. T. Wang, B. Daiber, J. M. Frost, A. S. Mann, E. C. Garnett, A. Walsh and B. Ehrler, *Energy Environ. Sci.*, 2017, 10, 509–515.
9. M. R. Filip, G. E. Eperon, J. Snaith and F. Giustino, *Nat. Commun.*, 2014, 5, 5757.
10. K. Page, J. E. Siewenie, P. Quadrelli and L. Malavasi, *Angew. Chem., Int. Ed.*, 2016, 55, 14320–14324.
11. A. Bernasconi and L. Malavasi, *ACS Energy Lett.*, 2017, 2, 863–868.
12. E. M. Hutter, M. C. Ge'lviz-Rueda, V. Bulovic, F. C. Grozema, S. D. Stranks and T. J. Savenjie, *Nat. Mater.*, 2017, 16, 115–120.
13. T. Kirchartz and U. Rau, *J. Phys. Chem. Lett.*, 2017, 8, 1265–1271.
14. W. Huang, et al., *ACS Photonics*, 2018, 5, 1583–1590.

## 4.2 Extended ball milling

A ball miller is a grinder constituted by a cylindrical container called “jar” (see Figure 4.7). The jar is hermetically closed and it is filled with balls of the same material: usually steel or tungsten carbide or  $\text{ZrO}_2$ . The jar rotates at a proper speed giving to the balls the force to be the grinding media.

This technique is easily scalable and largely employed in the industry. It is mainly applied for grinding<sup>116,117</sup> and to carry on many types of syntheses (solid or solid-liquid)<sup>118–120</sup>, but it is possible to find in literature more “exotic” applications too, such as mechanical alloying<sup>121</sup> or amorphization<sup>122</sup>.

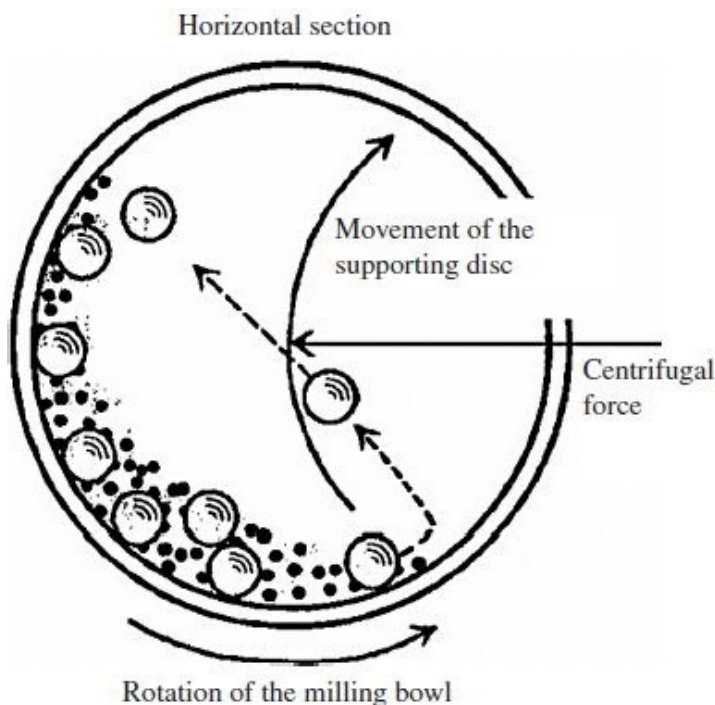


Figure 4.7 Scheme of a ball milling process



### 4.2.1 MAPI and $\text{PEA}_2\text{PbBr}_4$

#### **The Effect of Extended Ball-Milling upon Three-Dimensional and Two-Dimensional Perovskite Crystals Properties**

##### *Purpose and scope*

Here we discovered that the ball milling process, extended over a large temporal window, is related to the structural and optical properties of referential three-dimensional (3D)  $\text{MAPbI}_3$  (MA = methylammonium) and two-dimensional (2D)  $\text{PEA}_2\text{PbI}_4$  (PEA = phenylethylammonium) perovskite crystals.

For both 2D and 3D systems, the process induces a reduction of the crystallite dimension, accompanied by a worsening of the overall crystallinity, but without any sign of amorphization. For  $\text{MAPbI}_3$ , an intriguing room temperature structural transition, from tetragonal to cubic, is observed. The processing in both cases impacts the morphology, with a reduction of the crystal shape quality connected to the particles' agglomeration tendency.

All these effects translate to a “blue shift” of the absorption and emission features, suggesting the use of this technique to modulate the 3D and 2D OHPs' properties.

##### *Introduction*

In recent years, organometal halide perovskites (OHPs) have gained enormous attention as active materials applicable in several optoelectronic applications, such as solar cells, light emitting devices, photodetectors and field-effect transistors<sup>1-6</sup>. These materials indeed own exceptional optoelectronic

properties, such as high absorption coefficients, the direct photogeneration of free carriers and long carrier diffusion length, and can be manufactured using numerous and low-energy consuming methods<sup>1,7-10</sup>.

Most of the studies reported in the literature concern the investigation and application of thin film OHPs<sup>9,11,12</sup>. However, these films are usually characterized by a grain structure and morphology that directly impact on the optoelectronic features, since they are a collection of crystallites, amorphous phases and unreacted species<sup>4,13-15</sup>. Additionally, their optical and electronic properties can be dominated by extrinsic defects, since trap states are more easily generated at the grain boundaries<sup>11</sup>. Therefore, in order to understand the intrinsic properties of these appealing materials, polycrystalline powdered samples represent an ideal model to be examined for the expected lower defect density (resulting from the absence of inter-grain regions), and for certain chemical compositions<sup>5,8,12,13,16-19</sup>.

Peculiarly, the use of polycrystalline samples has nowadays gained significant attention with regards to the exploitation of the effects of different factors, such as chemical manipulation and external perturbations, on the structural, morphological and optoelectronic properties of the hybrid perovskites<sup>20-34</sup>. In some recent examples, polycrystalline samples were synthesized and investigated in order to (i) measure the impact of rubidium ions' incorporation into multiple-cation perovskites  $\text{Rb}(\text{MAFA})\text{PbI}_3$  (MA = methylammonium; FA = formamidinium)<sup>21</sup>, (ii) study the role of different organic cations [27], (iii) study the effect of illumination<sup>34</sup> on  $\text{MAPbI}_3$  properties, iv) explore the consequence of halide substitution in a lead-free  $\text{BZA}_2\text{SnX}_4$  (BZA = benzylammonium; X = Cl, Br or I) system<sup>28</sup>, (v) analyze the degradation processes triggered by the X-ray,  $\text{N}_2$ ,  $\text{O}_2$  or  $\text{H}_2\text{O}$  exposure of  $\text{MAPbBr}_3$  perovskite<sup>29</sup>, and (vi) assess its enhanced photoluminescence and photoconductivity attributed to erbium-

doping<sup>22</sup>. Perovskites crystals were also employed to evaluate the responses of OHPs to external temperature and pressure, which is considered a physical probe for tailoring the properties of these materials<sup>25,33</sup>. Indeed, the results of different temperatures and/or pressures on the structural and optoelectronic features of MAPbI<sub>3</sub><sup>22-25,32</sup>, MAPbBr<sub>3</sub><sup>30-32</sup> and FAPbI<sub>3</sub><sup>33</sup> crystals have been reported in the literature.

Herein, polycrystalline powdered samples of three-dimensional (3D) and two-dimensional (2D) OHPs are examined in order to evaluate the effects of prolonged high-energy ball-milling processes on their structural and optical properties. High-energy ball-milling is a mechanical grinding of materials, in which the milling occurs thanks to the mechanical friction between the material and a grinding medium (i.e., balls) included in a container<sup>35-37</sup>. This technique can have different consequences on the treated materials, such as different extents of downsizing, efficient mixing, solid-state chemical transformations, or a combination of all of these<sup>36</sup>. Very importantly, it can be applied as an environmentally friendly, reproducible, efficient and simple synthesis method for a variety of solid materials, among which are OHPs<sup>24,35,38</sup>. In particular, the use of this methodology should be considered as an alternative chemical strategy and a promising avenue for synthesizing high-purity OHP crystals in a solvent-free manner, which is expected to pave the way for the investigation of the fundamental properties (relevant to their implementation into optoelectronic devices) of these materials<sup>35,38-42</sup>. However, to our knowledge, few publications deal with the description of the process in detail, and in particular, with the study of its effects on the final OHPs samples. The present study aims to investigate the results of prolonged ball-milling on the structural, morphological and optical properties of MAPbI<sub>3</sub> 3D and PEA<sub>2</sub>PbI<sub>4</sub> (PEA = phenylethylammonium) 2D perovskite crystals.

For this purpose, polycrystalline samples were prepared via wet-chemistry methods, subjected to high-energy ball-milling for different times, and characterized by means of X-ray diffraction (XRD), scanning electron microscopy (SEM) and absorbance and photoluminescence (PL) spectroscopies.

### Experimental methods

#### **Syntheses of perovskites**

The polycrystalline MAPbI<sub>3</sub> 3D and PEA<sub>2</sub>PbI<sub>4</sub> 2D perovskite powders were synthesized using a wet-chemistry method<sup>33</sup> with the following steps: (i) dissolving stoichiometric lead (II) acetate (Sigma Aldrich; 99.9%) in a large excess (9 times for MAPbI<sub>3</sub>, 15 times for PEA<sub>2</sub>PbI<sub>4</sub>) of hydriodic acid (57 wt % in H<sub>2</sub>O, 99.99%, Sigma Aldrich) or hydrobromic acid (48 wt % in H<sub>2</sub>O, ACS Reagent, Sigma Aldrich); (ii) heating up to 100 °C within an oil bath; (iii) adding a stoichiometric quantity of methylamine (40 wt % in H<sub>2</sub>O, Sigma Aldrich) or phenethylamine (≥99%, Sigma Aldrich); (iv) letting it cool down to 50 °C; (v) filtering by means of a water pump; and (vi) heating to 60 °C in a vacuum in a B-585 glass oven (BUCHI) for 10 h. All the first 4 synthesis steps were carried out in nitrogen flux.

#### **High-Energy Ball-Milling Processes**

Four grams of each synthesized powder were ground by means of a planetary ball-milling machine (Fritsch, Pulverisette 7, Premium Line) equipped with tungsten carbide (WC) jars and balls (each ball about 1 g)<sup>28</sup>. The samples were prepared with a powder–balls ratio of 1:10, by alternating 20 min of grinding at 800 rpm with a 10 min break, for total times of 240 and 420 h for MAPbI<sub>3</sub> and PEA<sub>2</sub>PbI<sub>4</sub>, respectively. The same amounts (~100 mg) of the MAPbI<sub>3</sub> samples were taken from each jar after

72, 120, 192 and 240 h; the same was done for  $\text{PEA}_2\text{PbI}_4$  after 120, 204, 324 and 420 h.

### **Sample Characterization**

XRD investigations of the powder samples were carried out with a Bruker D8 Advance diffractometer using copper K radiation ( $\lambda=1.54056 \text{ \AA}$ ) as the X-ray source, under an ambient condition (i.e., temperature  $25^\circ\text{C}$ , humidity 25%). The measurements were performed in the Bragg–Brentano configuration, with a resolution of 0.02 and an integration time of 4 s.

A TESCAN Mira 3 high-resolution scanning electron microscope was used to perform the morphological characterization of the samples. SEM images were acquired at a working distance in the range 8.0–8.5 mm, an electron acceleration voltage of 20.00 kV, and 5.00–10.00 kx magnification.

Total absorption spectra were recorded with a PerkinElmer LAMBDA 1050 High Performance Series spectrophotometer including an integrating sphere for the collection of all the light scattered by the sample.

Steady state and time-resolved PL was measured by an Edinburgh FLS980 spectrometer equipped with a Peltier-cooled Hamamatsu R928 photomultiplier tube (185–850 nm). An Edinburgh Xe900 450W Xenon arc lamp was used as the exciting light source. Corrected spectra were obtained via a calibration curve supplied with the instrument (lamp power in the steady state PL experiments  $\sim 0.6 \text{ mW/cm}^2$ , spot area  $0.5 \text{ cm}^2$ ). Emission lifetimes were determined with the single photon counting technique by means of the same Edinburgh FLS980 spectrometer using a laser diode as the excitation source (1 MHz,  $\lambda_{\text{exc}} = 635 \text{ nm}$ , 67 ps pulse width and about 30 ps time resolution after deconvolution) and a Hamamatsu MCP R3809U-50 (time

resolution 20 ps) as detector (laser power in the TRPL experiment  $\sim 1.6 \text{ mW/cm}^2$ , spot area  $0.3 \text{ mm}^2$ ).

### Results and discussion

The powder XRD patterns of the  $\text{MAPbI}_3$  3D perovskite, after selected high-energy ball-milling times (0–240 h), are shown in Figure 4.8.

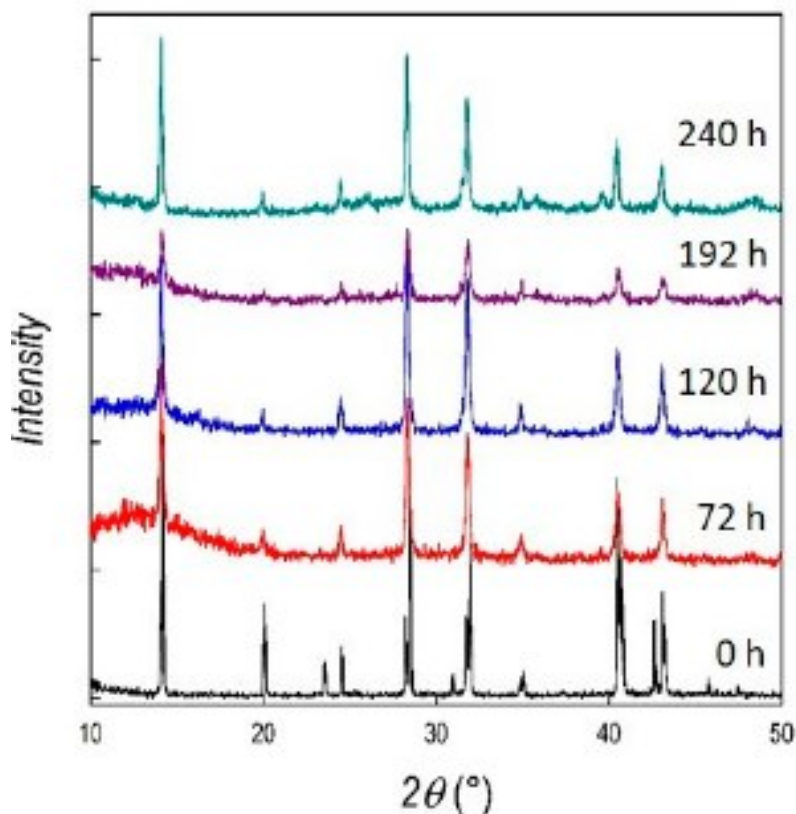


Figure 4.8 X-ray diffraction (XRD) patterns of  $\text{MAPbI}_3$  (MA = methylammonium) as a function of ball-milling time

As can be seen, even after 240 h of the external treatment, the sample maintains a good crystallinity, with only a slight peak broadening with respect to the starting pattern, probably originating from strain-induced defects due to the mechanical treatment. The XRD data of the as-prepared (0 h of ball-milling) MAPbI<sub>3</sub> that overlapped with the peaks of the tetragonal crystal structure (vertical red bars) are reported in the bottom part of Figure 4.9.

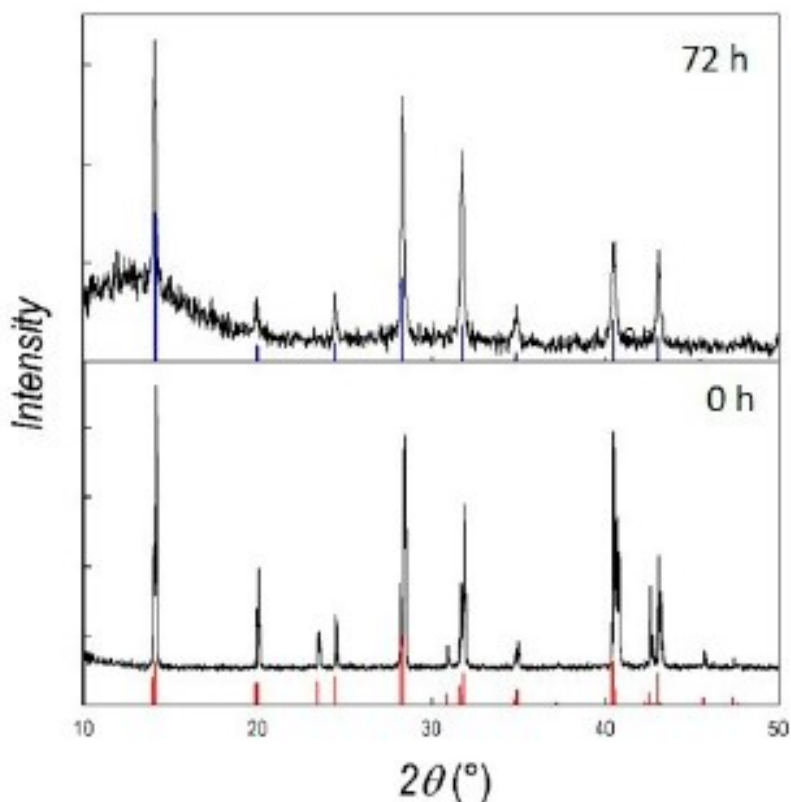


Figure 4.9 Bottom: XRD pattern of as-prepared MAPbI<sub>3</sub> overlapped with the expected pattern for the tetragonal unit cell; top: XRD pattern of 72 h-milled MAPbI<sub>3</sub> overlapped with the expected pattern for the cubic unit cell.

As can be appreciated, all the expected peaks are present in the experimental pattern, confirming the typical tetragonal structure of the synthesized MAPbI<sub>3</sub> perovskite<sup>25</sup>. On the other hand, already considering the pattern of the sample after 72 h of milling (top part of Figure 4.9), a clear phase transition occurs. The matching of the obtained diffraction peaks with those of the cubic phase (blue vertical bar) confirms the stabilization of this symmetry in the treated MAPbI<sub>3</sub> crystals. The clear sign of tetragonal symmetry<sup>25,43</sup>, namely, the two peaks around 2 $\theta$ , are not present in the milled sample, suggesting that the high-energy mechanical treatment induces the structural phase transition of the 3D perovskite<sup>32</sup>. The cubic symmetry is also found in all the samples by further increasing the milling time, as displayed in Figure 4.8. In addition, as reported in Table 4.1, the treatment has an effect on the lattice parameters, leading to a slight cell volume expansion as a function of time.

*Table 4.1* Lattice parameters and cell volume for MAPbI<sub>3</sub> at different ball-milling times

Crystalline Phase	Ball-Milling Time (h)	A (Å)	C (Å)	Cell Volume (Å <sup>3</sup> )
Tetragonal	0	8.868±0.001	12.628±0.001	248.300
	72	6.291±0.001	-	248.977
Cubic	120	6.293±0.001	-	249.214
	192	6.295±0.001	-	249.152
	240	6.301±0.001	-	250.166

The Le Bail approach was applied to calculate these parameters with a zero-shift value of -0.0651<sup>44</sup>.

The XRD patterns, as a function of the ball-milling time (0–420 h) for the PEA<sub>2</sub>PbI<sub>4</sub> 2D perovskite, are displayed in Figure 2.



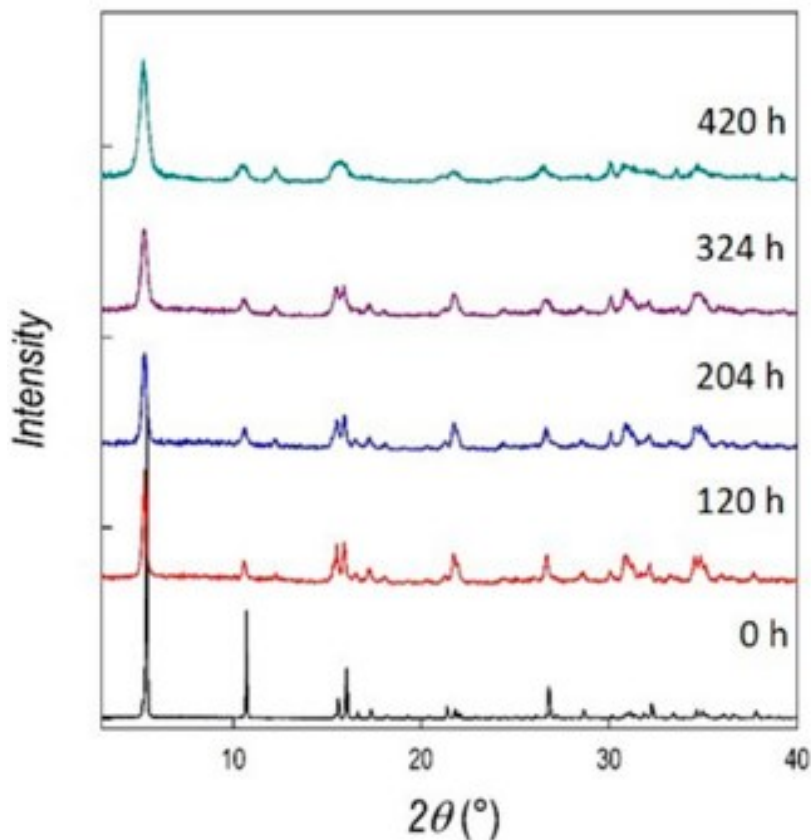
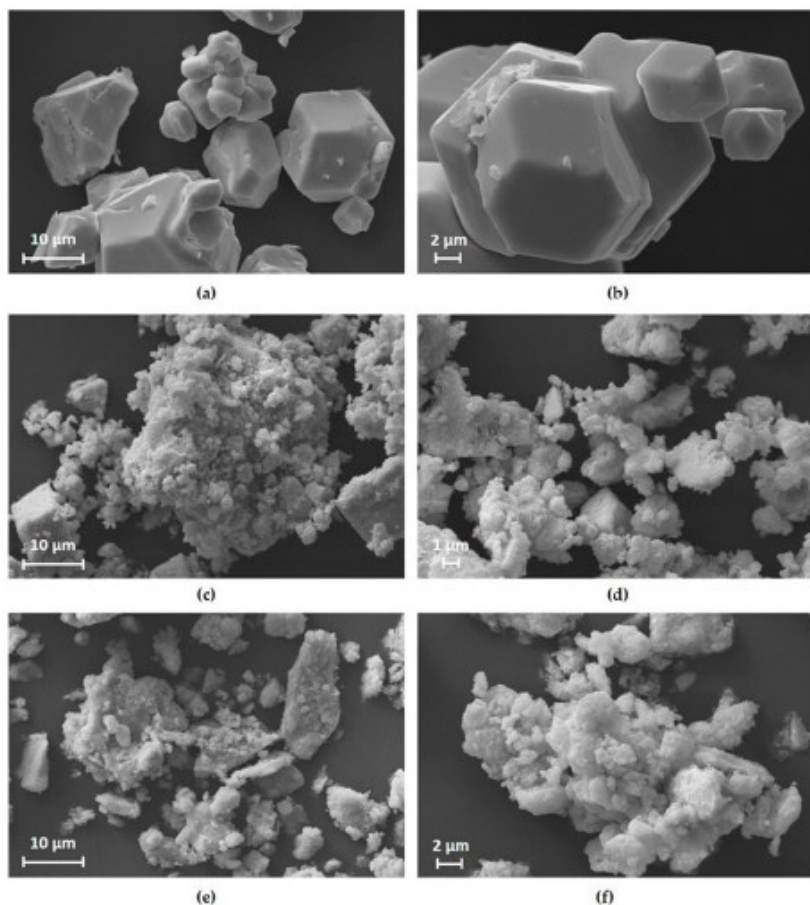


Figure 4.10 2. XRD patterns of  $\text{PEA}_2\text{PbI}_4$  (PEA = phenylethylammonium) as a function of ball-milling time

The crystal structure of the as-prepared material is in agreement with the monoclinic space group, and the pattern is dominated by the 001 peaks, as is common in 2D metal halide perovskites<sup>45,46</sup>. A significant crystallinity reduction is found in the samples, already after 120 h, and it is progressively increased by raising the milling treatment time, as can be appreciated by the peak's broadening. In particular, after 420 h of ball-milling,

most of the intensity is lost and the peaks are very broad. The FWHM moves from about  $0.05^{\circ}$  for the as-prepared sample, to about  $0.49^{\circ}$  after 420 h of milling time. At the same time, the first peak, corresponding to the 001 reflection, shifts to a lower angle by increasing the treatment, from  $5.413^{\circ}$  (0 h) to  $5.238^{\circ}$  (420 h), indicating an expansion of the c-axis. However, no sign of amorphization is found, suggesting the relevant robustness of the 2D sample structure. Furthermore, contrary to what was assessed for  $\text{MAPbI}_3$ , no evidences of phase transition are found in  $\text{PEA}_2\text{PbI}_4$  perovskite crystals as a consequence of the ball-milling treatment at various times.

Representative SEM images of the as-prepared and after-ball-milling  $\text{MAPbI}_3$  and  $\text{PEA}_2\text{PbI}_4$  samples are respectively reported in Figures 4.11 and 4.12.



*Figure 4.11* Scanning electron microscopy (SEM) images, at 5 kx and 10 kx magnification, of (a,b) as-prepared MAPbI<sub>3</sub>, and that after (c,d) 120 and (e,f) 240 h of ball-milling

The as-prepared MAPbI<sub>3</sub> (Figure 4.11-a,b) shows the typical cubic-like shape of the crystallites, which have dimensions ranging from 5 to 20–30 μm. The ball-milling is performed to significantly reduce the quality of the crystal shape, also producing smaller particles which tend to agglomerate (Figure

4.11-c–f). No other remarkable variations concerning the morphology can be observed by increasing the milling time from 120 to 240 h.

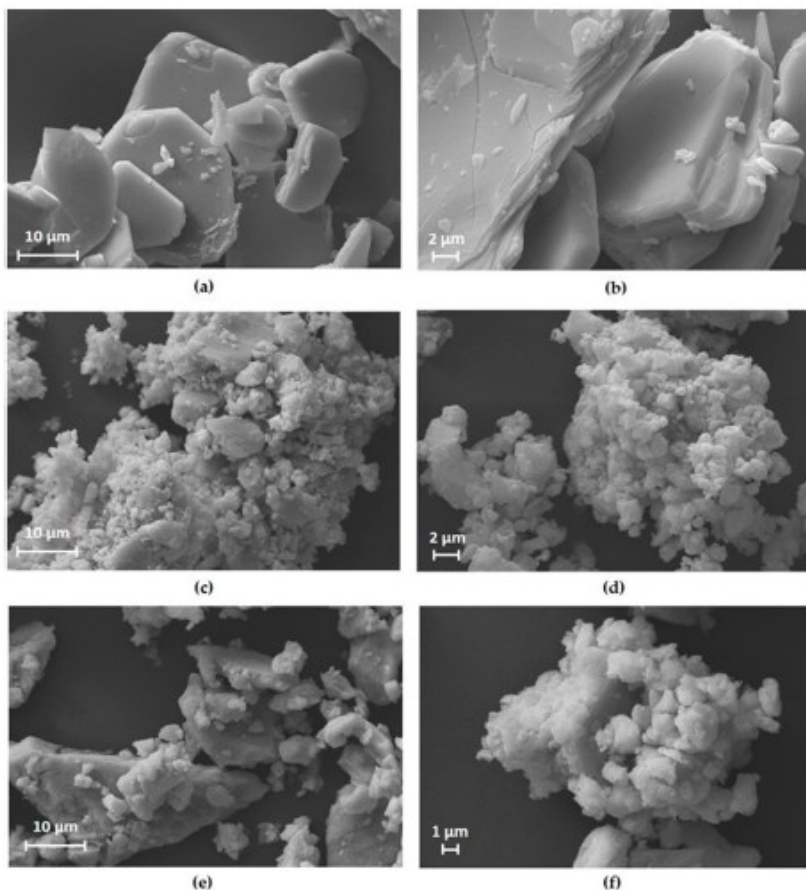


Figure 4.12 SEM images, at 5 kx and 10 kx magnification, of (a,b) as-prepared  $\text{PEA}_2\text{PbI}_4$ , and that after (c,d) 204 and (e,f) 420 h of ball-milling

As-prepared  $\text{PEA}_2\text{PbI}_4$  (Figure 4.12-a,b) reveals a lamellar-like morphology, with grains of several microns. Such a peculiar morphology is lost due to the ball-milling, which reduces the

size of the crystallites, producing also a broader size distribution (Figure 4.12-c,f). As in the case of  $\text{MAPbI}_3$ , by further prolonging the mechanical treatment (from 204 to 420 h), a dramatic change in the crystal morphology is not found. However, as is clear from the diffraction data, the intrinsic crystallinity is progressively reduced by increasing the ball-milling time, irrespective of the sample morphology and size.

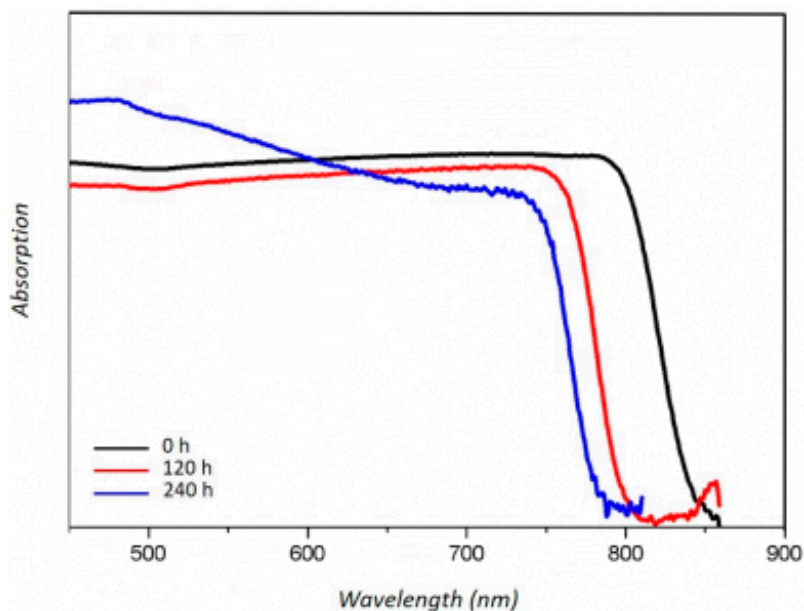


Figure 4.13 Absorption spectra of as-prepared (0 h)  $\text{MAPbI}_3$ , and after 120 and 240 h of ball-milling

For the 3D  $\text{MAPbI}_3$  sample, the absorption spectra (Figure 4.13) show an evident shift associated with the ball-milling process. From the as-prepared sample to the 240-h-milled one, there is a “blue shift” of about 0.1 eV, with the sample after 120 h of treatment laying in an intermediate region. As discussed above, the high-energy process causes a phase transition from the

tetragonal to the cubic perovskite phase. Additionally, it induces an expansion of the lattice. In principle, a reduction of the band gap, passing from a distorted Pb-I geometry (tetragonal) to a symmetric one (cubic), could be caused by an improved interaction between the lead and iodide orbitals.

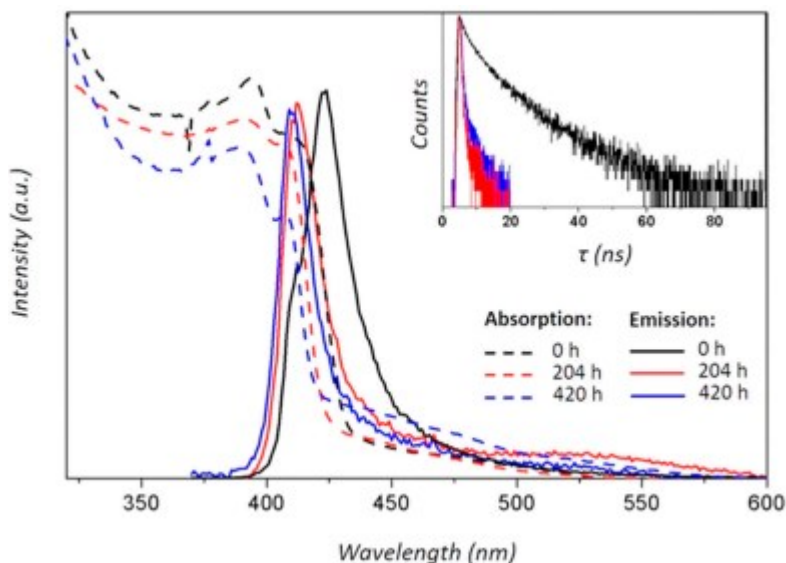


Figure 4.14 Absorption and steady-state emission photoluminescence (PL) spectra of as-prepared (0 h)  $\text{PEA}_2\text{PbI}_4$ , and that after 204 and 420 h of ball-milling (main panel). Time-resolved PL spectra (inset) of the same samples

However, in the examined systems, the transition to the cubic phase is also linked to a lattice expansion, leading to an elongation of the Pb-I bond length and thus to the downshift of the VB<sup>47,48</sup>. In the cubic phase “regime” of the  $\text{MAPbI}_3$  perovskite, the  $[\text{PbI}_6]^{4-}$  octahedra expansion (Table 4.1) increases the Pb-I bond length. This in turn reduces the coupling of the Pb s and the I p orbitals, and pushes down the VB, leading to the observed blue shift of the band gap. It is worth noting that the absorption edge retains a relative sharpness, even after long-

lasting milling, which is an indirect indication of material order retention, as the low-energy tail of the exciton absorption is reminiscent of Urbach absorption, which is a measure of the disorder<sup>49</sup>. The emissions of the systems could not be obtained, for two main reasons; one is related to the setup used, which is very weakly sensitive above 830 nm, where the emission band likely lays<sup>50</sup>, and the second is related to the very weak emission expected in such systems, due to the defects introduced following high-energy milling, as observed below for the more strongly emissive samples (PEA<sub>2</sub>PbI<sub>4</sub>). For PEA<sub>2</sub>PbI<sub>4</sub> systems, a similar trend for the absorption spectra can be observed (Figure 4.14), also resulting in the light emission behavior, but with some additional findings. The as-prepared crystalline powder shows a narrow intense emission, characterized by a lifetime in the order of a few nanoseconds (biexponential decay: 2.5 and 10.5 ns), and the emission band presents a shift, relative to the absorption onset, of a few nm (around 8 nm). For the samples after 204 h and 420 h of high-energy treatment, consistent with the absorption features, a blue shift, a reduction in terms of the intensity of the emission compared to the referential compound, a smaller Stokes shift and a reduction of the emission lifetime can be noticed (for both samples the emission decays were below 50 ps). As clearly evidenced by the XRD measurements and the SEM images, the quality of the PEA<sub>2</sub>PbI<sub>4</sub> crystals is strongly affected by the ball-milling, and the introduction of electronically active defects is logically linked to this process, impacting on the optical properties. However, of interest is the shift of the absorption and emission, which has been observed for 2D systems when quantum confinement effects were triggered by the system's reduced dimensionality. Herein, it is possible that some crystals, at least in one dimension, could shrink following ball-milling under the material Bohr radius, triggering some quantum confinement. Some of us recently

found that, even in the bulk perovskite, a single photon emission could be triggered via material deposition protocol variation<sup>51</sup>; therefore, further studies will be dedicated to the issue.

### Conclusions

In this study, the effect of extended ball-milling on the structural, morphological and optical properties of MAPbI<sub>3</sub> 3D and PEA<sub>2</sub>PbI<sub>4</sub> 2D perovskite crystals was investigated. Particularly, polycrystalline powders were synthesized via a wet-chemistry method; they then underwent high-energy ball-millings of different durations, and were analyzed using XRD, SEM, absorbance and PL spectroscopies. From the structural point of view, the XRD results showed no sign of amorphization for either sample, even after the prolonged milling treatment. Additionally, the processing induces a clear phase transition (from tetragonal to cubic) already after 72 h for MAPbI<sub>3</sub>, and a significant crystallinity reduction for the PEA<sub>2</sub>PbI<sub>4</sub> perovskite. The morphological SEM investigation displayed a reduction of the crystals' quality due to the ball-milling, with a reduction of their size and an agglomeration tendency. The optical characterization showed an interesting effect on the MAPbI<sub>3</sub> and PEA<sub>2</sub>PbI<sub>4</sub>'s band gap tunings, attributable to the high-energy treatment. Additionally, the 2D perovskite exhibited a reduction in terms of emission intensity and lifetime, probably due to the introduction of electronic defects, attributable the decreased quality of the crystals. In conclusion, the mechanical ball-milling process affects many properties of crystalline MAPbI<sub>3</sub> 3D and PEA<sub>2</sub>PbI<sub>4</sub> 2D perovskites, without incurring their amorphization, and it could be further applied to a wider class of OHPs in order to gain information regarding (micro)structure-properties correlations.



## References

1. Grancini, G.; Nazeeruddin, M.K. Dimensional tailoring of hybrid perovskites for photovoltaics. *Nat. Rev. Mater.* 2019, 4, 4–22
2. Fu, Y.; Zhu, H.; Schrader, A.W.; Liang, D.; Ding, Q.; Joshi, P.; Hwang, L.; Zhu, X.Y.; Jin, S. Nanowire Lasers of Formamidinium Lead Halide Perovskites and Their Stabilized Alloys with Improved Stability. *Nano Lett.* 2016, 16, 1000–1008.
3. Wang, F.; Mei, J.; Wang, Y.; Zhang, L.; Zhao, H.; Zhao, D. Fast Photoconductive Responses in Organometal Halide Perovskite Photodetectors. *ACS Appl. Mater. Interfaces* 2016, 8, 2840–2846.
4. Choi, J.; Han, J.S.; Hong, K.; Kim, S.Y.; Jang, H.W. Organic–Inorganic Hybrid Halide Perovskites for Memories, Transistors, and Artificial Synapses. *Adv. Mater.* 2018, 30, 1–21.
5. Zuo, T.; He, X.; Hu, P.; Jiang, H. Organic-Inorganic Hybrid Perovskite Single Crystals: Crystallization, Molecular Structures, and Bandgap Engineering. *ChemNanoMat* 2019, 5, 278–289.
6. Colella, S.; Mazzeo, M.; Rizzo, A.; Gigli, G.; Listorti, A. The Bright Side of Perovskites. *J. Phys. Chem. Lett.* 2016, 7, 4322–4334.
7. Anni, M.; Creti, A.; Zhang, Y.; De Giorgi, M.L.; Lomascolo, M. Investigation of the role of the environment on the photoluminescence and the exciton relaxation of CsPbBr<sub>3</sub> nanocrystals thin films. *Appl. Sci.* 2020, 10, 2148.
8. Huang, Y.; Li, L.; Liu, Z.; Jiao, H.; He, Y.; Wang, X.; Zhu, R.; Wang, D.; Sun, J.; Chen, Q.; et al. The intrinsic properties of FA(1-X)MAxPbI<sub>3</sub> perovskite single crystals. *J. Mater. Chem. A* 2017, 5, 8537–8544.

9. Cheng, X.; Yang, S.; Cao, B.; Tao, X.; Chen, Z. Single Crystal Perovskite Solar Cells: Development and Perspectives. *Adv. Funct. Mater.* 2020, 30, 1–20.
10. Giuri, A.; Masi, S.; Listorti, A.; Gigli, G.; Colella, S.; Esposito Corcione, C.; Rizzo, A. Polymeric rheology modifier allows single-step coating of perovskite ink for highly efficient and stable solar cells. *Nano Energy* 2018, 54, 400–408.
11. Yamada, Y.; Yamada, T.; Phuong, L.Q.; Maruyama, N.; Nishimura, H.; Wakamiya, A.; Murata, Y.; Kanemitsu, Y. Dynamic Optical Properties of  $\text{CH}_3\text{NH}_3\text{PbI}_3$  Single Crystals As Revealed by One- and Two-Photon Excited Photoluminescence Measurements. *J. Am. Chem. Soc.* 2015, 137, 10456–10459.
12. Ding, J.; Yan, Q. Organic-Inorganic Hybrid Halide; Perovskite. *Single* 2017, 60, 1063–1078.
13. Yamada, T.; Yamada, Y.; Kanemitsu, Y. Photon recycling in perovskite  $\text{CH}_3\text{NH}_3\text{PbX}_3$  ( $\text{X} = \text{I}, \text{Br}, \text{Cl}$ ) bulk single crystals and polycrystalline films. *J. Lumin.* 2020, 220, 116987.
14. Masi, S.; Sestu, N.; Valenzano, V.; Higashino, T.; Imahori, H.; Saba, M.; Bongiovanni, G.; Armenise, V.; Milella, A.; Gigli, G.; et al. Simple Processing Additive-Driven 20% Efficiency for Inverted Planar Heterojunction Perovskite Solar Cells. *ACS Appl. Mater. Interfaces* 2020, 12, 18431–18436.
15. Yang, J.; Chen, S.; Xu, J.; Zhang, Q.; Liu, H.; Liu, Z.; Yuan, M. A review on improving the quality of Perovskite Films in Perovskite Solar Cells via the weak forces induced by additives. *Appl. Sci.* 2019, 9, 4393.
16. Shen, H.; Nan, R.; Jian, Z.; Li, X. Defect step controlled growth of perovskite  $\text{MAPbBr}_3$  single crystal. *J. Mater. Sci.* 2019, 54, 11596–11603.
17. Wang, Y.L.; Chang, S.; Chen, X.M.; Ren, Y.D.; Shi, L.F.; Liu, Y.H.; Zhong, H.Z. Rapid Growth of Halide Perovskite Single Crystals: From Methods to Optimization Control. *Chin. J. Chem.* 2019, 37, 616–629.

18. Pan, W.; Wei, H.; Yang, B. Development of Halide Perovskite Single Crystal for Radiation Detection Applications. *Front. Chem.* 2020, 8, 1–9.
19. Alberti, A.; Deretzis, I.; Mannino, G.; Smecca, E.; Giannazzo, F.; Listorti, A.; Colella, S.; Masi, S.; La Magna, A. Nitrogen Soaking Promotes Lattice Recovery in Polycrystalline Hybrid Perovskites. *Adv. Energy Mater.* 2019, 9, 1–12.
20. Chen, L.; Tan, Y.Y.; Chen, Z.X.; Wang, T.; Hu, S.; Nan, Z.A.; Xie, L.Q.; Hui, Y.; Huang, J.X.; Zhan, C.; et al. Toward Long-Term Stability: Single-Crystal Alloys of Cesium-Containing Mixed Cation and Mixed Halide Perovskite. *J. Am. Chem. Soc.* 2019, 141, 1665–1671.
21. Kim, H.; Byun, H.R.; Jeong, M.S. Synthesis and Characterization of Multiple-Cation Rb(MAFA)PbI<sub>3</sub> Perovskite Single Crystals. *Sci. Rep.* 2019, 9, 1–7.
22. Rong, S.; Xiao, Y.; Jiang, J.; Zeng, Q.; Li, Y. Strongly Enhanced Photoluminescence and Photoconductivity in Erbium-Doped MAPbBr<sub>3</sub> Single Crystals. *J. Phys. Chem. C* 2020, 124, 8992–8998.
23. Wu, C.; Guo, D.; Li, P.; Wang, S.; Liu, A.; Wu, F. A study on the effects of mixed organic cations on the structure and properties in lead halide perovskites. *Phys. Chem. Chem. Phys.* 2020, 22, 3105–3111.
24. Pisanu, A.; Coduri, M.; Morana, M.; Ciftci, Y.O.; Rizzo, A.; Listorti, A.; Gaboardi, M.; Bindi, L.; Queloz, V.I.E.; Milanese, C.; et al. Exploring the role of halide mixing in lead-free BZA<sub>2</sub>SnX<sub>4</sub> two dimensional hybrid perovskites. *J. Mater. Chem. A* 2020, 8, 1875–1886.
25. Wang, C.; Ecker, B.R.; Wei, H.; Huang, J.; Gao, Y. Environmental Surface Stability of the MAPbBr<sub>3</sub> Single Crystal. *J. Phys. Chem. C* 2018, 122, 3513–3522.
26. Chen, C.; Hu, X.; Lu, W.; Chang, S.; Shi, L.; Li, L.; Zhong, H.; Han, J.B. Elucidating the phase transitions and temperature-

- dependent photoluminescence of MAPbBr<sub>3</sub> single crystal. *J. Phys. D. Appl. Phys.* 2018, 51.
27. Dimesso, L.; Wittich, C.; Mayer, T.; Jaegermann, W. Phase-change behavior of hot-pressed methylammonium lead bromide hybrid perovskites. *J. Mater. Sci.* 2019, 54, 2001–2015.
28. Jaffe, A.; Lin, Y.; Beavers, C.M.; Voss, J.; Mao, W.L.; Karunadasa, H.I. High-pressure single-crystal structures of 3D lead-halide hybrid perovskites and pressure effects on their electronic and optical properties. *ACS Cent. Sci.* 2016, 2, 201–209.
29. Sun, S.; Deng, Z.; Wu, Y.; Wei, F.; Halis Isikgor, F.; Brivio, F.; Gaultois, M.W.; Ouyang, J.; Bristowe, P.D.; Cheetham, A.K.; et al. Variable temperature and high-pressure crystal chemistry of perovskite formamidinium lead iodide: A single crystal X-ray diffraction and computational study. *Chem. Commun.* 2017, 53, 7537–7540.
30. McClintock, L.; Xiao, R.; Hou, Y.; Gibson, C.; Travaglini, H.C.; Abramovitch, D.; Tan, L.Z.; Senger, R.T.; Fu, Y.; Jin, S.; et al. Temperature and Gate Dependence of Carrier Diffusion in Single Crystal Methylammonium Lead Iodide Perovskite Microstructures. *J. Phys. Chem. Lett.* 2020, 11, 1000–1006.
31. Huang, W.; Yue, S.; Liu, Y.; Zhu, L.; Jin, P.; Wu, Q.; Zhang, Y.; Chen, Y.; Liu, K.; Liang, P.; et al. Observation of Unusual Optical Band Structure of CH<sub>3</sub>NH<sub>3</sub>PbI<sub>3</sub> Perovskite Single Crystal. *ACS Photonics* 2018, 5, 1583–1590.
32. Liu, C.; Li, Z.; Yang, L.; Yao, X.; Li, H.; Liu, X.; Zhao, Y.; Zhu, P.; Cui, T.; Sun, C.; et al. Optical Behaviors of a Microsized Single-Crystal MAPbI<sub>3</sub> Plate under High Pressure. *J. Phys. Chem. C* 2019.
33. Bonomi, S.; Tredici, I.; Albini, B.; Galinetto, P.; Rizzo, A.; Listorti, A.; Tamburini, U.A.; Malavasi, L. Ambient condition retention of band-gap tuning in MAPbI<sub>3</sub> induced by high pressure quenching. *Chem. Commun.* 2018, 54, 13212–13215.

34. Colella, S.; Todaro, M.; Masi, S.; Listorti, A.; Altamura, D.; Caliendo, R.; Giannini, C.; Carignani, E.; Geppi, M.; Meggiolaro, D.; et al. Light-Induced Formation of  $\text{Pb}^{3+}$  Paramagnetic Species in Lead Halide Perovskites. *ACS Energy Lett.* 2018, 3, 1840–1847.
35. Elseman, A.M.; Rashad, M.M.; Hassan, A.M. Easily Attainable, Efficient Solar Cell with Mass Yield of Nanorod Single-Crystalline Organo-Metal Halide Perovskite Based on a Ball Milling Technique. *ACS Sustain. Chem. Eng.* 2016, 4, 4875–4886.
36. Protesescu, L.; Yakunin, S.; Nazarenko, O.; Dirin, D.N.; Kovalenko, M.V. Low-Cost Synthesis of Highly Luminescent Colloidal Lead Halide Perovskite Nanocrystals by Wet Ball Milling. *ACS Appl. Nano Mater.* 2018, 1, 1300–1308.
37. Zhang, L.; Xu, Z.; Cao, L.; Yao, X. Synthesis of BF-PT perovskite powders by high-energy ball milling. *Mater. Lett.* 2007, 61, 1130–1133.
38. Manukyan, K.V.; Yeghishyan, A.V.; Moskovskikh, D.O.; Kapaldo, J.; Mintairov, A.; Mukasyan, A.S. Mechanochemical synthesis of methylammonium lead iodide perovskite. *J. Mater. Sci.* 2016, 51, 9123–9130.
39. Jodlowski, A.D.; Yépez, A.; Luque, R.; Camacho, L.; de Miguel, G. Benign-by-Design Solventless Mechanochemical Synthesis of Three-, Two-, and One-Dimensional Hybrid Perovskites. *Angew. Chem. Int. Ed.* 2016, 55, 14972–14977.
40. Palazon, F.; El Ajjouri, Y.; Bolink, H.J. Making by Grinding: Mechanochemistry Boosts the Development of Halide Perovskites and Other Multinary Metal Halides. *Adv. Energy Mater.* 2019, 9, 1902499, 1–13.
41. Rashad, M.M.; Elseman, A.M.; Hassan, A.M. Facile synthesis, characterization and structural evolution of nanorods single-crystalline  $(\text{C}_4\text{H}_9\text{NH}_3)_2\text{PbI}_2\text{X}_2$  mixed halide organometal

perovskite for solar cell application. *Optik (Stuttg)* 2016, 127, 9775–9787.

42. Palazon, F.; El Ajjouri, Y.; Sebastia-Luna, P.; Lauciello, S.; Manna, L.; Bolink, H.J. Mechanochemical synthesis of inorganic halide perovskites: Evolution of phase-purity, morphology, and photoluminescence. *J. Mater. Chem. C* 2019, 7, 11406–11410.

43. Mekkat, P.; Predeep, P. Hybrid perovskite single crystal with extended absorption edge and environmental stability: Towards a simple and easy synthesis procedure. *Mater. Chem. Phys.* 2020, 239, 122084.

44. Le Bail, A. Whole powder pattern decomposition methods and applications: A retrospection. *Powder Diffr.* 2005, 20, 316–326.

45. Mao, L.; Stoumpos, C.C.; Kanatzidis, M.G. Two-Dimensional Hybrid Halide Perovskites: Principles and Promises. *J. Am. Chem. Soc.* 2019, 141, 1171–1190.

46. Liu, Y.; Ye, H.; Zhang, Y.; Zhao, K.; Yang, Z.; Yuan, Y.; Wu, H.; Zhao, G.; Yang, Z.; Tang, J.; et al. Surface-Tension-Controlled Crystallization for High-Quality 2D Perovskite Single Crystals for Ultrahigh Photodetection. *Matter* 2019, 1, 465–480.

47. Postorino, P.; Malavasi, L. Pressure-Induced Effects in Organic-Inorganic Hybrid Perovskites. *J. Phys. Chem. Lett.* 2017, 8, 2613–2622.

48. Szafranski, M.; Katrusiak, A. Mechanism of Pressure-Induced Phase Transitions, Amorphization, and Absorption-Edge Shift in Photovoltaic Methylammonium Lead Iodide. *J. Phys. Chem. Lett.* 2016, 7, 3458–3466.

49. Singh, S.; Li, C.; Panzer, F.; Narasimhan, K.L.; Graeser, A.; Gujar, T.P.; Köhler, A.; Thelakkat, M.; Huettner, S.; Kabra, D. Effect of Thermal and Structural Disorder on the Electronic

Structure of Hybrid Perovskite Semiconductor  $\text{CH}_3\text{NH}_3\text{PbI}_3$ . *J. Phys. Chem. Lett.* 2016, 7, 3014–3021.

50. Shi, D.; Adinolfi, V.; Comin, R.; Yuan, M.; Alarousu, E.; Buin, A.; Chen, Y.; Hoogland, S.; Rothenberger, A.; Katsiev, K.; et al. Low trap-state density and long carrier diffusion in organolead trihalide perovskite single crystals. *Science* 2015, 347, 519–522.

51. Suárez-Forero, D.G.; Giuri, A.; De Giorgi, M.; Polimeno, L.; De Marco, L.; Todisco, F.; Gigli, G.; Dominici, L.; Ballarini, D.; Ardizzone, V.; et al. Quantum Nature of Light in Nonstoichiometric Bulk Perovskites. *ACS Nano* 2019, 13, 10711–10716

## FUTURE PERSPECTIVES

Several works that could perfectly fit into the previous chapters are now still in progress. Some of them are at their really beginning, for instance, the deposition of 2D and quaternary metal halide perovskites by the means of RF magnetron sputtering. Many others are instead about to see the light, such as the: radio frequency magnetron sputtering of the lead-free and mixed halide  $\text{Cs}_3\text{Sb}_2\text{X}_9$  thin films integrated into complete devices; the high-pressure quenching and extended ball-milling of the lead-free hybrid  $\text{MA}_3\text{Bi}_2\text{I}_9$  and inorganic  $\text{Cs}_3\text{Bi}_2\text{I}_9$ ; high-pressure in-situ studies at the large facilities of hybrid phases containing large cations, like benzylammonium, butylammonium, and 2,2-(ethylenedioxy)bis(ethylammonium); the in-situ structural investigation of moisture/oxygen sensitive

thin films of perovskites containing  $\text{Sn}^{2+}$ , in order to best comprehend their degradation in controlled environmental conditions.

There is still considerable work to do to build reliable, durable, convenient, and largely marketable perovskite-based devices. With this thesis we set a strong starting point in this direction, indeed we successfully demonstrated that is possible to: tune structural and optoelectronic properties of several perovskite phases (mainly lead-free) and grow thin films of different metal halide perovskites by vapor phase method highlighting the versatility of this approach.

Current research is now turning towards tin-based MHPs to overcome all the issues and concerns related to lead-containing phases. It is clear that providing novel clues and tools to deal with these phases still represents a key point for further development in the field where we expect a renaissance of lead-free based devices for a vast variety of applications from photovoltaics, detection, and photocatalysis.



# BIBLIOGRAPHY

1. Rogelj, J., Forster, P. M., Kriegler, E., Smith, C. J. & Séférian, R. Estimating and tracking the remaining carbon budget for stringent climate targets. *Nature* **571**, 335–342 (2019).
2. Correa-Baena, J.-P. *et al.* Promises and challenges of perovskite solar cells. *Science* **358**, 739–744 (2017).
3. Lin, K. *et al.* Perovskite light-emitting diodes with external quantum efficiency exceeding 20 per cent. *Nature* **562**, 245–248 (2018).
4. Akkerman, Q. A. & Manna, L. What Defines a Halide Perovskite? *ACS Energy Lett.* **5**, 604–610 (2020).
5. Zhou, C. *et al.* Low dimensional metal halide perovskites and hybrids. *Materials Science and Engineering: R: Reports* **137**, 38–65 (2019).

6. Li, C. *et al.* Formability of  $ABX_3$  ( $X = F, Cl, Br, I$ ) halide perovskites. *Acta Crystallogr B Struct Sci* **64**, 702–707 (2008).
7. Cross, L. E. & Newnham, R. E. History of Ferroelectrics. 17.
8. Møller, C. K. Crystal Structure and Photoconductivity of Cæsium Plumbahalides. *Nature* **182**, 1436–1436 (1958).
9. Hong, X., Ishihara, T. & Nurmikko, A. V. Dielectric confinement effect on excitons in  $PbI_4$ -based layered semiconductors. *Phys. Rev. B* **45**, 6961–6964 (1992).
10. Mitzi, D. B., Feild, C. A., Harrison, W. T. A. & Guloy, A. M. Conducting tin halides with a layered organic-based perovskite structure. *Nature* **369**, 467–469 (1994).
11. Mitzi, D. B., Dimitrakopoulos, C. D. & Kosbar, L. L. Structurally Tailored Organic–Inorganic Perovskites: Optical Properties and Solution-Processed Channel Materials for Thin-Film Transistors. *Chem. Mater.* **13**, 3728–3740 (2001).

12. Hattori, T., Taira, T., Era, M., Tsutsui, T. & Saito, S. Highly efficient electroluminescence from a heterostructure device combined with emissive layered-perovskite and an electron-transporting organic compound. *Chemical Physics Letters* **254**, 103–108 (1996).
13. Roccaforte, F. *et al.* Challenges for energy efficient wide band gap semiconductor power devices: Energy efficient wide band gap semiconductor power devices. *Phys. Status Solidi A* **211**, 2063–2071 (2014).
14. Braly, I. L. *et al.* Hybrid perovskite films approaching the radiative limit with over 90% photoluminescence quantum efficiency. *Nature Photon* **12**, 355–361 (2018).
15. Manser, J. S., Christians, J. A. & Kamat, P. V. Intriguing Optoelectronic Properties of Metal Halide Perovskites. *Chem. Rev.* **116**, 12956–13008 (2016).

16. Stranks, S. D. & Snaith, H. J. Metal-halide perovskites for photovoltaic and light-emitting devices. *Nature Nanotech* **10**, 391–402 (2015).
17. Xing, G. *et al.* Low-temperature solution-processed wavelength-tunable perovskites for lasing. *Nature Mater* **13**, 476–480 (2014).
18. Yakunin, S. *et al.* Low-threshold amplified spontaneous emission and lasing from colloidal nanocrystals of caesium lead halide perovskites. *Nat Commun* **6**, 8056 (2015).
19. Zhu, H. *et al.* Lead halide perovskite nanowire lasers with low lasing thresholds and high quality factors. *Nature Mater* **14**, 636–642 (2015).
20. Wehrenfennig, C., Liu, M., Snaith, H. J., Johnston, M. B. & Herz, L. M. Homogeneous Emission Line Broadening in the Organo Lead Halide Perovskite  $\text{CH}_3\text{NH}_3\text{PbI}_{3-x}\text{Cl}_x$ . *J. Phys. Chem. Lett.* **5**, 1300–1306 (2014).

21. Hoefler, S. F., Trimmel, G. & Rath, T. Progress on lead-free metal halide perovskites for photovoltaic applications: a review. *Monatsh Chem* **148**, 795–826 (2017).
22. Nishimura, K. *et al.* Lead-free tin-halide perovskite solar cells with 13% efficiency. *Nano Energy* **74**, 104858 (2020).
23. Peng, J., Chen, Y., Zheng, K., Pullerits, T. & Liang, Z. Insights into charge carrier dynamics in organo-metal halide perovskites: from neat films to solar cells. *Chem. Soc. Rev.* **46**, 5714–5729 (2017).
24. Aristidou, N. *et al.* The Role of Oxygen in the Degradation of Methylammonium Lead Trihalide Perovskite Photoactive Layers. *Angew. Chem. Int. Ed.* **54**, 8208–8212 (2015).
25. Wang, R. *et al.* A Review of Perovskites Solar Cell Stability. *Adv. Funct. Mater.* **29**, 1808843 (2019).
26. Xing, G. *et al.* Solution-Processed Tin-Based Perovskite for Near-Infrared Lasing. *Adv. Mater.* **28**, 8191–8196 (2016).

27. Zhang, Q. *et al.* Recent progress in lead-free perovskite (-like) solar cells. *Materials Today Energy* **8**, 157–165 (2018).
28. Deng, Y., Xiao, Z. & Huang, J. Light-Induced Self-Poling Effect on Organometal Trihalide Perovskite Solar Cells for Increased Device Efficiency and Stability. *Adv. Energy Mater.* **5**, 1500721 (2015).
29. Giustino, F. & Snaith, H. J. Toward Lead-Free Perovskite Solar Cells. *ACS Energy Lett.* **1**, 1233–1240 (2016).
30. Binek, A. *et al.* Recycling Perovskite Solar Cells To Avoid Lead Waste. *ACS Appl. Mater. Interfaces* **8**, 12881–12886 (2016).
31. Saliba, M. *et al.* Cesium-containing triple cation perovskite solar cells: improved stability, reproducibility and high efficiency. *Energy Environ. Sci.* **9**, 1989–1997 (2016).

32. Bhaumik, S., Ray, S. & Batabyal, S. K. Recent advances of lead-free metal halide perovskite single crystals and nanocrystals: synthesis, crystal structure, optical properties, and their diverse applications. *Materials Today Chemistry* **18**, 100363 (2020).
33. Toshniwal, A. & Kheraj, V. Development of organic-inorganic tin halide perovskites: A review. *Solar Energy* **149**, 54–59 (2017).
34. Yang, T. C.-J., Fiala, P., Jeangros, Q. & Ballif, C. High-Bandgap Perovskite Materials for Multijunction Solar Cells. *Joule* **2**, 1421–1436 (2018).
35. Saparov, B. *et al.* Thin-Film Deposition and Characterization of a Sn-Deficient Perovskite Derivative  $\text{Cs}_2\text{SnI}_6$ . *Chem. Mater.* **28**, 2315–2322 (2016).
36. Xiao, Z., Zhou, Y., Hosono, H. & Kamiya, T. Intrinsic defects in a photovoltaic perovskite variant  $\text{Cs}_2\text{SnI}_6$ . *Phys. Chem. Chem. Phys.* **17**, 18900–18903 (2015).

37. Ke, W. & Kanatzidis, M. G. Prospects for low-toxicity lead-free perovskite solar cells. *Nat Commun* **10**, 965 (2019).
38. Pan, W. *et al.* Cs<sub>2</sub>AgBiBr<sub>6</sub> single-crystal X-ray detectors with a low detection limit. *Nature Photon* **11**, 726–732 (2017).
39. Soto-Montero, T., Soltanpoor, W. & Morales-Masis, M. Pressing challenges of halide perovskite thin film growth. *APL Materials* **8**, 110903 (2020).
40. Bi, Z. *et al.* Fast preparation of uniform large grain size perovskite thin film in air condition via spray deposition method for high efficient planar solar cells. *Solar Energy Materials and Solar Cells* **162**, 13–20 (2017).
41. Qin, Y. *et al.* High-quality NiO thin film by low-temperature spray combustion method for perovskite solar cells. *Journal of Alloys and Compounds* **810**, 151970 (2019).



42. Nie, W. *et al.* High-efficiency solution-processed perovskite solar cells with millimeter-scale grains. *Science* **347**, 522–525 (2015).
43. Eggers, H. *et al.* Inkjet-Printed Micrometer-Thick Perovskite Solar Cells with Large Columnar Grains. *Adv. Energy Mater.* **10**, 1903184 (2020).
44. Parvazian, E., Abdollah-zadeh, A., Dehghani, M. & Taghavinia, N. Photovoltaic Performance Improvement in Vacuum-Assisted Meniscus Printed Triple-Cation Mixed-Halide Perovskite Films by Surfactant Engineering. *ACS Appl. Energy Mater.* **2**, 6209–6217 (2019).
45. Hwang, K. *et al.* Toward Large Scale Roll-to-Roll Production of Fully Printed Perovskite Solar Cells. *Adv. Mater.* **27**, 1241–1247 (2015).
46. Deng, Y. *et al.* Scalable fabrication of efficient organolead trihalide perovskite solar cells with doctor-bladed active layers. *Energy Environ. Sci.* **8**, 1544–1550 (2015).

47. Ku, Z., Rong, Y., Xu, M., Liu, T. & Han, H. Full Printable Processed Mesoscopic CH<sub>3</sub>NH<sub>3</sub>PbI<sub>3</sub>/TiO<sub>2</sub> Heterojunction Solar Cells with Carbon Counter Electrode. *Sci Rep* **3**, 3132 (2013).
48. Dunlap-Shohl, W. A., Zhou, Y., Padture, N. P. & Mitzi, D. B. Synthetic Approaches for Halide Perovskite Thin Films. *Chem. Rev.* **119**, 3193–3295 (2019).
49. Huang, F. *et al.* Gas-assisted preparation of lead iodide perovskite films consisting of a monolayer of single crystalline grains for high efficiency planar solar cells. *Nano Energy* **10**, 10–18 (2014).
50. Zhou, Y. *et al.* Room-temperature crystallization of hybrid-perovskite thin films via solvent–solvent extraction for high-performance solar cells. *J. Mater. Chem. A* **3**, 8178–8184 (2015).
51. Im, J.-H., Jang, I.-H., Pellet, N., Grätzel, M. & Park, N.-G. Growth of CH<sub>3</sub>NH<sub>3</sub>PbI<sub>3</sub> cuboids with controlled size for

- high-efficiency perovskite solar cells. *Nature Nanotech* **9**, 927–932 (2014).
52. Xiao, Z. *et al.* Efficient, high yield perovskite photovoltaic devices grown by interdiffusion of solution-processed precursor stacking layers. *Energy Environ. Sci.* **7**, 2619–2623 (2014).
53. Bonomi, S. *et al.* Novel Physical Vapor Deposition Approach to Hybrid Perovskites: Growth of MAPbI<sub>3</sub> Thin Films by RF-Magnetron Sputtering. *Sci Rep* **8**, 15388 (2018).
54. Dang, H. X. *et al.* Multi-cation Synergy Suppresses Phase Segregation in Mixed-Halide Perovskites. *Joule* **3**, 1746–1764 (2019).
55. Gratia, P. *et al.* The Many Faces of Mixed Ion Perovskites: Unraveling and Understanding the Crystallization Process. *ACS Energy Lett.* **2**, 2686–2693 (2017).

56. Bonomi, S., Patrini, M., Bongiovanni, G. & Malavasi, L. Versatile vapor phase deposition approach to cesium tin bromide materials  $\text{CsSnBr}_3$ ,  $\text{CsSn}_2\text{Br}_5$  and  $\text{Cs}_2\text{SnBr}_6$ . *RSC Adv.* **10**, 28478–28482 (2020).
57. Xia, L. *et al.* A Review of Perovskite Photovoltaic Materials' Synthesis and Applications via Chemical Vapor Deposition Method. *Materials* **12**, 3304 (2019).
58. Bonomi, S. & Malavasi, L. Physical and chemical vapor deposition methods applied to all-inorganic metal halide perovskites. *Journal of Vacuum Science & Technology A* **38**, 060803 (2020).
59. Kim, B.-S., Choi, M.-H., Choi, M.-S. & Kim, J.-J. Composition-controlled organometal halide perovskite via  $\text{CH}_3\text{NH}_3\text{I}$  pressure in a vacuum co-deposition process. *J. Mater. Chem. A* **4**, 5663–5668 (2016).

60. Ramos, F. J. *et al.* Perovskite Solar Cells Based on Nanocolumnar Plasma-Deposited ZnO Thin Films. *ChemPhysChem* **15**, 1148–1153 (2014).
61. Bansode, U. & Ogale, S. On-axis pulsed laser deposition of hybrid perovskite films for solar cell and broadband photo-sensor applications. *Journal of Applied Physics* **121**, 133107 (2017).
62. Malinkiewicz, O. *et al.* Perovskite solar cells employing organic charge-transport layers. *Nature Photon* **8**, 128–132 (2014).
63. Kim, B.-S., Kim, T.-M., Choi, M.-S., Shim, H.-S. & Kim, J.-J. Fully vacuum-processed perovskite solar cells with high open circuit voltage using MoO<sub>3</sub>/NPB as hole extraction layers. *Organic Electronics* **17**, 102–106 (2015).
64. Liu, M., Johnston, M. B. & Snaith, H. J. Efficient planar heterojunction perovskite solar cells by vapour deposition. *Nature* **501**, 395–398 (2013).

65. Wang, S. *et al.* Smooth perovskite thin films and efficient perovskite solar cells prepared by the hybrid deposition method. *J. Mater. Chem. A* **3**, 14631–14641 (2015).
66. Ávila, J., Momblona, C., Boix, P. P., Sessolo, M. & Bolink, H. J. Vapor-Deposited Perovskites: The Route to High-Performance Solar Cell Production? *Joule* **1**, 431–442 (2017).
67. Shen, P.-S., Chiang, Y.-H., Li, M.-H., Guo, T.-F. & Chen, P. Research Update: Hybrid organic-inorganic perovskite (HOIP) thin films and solar cells by vapor phase reaction. *APL Mater.* **4**, 091509 (2016).
68. Guo, P. *et al.* Room-Temperature Red-Green-Blue Whispering-Gallery Mode Lasing and White-Light Emission from Cesium Lead Halide Perovskite ( $\text{CsPbX}_3$ , X = Cl, Br, I) Microstructures. *Advanced Optical Materials* **6**, 1700993 (2018).

69. Tian, C. *et al.* Chemical Vapor Deposition Method Grown All-Inorganic Perovskite Microcrystals for Self-Powered Photodetectors. *ACS Appl. Mater. Interfaces* **11**, 15804–15812 (2019).
70. Luo, P. *et al.* Fast anion-exchange from CsPbI<sub>3</sub> to CsPbBr<sub>3</sub> via Br<sub>2</sub>-vapor-assisted deposition for air-stable all-inorganic perovskite solar cells. *Chemical Engineering Journal* **343**, 146–154 (2018).
71. Luo, P. *et al.* Colorful, bandgap-tunable, and air-stable CsPb(I<sub>x</sub>Br<sub>1-x</sub>)<sub>3</sub> inorganic perovskite films via a novel sequential chemical vapor deposition. *Ceramics International* **44**, 12783–12788 (2018).
72. Borri, C. *et al.* First Proof-of-Principle of Inorganic Lead Halide Perovskites Deposition by Magnetron-Sputtering. *Nanomaterials* **10**, 60 (2019).

73. Veronese, A. *et al.* Morphological and Optical Tuning of Lead-Free Cs<sub>2</sub>SnX<sub>6</sub> (X = I, Br) Perovskite Nanocrystals by Ligand Engineering. *Front. Electron.* **2**, 703182 (2021).
74. Linaburg, M. R., McClure, E. T., Majher, J. D. & Woodward, P. M. Cs<sub>1-x</sub>Rb<sub>x</sub>PbCl<sub>3</sub> and Cs<sub>1-x</sub>Rb<sub>x</sub>PbBr<sub>3</sub> Solid Solutions: Understanding Octahedral Tilting in Lead Halide Perovskites. *Chem. Mater.* **29**, 3507–3514 (2017).
75. Zhang, X., Li, L., Sun, Z. & Luo, J. Rational chemical doping of metal halide perovskites. *Chem. Soc. Rev.* **48**, 517–539 (2019).
76. Leijtens, T., Prasanna, R., Gold-Parker, A., Toney, M. F. & McGehee, M. D. Mechanism of Tin Oxidation and Stabilization by Lead Substitution in Tin Halide Perovskites. *ACS Energy Lett.* **2**, 2159–2165 (2017).
77. Klug, M. T. *et al.* Tailoring metal halide perovskites through metal substitution: influence on photovoltaic and material properties. *Energy Environ. Sci.* **10**, 236–246 (2017).



78. Lu, C.-H., Biesold-McGee, G. V., Liu, Y., Kang, Z. & Lin, Z. Doping and ion substitution in colloidal metal halide perovskite nanocrystals. *Chem. Soc. Rev.* **49**, 4953–5007 (2020).
79. Yuan, G. *et al.* Structural, Optical, and Thermal Properties of  $\text{Cs}_2\text{SnI}_{6-x}\text{Br}_x$  Mixed Perovskite Solid Solutions. *Eur. J. Inorg. Chem.* **2019**, 2524–2529 (2019).
80. Pisanu, A. *et al.* Enhanced Air-Stability of Sn-based Hybrid Perovskites Induced by Dimethylammonium (DMA): Synthesis, Characterization, Aging and Hydrogen Photogeneration of the  $\text{MA}_{1-x}\text{DMA}_x\text{SnBr}_3$  System. *J. Mater. Chem. C* **7**, 7020–7026 (2019).
81. Chiara, R. *et al.* Role of spacer cations and structural distortion in two-dimensional germanium halide perovskites. *J. Mater. Chem. C* **9**, 9899–9906 (2021).
82. Lou, Y., Fang, M., Chen, J. & Zhao, Y. Formation of highly luminescent cesium bismuth halide perovskite

- quantum dots tuned by anion exchange. *Chem. Commun.* **54**, 3779–3782 (2018).
83. Creutz, S. E., Crites, E. N., De Siena, M. C. & Gamelin, D. R. Anion Exchange in Cesium Lead Halide Perovskite Nanocrystals and Thin Films Using Trimethylsilyl Halide Reagents. *Chem. Mater.* **30**, 4887–4891 (2018).
84. Shi, F. Introductory Chapter: Basic Theory of Magnetron Sputtering. in *Magnetron Sputtering [Working Title]* (IntechOpen, 2018). doi:10.5772/intechopen.80550.
85. Burt, R. J., Meyer, S. F. & Hsieh, E. J. Radio frequency magnetron sputtering of thick film amorphous beryllium. *Journal of Vacuum Science and Technology* **17**, 407–410 (1980).
86. Meyer, S. F., Hsieh, E. J. & Burt, R. J. R.F. magnetron sputtering of thick platinum coatings on glass microspheres. *Thin Solid Films* **72**, 373–378 (1980).

87. Dagamseh, A. M. K., Vet, B., Tichelaar, F. D., Sutta, P. & Zeman, M. ZnO:Al films prepared by rf magnetron sputtering applied as back reflectors in thin-film silicon solar cells. *Thin Solid Films* **516**, 7844–7850 (2008).
88. Fischer, J. *et al.* Development of thin film cathodes for lithium-ion batteries in the material system Li–Mn–O by r.f. magnetron sputtering. *Thin Solid Films* **528**, 217–223 (2013).
89. Nagata, A. & Okayama, H. Characterization of solid oxide fuel cell device having a three-layer film structure grown by RF magnetron sputtering. *Vacuum* **66**, 523–529 (2002).
90. Faglia, G., Groppelli, S. & Nelli, P. Methods for the preparation of NO, NO<sub>2</sub>, and H<sub>2</sub>, sensors based on tin oxide thin films, grown by means of the r.f. magnetron sputtering technique. 10.
91. Jeong, S.-H., Kim, J.-K., Kim, B.-S., Shim, S.-H. & Lee, B.-T. Characterization of SiO<sub>2</sub> and TiO<sub>2</sub> films prepared using

- rf magnetron sputtering and their application to anti-reflection coating. *Vacuum* **76**, 507–515 (2004).
92. Lee, J.-H., Lee, S.-H., Yoo, K.-L., Kim, N.-Y. & Hwangbo, C. K. Deposition of multi-period low-emissivity filters for display application by RF magnetron sputtering. *Surface and Coatings Technology* **158–159**, 477–481 (2002).
  93. Kondaiah, P., Shaik, H. & Mohan Rao, G. Studies on RF magnetron sputtered HfO<sub>2</sub> thin films for microelectronic applications. *Electron. Mater. Lett.* **11**, 592–600 (2015).
  94. Zeng, Y. *et al.* Superhard TiAlCN coatings prepared by radio frequency magnetron sputtering. *Thin Solid Films* **584**, 283–288 (2015).
  95. Vuchkov, T., Yaqub, T. B., Evaristo, M. & Cavaleiro, A. Synthesis, Microstructural, and Mechano-Tribological Properties of Self-Lubricating W-S-C(H) Thin Films Deposited by Different RF Magnetron Sputtering Procedures. *Coatings* **10**, 272 (2020).

96. Carvalho, P. *et al.* Structural stability of decorative  $\text{ZrN}_x\text{O}_y$  thin films. *Surface and Coatings Technology* **200**, 748–752 (2005).
97. Popa, A. C. *et al.* Submicrometer Hollow Bioglass Cones Deposited by Radio Frequency Magnetron Sputtering: Formation Mechanism, Properties, and Prospective Biomedical Applications. *ACS Appl. Mater. Interfaces* **8**, 4357–4367 (2016).
98. Postorino, P. & Malavasi, L. Pressure-Induced Effects in Organic–Inorganic Hybrid Perovskites. *J. Phys. Chem. Lett.* **8**, 2613–2622 (2017).
99. Tan, J. C. & Cheetham, A. K. Mechanical properties of hybrid inorganic–organic framework materials: establishing fundamental structure–property relationships. *Chem. Soc. Rev.* **40**, 1059 (2011).

100. Kim, D. Y., Stefanoski, S., Kurakevych, O. O. & Strobel, T. A. Synthesis of an open-framework allotrope of silicon. *Nature Mater* **14**, 169–173 (2015).
101. Kawamoto, T. *et al.* Room-Temperature Polar Ferromagnet  $\text{ScFeO}_3$  Transformed from a High-Pressure Orthorhombic Perovskite Phase. *J. Am. Chem. Soc.* **136**, 15291–15299 (2014).
102. Wang, Y. *et al.* Dynamic Behavior of Molecular Switches in Crystal under Pressure and Its Reflection on Tactile Sensing. *J. Am. Chem. Soc.* **137**, 931–939 (2015).
103. Egan, L., Kamenev, K., Papanikolaou, D., Takabayashi, Y. & Margadonna, S. Pressure-Induced Sequential Magnetic Pole Inversion and Antiferromagnetic–Ferromagnetic Crossover in a Trimetallic Prussian Blue Analogue. *J. Am. Chem. Soc.* **128**, 6034–6035 (2006).

104. Pinkowicz, D. *et al.* Enforcing Multifunctionality: A Pressure-Induced Spin-Crossover Photomagnet. *J. Am. Chem. Soc.* **137**, 8795–8802 (2015).
105. Zhao, Z. *et al.* Pressure induced metallization with absence of structural transition in layered molybdenum diselenide. *Nat Commun* **6**, 7312 (2015).
106. Drozdov, A. P., Eremets, M. I., Troyan, I. A., Ksenofontov, V. & Shylin, S. I. Conventional superconductivity at 203 kelvin at high pressures in the sulfur hydride system. *Nature* **525**, 73–76 (2015).
107. Jaffe, A. *et al.* High-Pressure Single-Crystal Structures of 3D Lead-Halide Hybrid Perovskites and Pressure Effects on their Electronic and Optical Properties. *ACS Cent. Sci.* **2**, 201–209 (2016).
108. Szafranski, M. & Katrusiak, A. Photovoltaic Hybrid Perovskites under Pressure. *J. Phys. Chem. Lett.* **8**, 2496–2506 (2017).

109. Liu, G. *et al.* Pressure-Induced Bandgap Optimization in Lead-Based Perovskites with Prolonged Carrier Lifetime and Ambient Retainability. *Adv. Funct. Mater.* **27**, 1604208 (2017).
110. Liu, X. *et al.* Organic–inorganic halide perovskite based solar cells – revolutionary progress in photovoltaics. *Inorg. Chem. Front.* **2**, 315–335 (2015).
111. McMillan, P. F. New materials from high-pressure experiments. *Nature Mater* **1**, 19–25 (2002).
112. Lee, A. P. & Reedy, B. J. Temperature modulation in semiconductor gas sensing. **8** (1999).
113. Atraszkiewicz, R. *et al.* High pressure gas quenching: Distortion analysis in gears after heat treatment. *Materials Science and Engineering: A* **558**, 550–557 (2012).
114. Heuer, V., Faron, D. R., Bolton, D., Lifshits, M. & Loeser, K. Distortion Control of Transmission Components



- by Optimized High Pressure Gas Quenching. *J. of Materi Eng and Perform* **22**, 1833–1838 (2013).
115. Hu, Z. Q. *et al.* Formation of non–equilibrium alloys by high pressure melt quenching. *Science and Technology of Advanced Materials* **2**, 41–48 (2001).
  116. Huang, J. Y., Yasuda, H. & Mori, H. Highly curved carbon nanostructures produced by ball-milling. *Chemical Physics Letters* **303**, 130–134 (1999).
  117. Li, Y. B., Wei, B. Q., Liang, J., Yu, Q. & Wu, D. H. Transformation of carbon nanotubes to nanoparticles by ball milling process. *Carbon* **37**, 493–497 (1999).
  118. Fecht, H. J., Hellstern, E., Fu, Z. & Johnson, W. L. Nanocrystalline metals prepared by high-energy ball milling. *METALLURGICAL TRANSACTIONS A* **5**.
  119. Stolle, A., Szuppa, T., Leonhardt, S. E. S. & Ondruschka, B. Ball milling in organic synthesis: solutions and challenges. *Chem. Soc. Rev.* **40**, 2317 (2011).

120. Kong, L. B., Ma, J., Zhu, W. & Tan, O. K. Preparation of Bi<sub>4</sub>Ti<sub>3</sub>O<sub>12</sub> ceramics via a high-energy ball milling process. *Materials Letters* **51**, 108–114 (2001).
121. Calka, A. & Radlinski, A. P. Universal high performance ball-milling device and its application for mechanical alloying. *Materials Science and Engineering: A* **134**, 1350–1353 (1991).
122. Weeber, A. W. & Bakker, H. Amorphization by ball milling. A review. *Physica B: Condensed Matter* **153**, 93–135 (1988).